Measurement and Modelling of Human Presence, Through-Wall Attenuation and Link Diversity at Millimetre-Wave Frequencies

by

Anmol Bhardwaj

BASc, The University of British Columbia, 2014

A THESIS SUBMITTED IN PARTIAL FULFILLMENT OF
THE REQUIREMENTS FOR THE DEGREE OF

MASTER OF APPLIED SCIENCE

in

THE FACULTY OF GRADUATE AND POSTDOCTORAL STUDIES

(Electrical and Computer Engineering)

THE UNIVERSITY OF BRITISH COLUMBIA

(Vancouver)

April 2019

The following individuals certify that they have read, and recommend to the Faculty of Graduate and Postdoctoral Studies for acceptance, a thesis/dissertation entitled:

Measurement and Modelling of Human Presence, Through-Wall Attenuation and Link Diversity at Millimetre-Wave Frequencies

submitted by Anmol Bhardwaj in partial fulfillment of the requirements for

the degree of Master of Applied Science

in Electrical & Computer Engineering

Examining Committee:

David G. Michelson
Supervisor

Shahriar Mirabbasi
Supervisory Committee Member

Mieszko Lis
Additional Examiner

Abstract

Exploitation of the millimetre-wave (mmWave) bands at 28 GHz and above is a key part of the fifth generation wireless (5G) strategy to address the exponentially growing demand for high throughput and capacity radio access. However, mmWave signals are highly susceptible to blockage by people and/or building structures. Previous work has presumed that when the direct path is blocked, communication will be conducted by secondary paths due to reflection or scattering by the environment but has not shown how much performance would degrade. Here, our objectives are: 1) to develop a physical-statistical model of the effect of human presence/blockage at 60 GHz; 2) to statistically characterize the manner in which through-wall attenuation varies between wall types, different walls of the same type, and different locations on a given wall together with an indication of how these results scale between 10 and 30 GHz; and 3) to provide an accurate assessment of the relative quality and capacity of direct and secondary paths at 30 GHz in both indoor and outdoor environments.

We used mmWave channel sounders of various types and configurations to conduct comprehensive, accurate and efficient measurement campaigns. The physical-statistical model for human presence is computationally efficient and shows very good agreement with measurements. It provides an accurate estimation of the reflection coefficient and the diffraction correction factor corresponding to indoor measurements at 60 GHz. Our through-wall attenuation measurement results demonstrate that through-wall attenuation falls into separable classes and is amenable to statistical characterization. The through-wall attenuation generally follows a Gaussian distribution in all building materials. Frequency dependence of the form of $f^{1.45}$ is observed between 10 and 30 GHz through-wall attenuation (linear) values. Our results for the assessment of link quality show that the relative path loss on the four strongest secondary paths follow a Log-normal distribution

while the Ricean-K-factor and SISO/MIMO channel capacity follow exponential distributions. They clearly show that the quality and capacity of secondary (reflected) paths at mmWave frequencies is dramatically lower than the direct (LoS) path with results obtained in outdoor microcells to be almost twice as worst as in indoor environments of comparable size.

Lay Summary

Mobile phones and most other personal access wireless devices currently operate in frequency bands below 6 GHz. The limited amount of spectrum available in this range restricts the throughput and capacity that they can provide. Recent advances have made it possible for personal access wireless devices to use frequencies above 28 GHz, i.e., the millimetre-wave bands. Because much more wireless spectrum is available in this frequency range, the throughput and capacity that can be achieved is much greater than in lower bands. However, the strength of millimetre wave signals is greatly reduced when they are obstructed by people and building walls. Although signals reflected by surrounding structures may be used when direct signals are blocked, they will always be weaker than the original signals. To assist product developers, we have developed models of these phenomena that are useful in the design and simulation of alternative techniques for mitigating such fading.

Preface

This thesis was prepared by Anmol Bhardwaj under the direct supervision of Prof. David G. Michelson. Anmol conducted the initial literature survey, worked with Prof. Michelson in developing an overall plan for the thesis, conducted measurements with the help of fellow students, and conducted Matlab analysis to generate results. Prof. Michelson was involved in every stage, oversaw the entire process, and provided advice throughout this work. Dr. Camillo Gentile, a senior research scientist in the Wireless Networks Division at the U.S. National Institute for Standards and Technology (NIST), co-supervised Anmol's work on human presence and reviewed the results for through-wall attenuation and the relative performance of direct and secondary paths.

Jelena Senic, Dr. Peter Papazian, Derek Caudill, Ruoyu Sun, and Dr. Jack Chuang of NIST assisted with the measurement campaign for Chapter 2 (human presence). Candice Loo, Guo Gaungkun, Raghul Sai Subramanian, and Tran Mai Villageois (Universite de Pierre et Marie Curie) assisted with the measurement campaigns for Chapter 3 (through-wall attenuation). Dr. Siamak Bonyadi-Ram, Parham Zarei, Hamed Noori assisted with the measurement campaign and channel sounder development for Chapter 4 (link-quality assessment).

Table of Contents

List of Tables

List of Figures

Acknowledgements

I offer my enduring gratitude to the faculty, staff and my fellow students at UBC, who have inspired me to continue my work in this field. I owe particular thanks to my thesis supervisor Prof. David G. Michelson, for enlarging my vision of science and providing detailed and thoughtful answers to my endless questions. His continuous support and mentorship played a huge role in the completion of this study.

I thank Huawei Technologies Canada for their financial support. I also thank Mr. Mark Hawryluck and Dr. David Steer of Huawei Technologies for their outstanding support and advice.

Special thanks to the U.S. National Institute of Science and Technology (NIST) Communications Technology Lab (Wireless Networks Division) for their financial support. I would like thank Dr. Nada T. Golmie and Dr. Camillo Gentile for all their support and mentorship throughout my stay at NIST.

Last but not least, I thank my fellow students at the UBC Radio Science Lab for their support. Special thanks to Dr. Siamak Bonyadi-Ram, Parham Zarei, Hamed Noori, Candice Loo, Guo Gaungkun, Raghul Sai Subramanian, and Tran Mai Villageois (visiting international research student from Universite de Pierre et Marie Curie) for their support in the development of the hardware and collecting measurements for this study.

Dedication

I would like to dedicate this thesis to my Parents and my Brother, who have relentlessly encouraged me to strive for excellence.

Chapter 1: Introduction

1.1 Significance

Fifth Generation (5G) wireless represents a fundamental break from past convention as the wireless industry seeks to address an ever-broadening range of use cases and user requirements. By introducing new paradigms, architectures, and even new frequency bands, 5G seeks to increase throughput, reduce latency, increase battery life and accommodate ever more users. Exploitation of the vast amounts of spectrum available in the millimetre-wave (mmWave) bands is a key part of the 5G strategy to achieve these goals. In order to address the demand for next generation wireless networks and the extreme shortage of available spectrum at sub-6 GHz frequencies, the Federal Communication Commission (FCC) in the United States and regulators in other jurisdictions, including Innovation, Science and Economic Development (ISED) in Canada, have allocated various bands in the mm-Wave range from 28-90 GHz for this purpose [1]. MmWave access systems will play a key role in 5G efforts to increase the throughput and capacity of radio access networks. Practical implementations will be expected to deliver very high data rates and ultra-low latencies while employing highly directional antennas and operating over distances of less than a few hundred meters.

In an attempt to meet this challenge, several groups have been formed that include IEEE Future Direction 5G Initiative [2], the International Telecommunication Union (ITU) [3], Millimetre-wave Based Mobile Radio Access Network for 5th Generation Integrated Communication (mmMAGIC) [4], the 3rd Generation Partnership project (3GPP) [5], and Mobile and Wireless communications Enablers for the Twenty-twenty Information Society (METIS) [6]. These groups are variously tasked with developing vision, specifications, and modeling and simulation frameworks for 5G and have actively developed mmWave channel models for mostly short range indoor and outdoor environments. The 3GPP released its first channel model for bands above 6 GHz in their Release 14 and has nearly completed its 5G specifications [5].

1.2 Previous Work and its Limitations

Propagation for radio access scenarios at mmWave frequencies has been investigated for many years. In 1985, a millimetre-wave system operating at 60 GHz that used directional fan antennas and spread spectrum modulation was able to reach up to 500 m [6]. At around the same time, the use of mmWave frequencies for non-communication applications such as radar sensing, medical imaging, and automotive navigation was also demonstrated [7]. The 60 GHz band was the first mmWave band to be used for consumer communications applications and for which WLAN and WPAN standards were first developed [8].

The first mmWave WPAN standard was developed by 802.15.3 Task Group 3c. Although it was not widely adopted, it set the stage for later developments such as IEEE 802.11ad (WiGig). Very high data rates were achieved over short ranges with these technologies [9]. SiBeam, a spin-off company from the University of California - Berkley, provided a breakthrough in mmWave technologies by developing a practical implementation of 60 GHz on-chip antenna arrays. This led to the development of the proprietary WirelessHD standard for communication between high definition (HD) home audio/video equipment [10].

Although SiBeam's practical on-chip antenna arrays addressed one of the biggest challenges in mmWave communication systems, channel impairment at mmWave frequencies is still an issue that needs to be fully understood so that suitable mitigation strategies can be developed. One of the biggest challenges at mmWave frequencies is that mmWaves in general are highly susceptible to blockage by people and/or building structures. Penetration loss through building materials is also significantly higher at mmWave frequencies. In an attempt to address some of these concerns, channel modeling groups have conducted measurement campaigns in the past to characterize blockage due to human presence and building materials at mmWave frequencies.

Human presence models that have been proposed to date cover a wide range of complexity. The simplest models only account for the presence or absence of blocking while the most complicated models presented to date account for the observed fading in the shadow region using statistical techniques [11-17]. While the models proposed to date are useful, their range of applicability is extremely limited. It is difficult to extrapolate channel response for a geometry of interest from a measured geometry unless the two are very similar. A more general approach is required.

Similarly, many measurement campaigns have been conducted in the past to characterize through-wall attenuation at mmWave frequencies [2-7]. However, previous work placed very little emphasis on variations in through-wall attenuation that may be observed along a given wall and between walls of different types. Most works focused on deriving dielectric parameters of a superficial wall material. But that is generally insufficient to predict relevant propagation behaviour as walls in general are multi-layered and quite complex. Overall, very little insight exists concerning the range of behavior or distribution either point-to-point on a given wall or between walls of broadly similar type.

When the direct path is blocked or not available, communication will be conducted by secondary paths that arise from reflection or scattering in the environment. Path loss and range of coverage at millimetre-wave frequencies has been studied previously [1], [2], [4], [7-11]. But few if any results capture the relative capability of direct and secondary paths. Previous standards, e.g., IEEE 802.15.3c, IEEE 802.11ad, and WirelessHD, simply assumed that secondary paths exist but without regard for their quality and capacity.

1.3 Objectives

In this work, our three main objectives are:

1. To propose a physical-statistical model for human presence in which the individual paths that contribute to the observed channel response are predicted geometrically while, the reflection coefficient and the diffraction correction factor which determine the strength of the corresponding rays are determined through measurements.

2. To reveal the statistical distribution of through-wall attenuation, either point-to-point on a given wall or between walls of broadly similar type, the extent to which the distributions for different wall types overlap or are separable or distinguishable.

3. To provide an accurate assessment of the relative quality and capacity of direct and secondary paths at millimetre-wave frequencies in typical indoor and outdoor environments and, as a consequence, the performance that can be achieved when using path diversity for radio access.

1.4 Approach

The stages of wireless channel model development that are applied in each of the following chapters are as follows: 1) Collection of measurement data; 2) Estimation of channel parameters (trends, distributions, and patterns); 3) Extraction of Model Parameters identified in Stage 2 (trends, distributions and patterns); and 4) Development of design and/or simulation models.

Stage 1 involves careful planning of the measurement campaign and proper configuration of the measurement equipment (channel sounder). Measurement campaigns require a lot of thought and care in order to be accurate and reproducible. Measurements must be representative and collected economically. Stage 1 further involves calibration and application of error correction models to compensate for imperfections in the measurement equipment.

Stage 2 involves estimation of the channel parameters, such as path loss, channel capacity, etc., and then discerning the distributions corresponding to these parameters. The mean and standard deviations of the derived distributions are then calculated.

Stage 3 involves modeling of the distribution parameters identified in Stage 2. Trends, distributions, and patterns within the parameters (identified in Stage 2) are analyzed. However, it can be quite challenging to accurately resolve such trends due to the lack of data present at this stage. It is often necessary to employ heuristic methods in order to reveal trends and patterns from small amounts of data.

Lastly, Stage 4 involves the development of a design or simulation model. Design models are generally first-order (sequence independent), whereas simulation models are generally second-order (sequence dependent). Such simulation models are generally excited by either uniform or Gaussian processes. In the case of non-Gaussian random variables, copula-based models may be used to account for correlation between variables. Such models are extremely complicated, however.

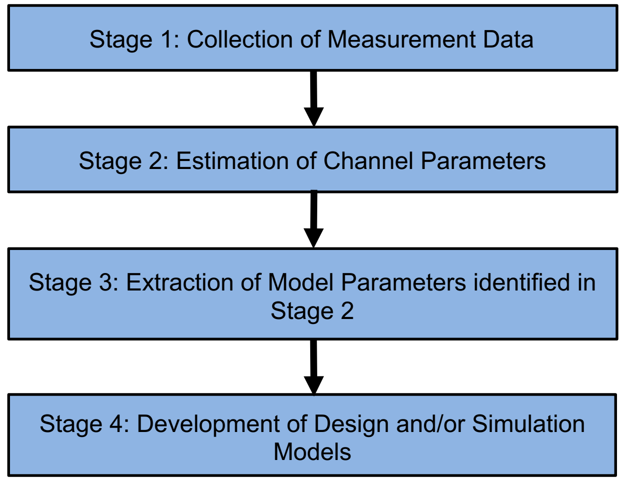

Figure 1 - Stages of Wireless Channel Model Development

1.5 Outline

The remainder of this thesis develops as follows: In Chapter 2, we develop a physical-statistical model for human presence at 60 GHz; In Chapter 3, we develop a statistical model for through-wall attenuation at 10 and 30 GHz; In Chapter 4, we develop a statistical model of link quality at 30 GHz; and, in Chapter 5, we present our conclusions and recommendations for future work.

Chapter 2: Human Presence Measurement and Modeling at 60 GHz

2.1 Introduction

Simple but accurate models of the effect of human presence on path propagation are vital to the simulation of mmWave access networks. Considerable work on the effects of human presence on mmWave propagation have been conducted in recent years. Some work has been purely simulation based, others have used measurements to construct measurement-based models. The ultimate aim of both activities is to provide designer and developers with the tools required to assess the impact of human presence on the capacity and performance of mmWave communication systems in the presence of humans.

In [11], the authors provide a good summary of all previous efforts to model human presence. Simulation based models for human blockage are mainly divided into two main categories: Absorbing screen models and Cylinder models. A version of the absorbing screen model is presented in [12], where the rectangular screen is treated as a vertically-infinitesimal strip and is called a double knife-edge model. In this case double knife-edge diffraction (DKED) from the absorbing screen can be used to estimate the received field at the receiver. Similar work has been presented in [13] where human blockage is modeled by two vertical absorbing strips and is called the Multiple Knife-Edge model. This model incorporates a third diffracted path from the top of the screen. Some more complex versions of this model are reported in [13-15] where human torso, shoulders, and head are also accounted for. Cylinder based human blockage models have also been well established in the literature [16-20]. For these sorts of models, the Geometrical Theory of Diffraction (GTD) and related techniques are generally used to derive the diffracted fields from the cylinder.

Ultimately electromagnetic simulation-based models require verification. A number of measurement campaigns and measurement-based modeling efforts have been conducted both to validate and compliment simulation-based studies [21-27]. Human blockage measurements at 60 GHz are presented in [22] and the measured results are compared with the original DKED model and its modified version that accounts for directional antennas. Similar measurements were conducted in [21], where MacCartney *et. al* present the measurement based two-state and four-state Markov models.

The models that have been proposed to date cover a wide range of complexity. The simplest models only account for presence or absence of blocking while the most complicated models presented to date account for the observed fading in the shadow region using statistical techniques. While the models proposed to date are useful, their range of applicability is extremely limited. It is difficult to extrapolate channel response for a geometry of interest from a measured geometry unless the two are very similar. In the case of more complicated numerical approaches, as the ones demonstrated in [5], the resulting models are highly computationally intensive. We believe that a more general approach is both required and quite tractable.

Here, we propose a physical-statistical model that combines the best qualities of both approaches. The individual paths which contribute to the observed channel response are predicted geometrically. However, the reflection coefficient and the diffraction correction factor which determine the strength of the corresponding rays are determined through measurements.

Accurate calculation of the combination of the rays requires accurate knowledge of the amplitude and phase of the individual rays. In our case the geometric component gives an accurate estimation of the phase and the measurement component give accurate estimation of the strength.

In order to peruse this approach, we devised a measurement setup, conducted a measurement campaign, devised a physical-statistical model that has both measurement and geometric based components and used the data collected both to estimate measurement-based parameters of model as well as to validate outcomes of our model.

The remainder of this chapter is developed as follows: Section 2.2 presents the underlying concepts of this work; Section 2.3 describes the methodology for collecting such measurements; Section 2.4 presents the overall results; and lastly the overall conclusions are drawn in Section 2.5.

2.2 Concepts

2.2.1 Four-State Fading Model for Individual Shadowing Events

In this section, a statistical measurement-based model for a single shadowing event is presented. Such a model can be used by a ray tracing simulation tools in order to simulate individual blockage events. Model parameters are estimated using measurement data collected for

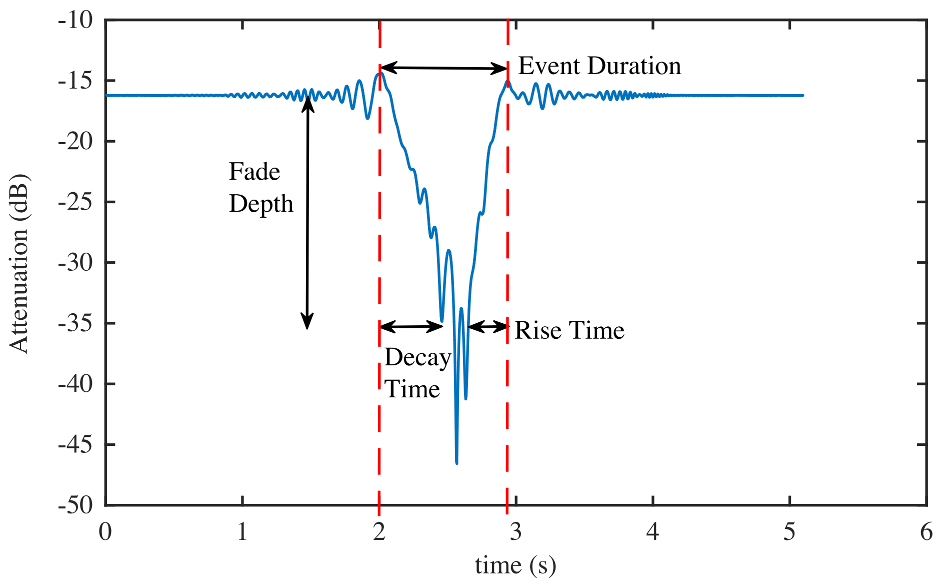

Figure 2 - Human Blockage Attenuation

up to 60 different individual shadowing events that take into account a bevy of different scenarios (described in Section 2.3.1). An example of such a shadowing event is shown in Figure 2.

A given shadowing event can be modeled by estimating the parameters shown in Figure 2, i.e., fade depth, fade duration, decay time, and rise time. The entire shadowing event can be broken down into four separate regions: shadow and unshadow regions along with signal rise and decay regions [21]. These regions are best described using the following equation for signal attenuation due to human blockage over time as the human traverses through the LOS beam,

$$S(t) = \begin{cases} r_{decay} * t, & 0 \le t \le \frac{S_{mean}}{r_{decay}} \\ S_{mean}, & \frac{S_{mean}}{r_{decay}} \le t \le t_D - \frac{S_{mean}}{r_{rise}} \\ S_{mean} - r_{rise} * t, & t_D - \frac{S_{mean}}{r_{rise}} \le t \le t_D \\ 0, & otherwise \end{cases} \quad (1)$$

where S(t) is the Shadowing gain over time, r_{decay} is the decay rate, r_{rise} is the rise rate, and t_D is the overall fade duration. A threshold level needs to be specified in order to estimate the rise and decay rates/times. As shown in Figure 2, the decay time is then calculated starting from the zero-crossing at the start of shadow region up to the threshold. Similar procedure is followed for rise time calculations. Parameter estimation of this model using measurement results is provided in 2.4.1.

2.2.2 Two-Ray Model: Reflection from Human Body

A two-ray model used for estimating the fading within the unshadow regions is presented in this section. This model is just a modified version of the two-ray ground bounce model which has been previously well-established in the literature. The two-rays in this scenario represent the LOS path and the reflected MPC from the human body. According to the model, the overall received power at the receiver is simply a result of interference (constructive/destructive) between these two paths. And that is what gives rise to the oscillatory behavior of the received signal in the unshadow region. The two-ray model for human blockage can be described using the following set of equations. First,

$$r_{LOS}(t) = Re\{\frac{\lambda * \sqrt{G_{LOS}}}{4 * \pi} * \frac{s(t) * e^{\frac{-j2\pi l}{\lambda}}}{l}\} \quad (2)$$

where s(t) is the transmitted signal, G_{LOS} is the Line of Sight (LOS) path gain, and l is the LOS path length. Second,

$$r_{reflected}(t) = Re\{\frac{\lambda * \Gamma(\theta) * \sqrt{G_{reflected}}}{4 * \pi} * \frac{s(t-\tau) * e^{\frac{-j2\pi(x+x')}{\lambda}}}{x + x'}\} \quad (3)$$

where $\Gamma(\theta)$ is the reflection coefficient, $G_{reflected}$ is the path gain along reflected component, x is the path length of the MPC incident upon human body, and x' is the path length of the reflected MPC from human body. $\Gamma(\theta)$ is computed empirically in Section 2.4.2, whereas all other components are geometric parameters. The overall received power at the receiver is given by (4),

$$P_r = \left| r_{LOS}(t) + r_{reflected}(t) \right|^2 \quad (4)$$

2.2.3 Double Knife-Edge Diffraction Model

This section provides a description of the double knife edge diffraction model for absorbing screen. As shown in Figure 3, an infinitesimal vertical screen is used to model the human body. Overall diffracted fields observed at the receiver can be estimated using the equations given below.

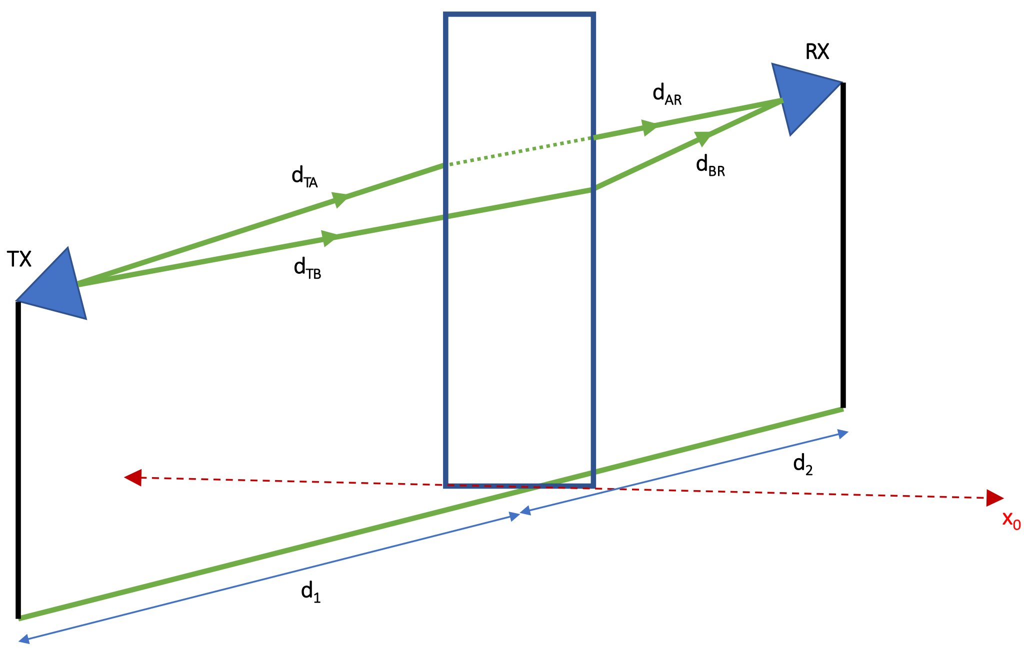

Figure 3 - DKED Model Geometry

First, the field of the non-obstructed half-plane is calculated using the following equation (Fresnel-Huygens principle),

$$G = \frac{1+j}{2}\left\{\left(\frac{1}{2} - C(v)\right) - j\left(\frac{1}{2} - S(v)\right)\right\} \tag{5}$$

where C(v) and S(v) are the cosine and sine Fresnel integral and v is given by the following equation,

$$v = h\sqrt{\frac{2}{\lambda}\left(\left(\frac{1}{d_1}\right) + \left(\frac{1}{d_2}\right)\right)}\ . \tag{6}$$

The following equation represents the superposition of the two knife-edge fields E_a and E_b given by (5),

$$E_{DKED} = \left(E_a \exp\left(-j2\pi f\left(\frac{\Delta d_a}{c}\right)\right) + E_b \exp\left(-j2\pi f\left(\frac{\Delta d_b}{c}\right)\right)\right)^{\gamma} \tag{7}$$

where $\Delta d_a = d_{TA} + d_{AR} - d_1 - d_2,\ \Delta d_b = d_{TB} + d_{BR} - d_1 - d_2$, and γ is the diffraction coefficient.

DKED model comparison with the measurement results is shown in Section 2.4.3. A diffraction correction factor was used in order to correct any mismatch of energy within the shadow region. The diffraction correction factor is just a fraction of the half-plane energy estimated by the DKED model. It was observed that the correction factor was mostly the same for cases with different human subjects and was different for the cases with different transmitter-receiver separation distances.

2.3 Methodology

2.3.1 Measurement Scenarios

The human presence environment is depicted in Figure 3. Several different shadowing events were captured in order to support the models presented in this chapter. A summary of different scenarios in presented in Figure 5. Three different transmitter heights were used. Multiple human walking positions in between transmitter and receiver were measured as shown by the red vertical lines in Figure 5. A total of three different transmitter-receiver separation distances were measured: 4 m, 6 m, and 8 m. Three different human subjects were used in these measurements, all with different body types. The heights corresponding to humans A, B, and C were 1.83 m, 1.72 m, and 1.68 m respectively. In order to ensure consistent walking speed across all scenarios, a metronome was used to help human subjects walking at a steady pace and a constant speed of 0.3 m/s.

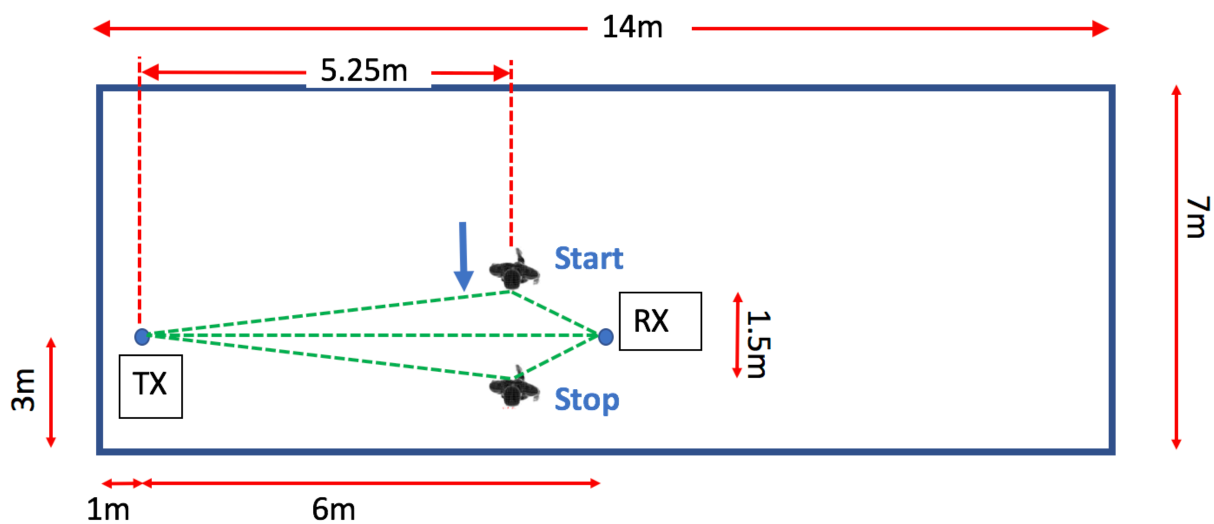

Figure 4 - Human Presence Measurement Environment

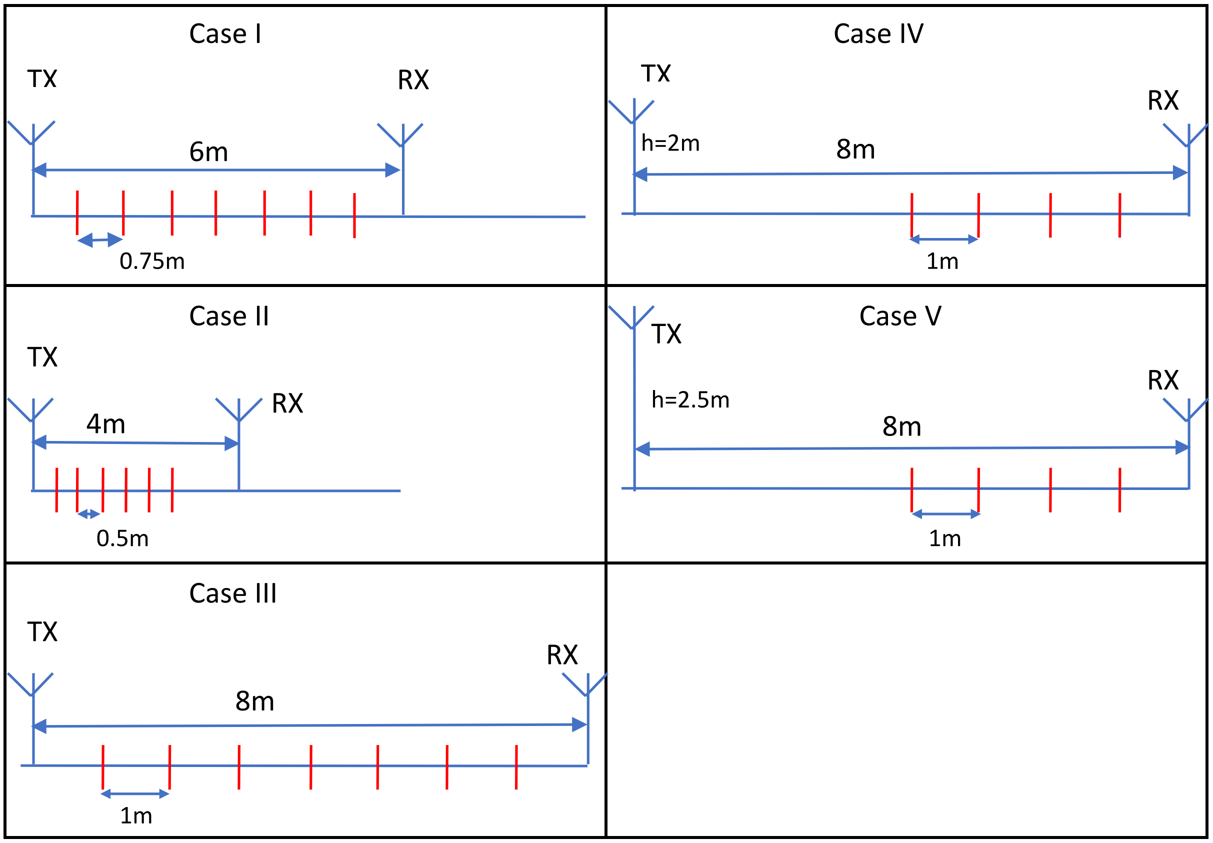

Figure 5 - Human Presence Measurement Scenario

2.3.2 Channel Sounder Specifications

An 8x16 MIMO 60 GHz channel sounder, developed at NIST, was used for the human presence measurements [29]. This channel sounder employs a pseudorandom bit sequence (PRBS) to measure the complex channel impulse response (CIR), a 16-element antenna array with fast switching multiplexer (MUX) at the receiver, and 8-element switched array at the transmitter. Antenna arrays are scalar feed horns (SFHs) with a maximum gain of 18.1 dBi and side-lobe levels below -10 dB. An arbitrary waveform generator (AWG) with a sampling rate of 12 Gsamples/s is employed at the transmitter. The AWG generates a 3 GHz intermediate frequency (IF) signal with BPSK modulation with a 2047-bit pseudorandom (PN) code word. The bit (or chip) rate is 2 Gbits/s, yielding a delay resolution of 0.5 ns and a maximum delay span of 1023.5 ns. The RF section then up-converts the IF signal to 60.5 GHz. The block diagram of the overall channel sounder is shown in Appendix A.

2.3.3 Data Collection and Verification

Figure 6 below shows the overall scenario where the human subject is walking through the LOS path. The array is set up in such a way such that the LOS antennas (channel 69) are completely aligned and the human subject walk perpendicular to the LOS path. A metronome was used in order to ensure a constant pace and a constant walking speed (0.3 m/s) by all human subjects.

Figure 6 - Channel Sounder for Human Presence Measurements at 60 GHz

The channel sounder used for these measurements collected 1500 PDPs (indexed as "sectors" at NIST) for each walking scenario. The time in between bursts was 3.4 ms and the overall shadowing event lasted for 5.1 s. The channel sounder was configured such that at least 5 samples are collected per wavelength. Additional care was given to ensuring that phase stability is achieved between samples. It was observed that phase stability improves if one oscillator is used at the receiver end as opposed to two, as shown in Figure 7. The standard deviation of phase across sectors/time improves significantly in the case of 1 PLDRO. The sector index in Figure 7 represents the number of bursts which is equivalent to the time of the shadowing event.

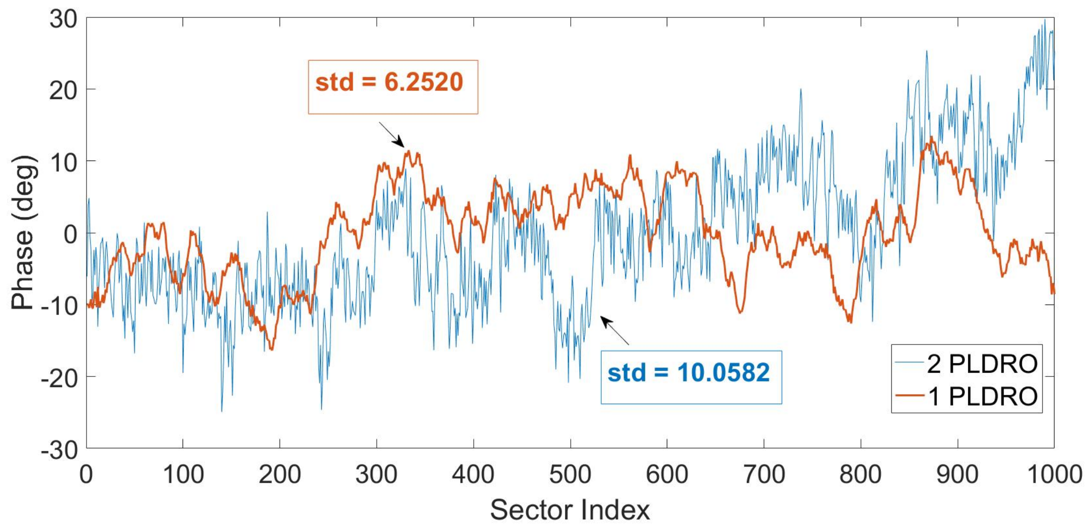

Figure 7 - Phase Variation over Time

2.4 Results

2.4.1 Four-State Model Parameters Estimation using Measurements

This section provides measurement-based parameters for the model presented in Section 2.2.1. A total of 64 shadowing events were used for this analysis. Figure 8 shows the CDFs for fade depths corresponding to 4 m, 6 m, and 8 m separation distances. Fade depth for each shadowing event was calculated in the same manner as shown in Figure 2. Each CDF includes data corresponding to all three human subjects along with seven different walking positions. As shown in Figure 8, fade depths corresponding to 4 m and 6 m transmitter-receiver separation cases are comparable. However, a lot less attenuation was observed for the 8 m case, as expected.

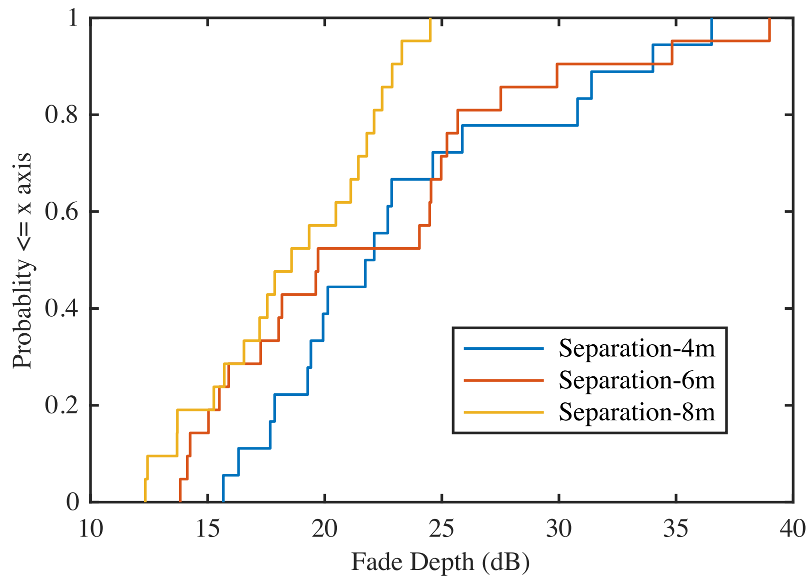

Figure 8 - CDFs for Fade Depth at 4-m, 6-m, and 8-m TX-RX Separation

Estimated distributions for each CDF curve corresponding to the 8-m separation distance are presented in Figure 9. Mean and standard deviation values are also presented for each case. As shown in Figure 9, for 8 m separation case, Weibull distribution best matches the measured results. Similar analysis was also conducted for the separation distances of 4 m and 6 m and it was found that they are best described by the Log-Normal distributions (Table 1).

Average fade duration (AFD) for a given shadowing event is defined in Figure 2. In this case, AFD is shown for a reference level of 0dB. Similar calculations were done for threshold levels of -2 dB, -4 dB, -6 dB, and -8 dB (Figure 10). The results are shown in the form of CDFs in Figure 11. Each CDF includes data to all human subjects and all walking positions. As expected, the AFD decreases as the threshold level decreases.

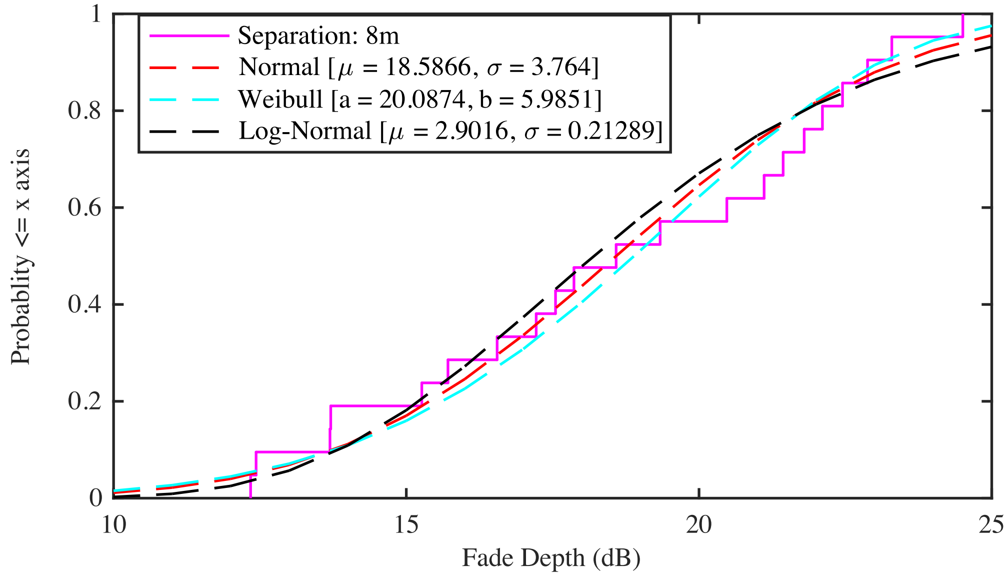

Figure 9 - Fade Depth Estimated Distributions (8-m Separation Distance)

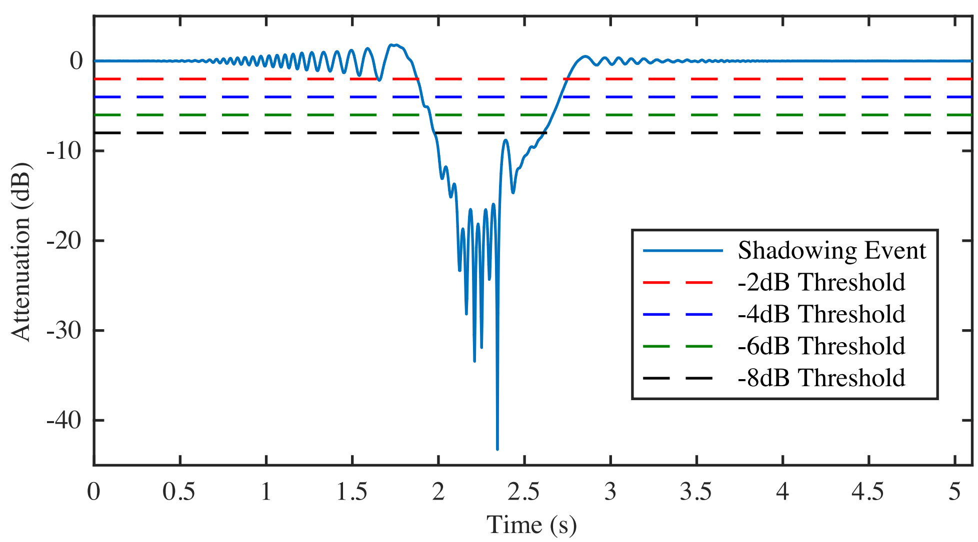

Figure 10 - Threshold Levels (Dashed Lines) for AFD Calculation

Similar to the fade depth, estimated distributions are also analyzed for AFD. The resulting distributions along with the mean and the standard deviation for each case are summarized in Table 1. AFD in each case is best described by the Gaussian distribution.

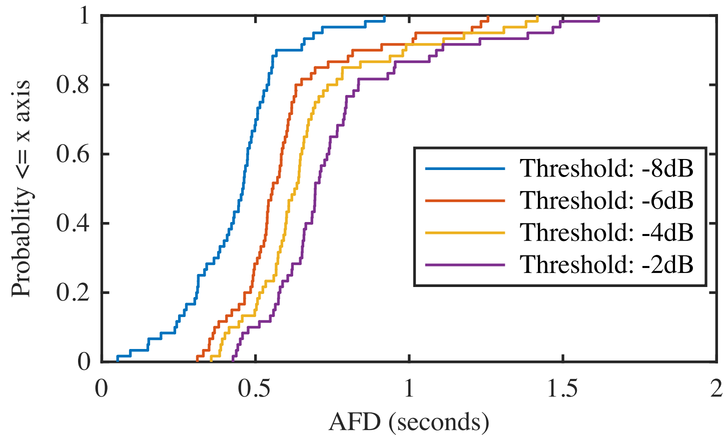

Figure 11 - CDF plots for Average Fade Duration (AFD)

Lastly, rise and decay times corresponding to individual shadowing events are shown in Figure 12. Rise/decay times were calculated by subtracting start/stop times of the shadowing events from the time corresponding to the threshold value, as described in Figure 2. The results shown in Figure 12 provide an accurate estimate of the rise and decay rate of the received power as the human enters and exits the shadow region. The results for rise and decay times are also summarized in in Table 1 and it was observed that both are best described using the Log Normal distribution.

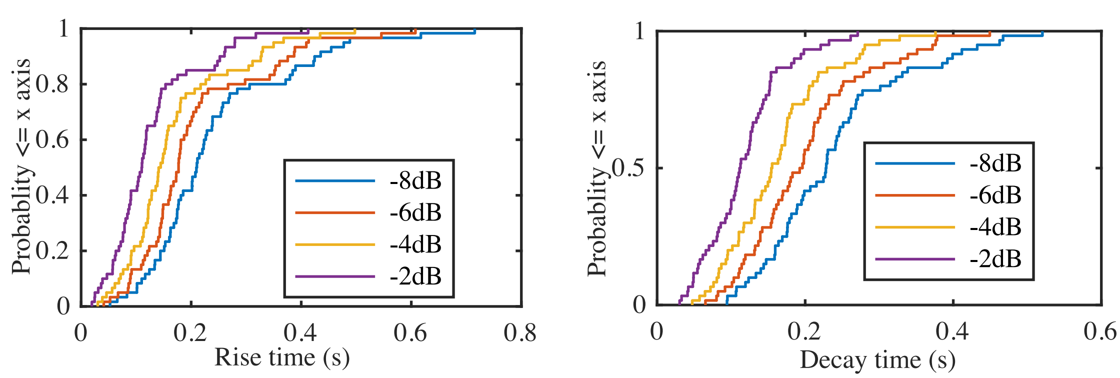

Figure 12 - Rise and Decay Times for Different Threshold Levels

The results summarized in Table 1 for Fade depth, Average Fade Duration, rise time, and decay time match closely with the work conducted by others [11-17].

Table 1 - Estimated Distributions for Fade Depth and AFD

	Distribution	**Mean**	**S.D.**
Fade Depth – 4m	Log-Normal	μ = 23.2705 dB	σ = 6.1584 dB
Fade Depth – 6m	Log-Normal	μ = 21.9835 dB	σ = 6.9862 dB
Fade Depth – 8m	Weibull	a = 20.0874 dB	b = 5.9851 dB
AFD: -2dB	Normal	μ = 0.7589 s	σ = 0.25749 s
AFD: -4dB	Normal	μ = 0.6715 s	σ = 0.22908 s
AFD: -6dB	Normal	μ = 0.59714 s	σ = 0.20425 s
AFD: -8dB	Normal	μ = 0.43717 s	σ = 0.16271 s
Rise: -2dB	LogNormal	μ = 0.1273 s	σ = 0.0912 s
Rise: -4dB	LogNormal	μ = 0.1690 s	σ = 0.1046 s
Rise: -6dB	LogNormal	μ = 0.2052 s	σ = 0.1182 s
Rise: -8dB	LogNormal	μ = 0.2417 s	σ = 0.1335 s
Decay: -2dB	LogNormal	μ = 0.1188 s	σ = 0.0629 s
Decay: -4dB	LogNormal	μ = 0.1635 s	σ = 0.0760 s
Decay: -6dB	LogNormal	μ = 0.2006 s	σ = 0.0875 s
Decay: -8dB	LogNormal	μ = 0.2390 s	σ = 0.1001 s

2.4.2 Two-ray Model Comparison with Measurements

The results for the two-ray model (described in Section 2.2.2) are presented here and are compared with the measurements. The two-ray model was used to estimate the unshadow regions of the overall event. As shown in Figure 13, the unshadow regions were further divided into smaller regions: A1, A2, A3, B1, B2, and B3.

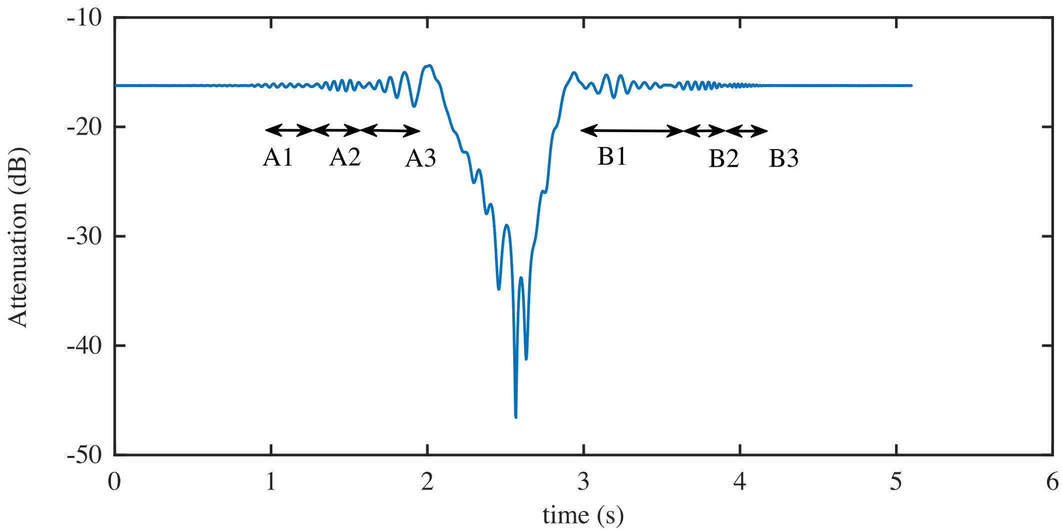

Figure 13 - Measured Attenuation (dB) for Reflection Model

As described in Section 2.2.2, the unshadow regions were further divided in order to account for the change in reflection coefficient.

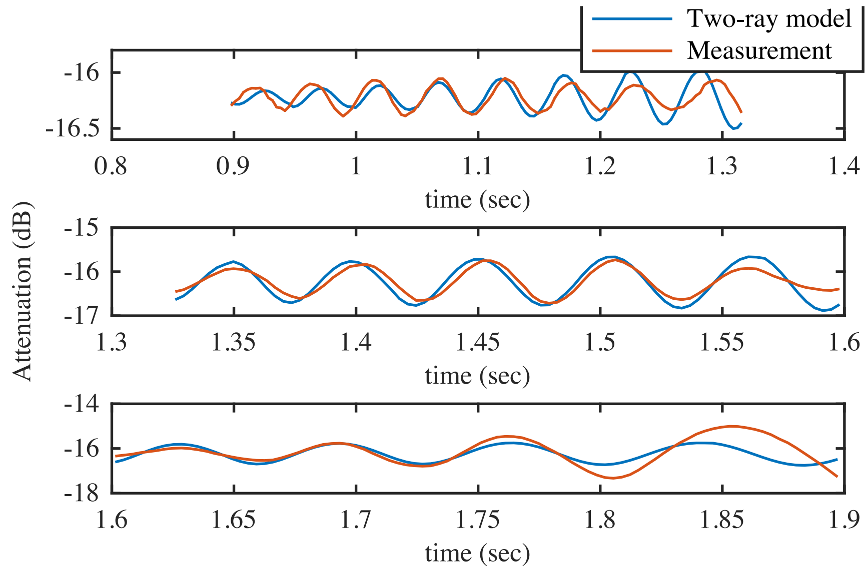

Figure 14 - Two-ray model vs Measurements Comparison for Regions: A1 (Top), A2 (Middle), and A3 (Bottom)

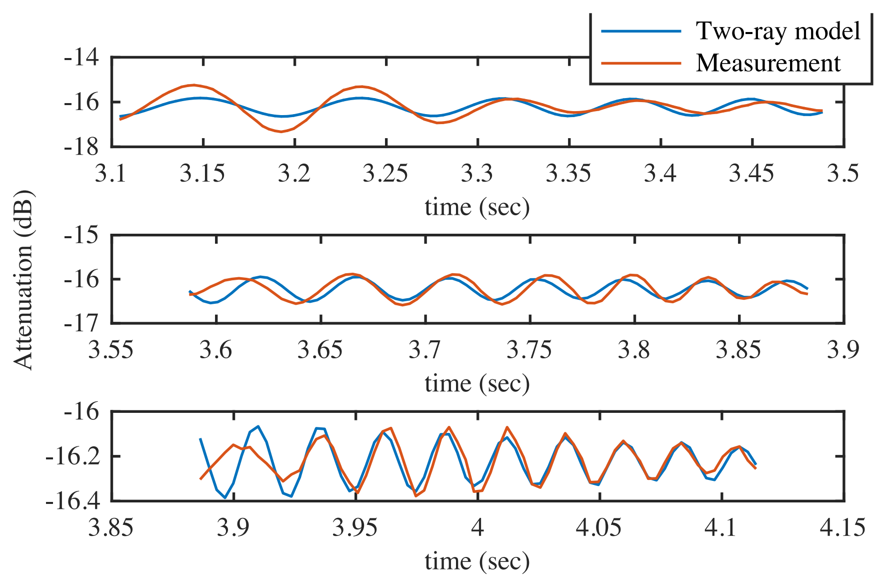

Figure 15 - Two-ray model vs Measurements Comparison for Regions: B1 (Top), B2 (Middle), and B3 (Bottom)

The value of this reflection coefficient (Γ) was estimated by fitting the two-ray model with the measurement data. Figure 14 shows the measurement and two-ray model comparison for the A1, A2, and A3 regions of the unshadow region; and Figure 15 shows the same comparison for regions B1, B2, and B3. A good fit is obtained for both cases by varying the value of the reflection coefficient. Similar analysis was conducted for several other measured shadowing events.

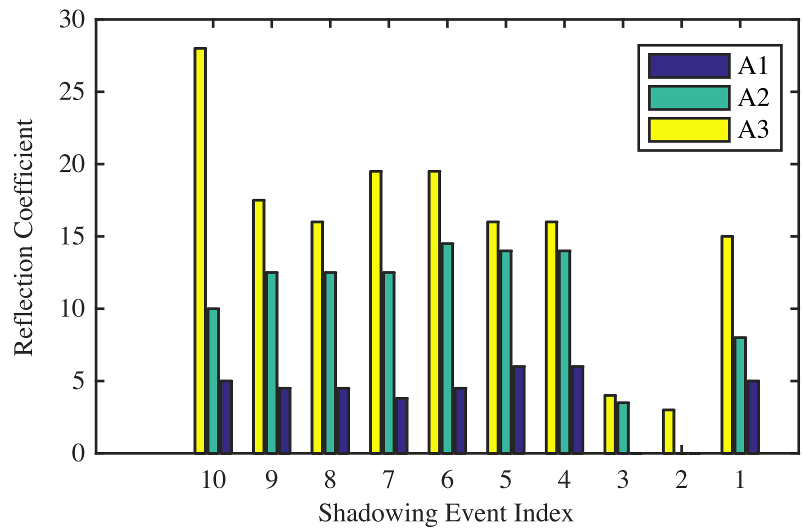

Figure 16 - Reflection Coefficient Values for the Left Unshadow Region

Overall, it was observed that the reflection coefficient generally changes every 0.3 s after the human starts walking and this was consistently observed across most scenarios. The value of the reflection coefficient was observed to increase as the reflected angle (θ) decreases and vice versa (8). The results corresponding to the reflection coefficient for six different shadowing events are shown in Figure 16 and Figure 17. Such a measurement-based model is of tremendous value for ray-tracing tools and MAC layer simulations.

$$\Gamma(d) = \begin{cases} 5, & 0.27 \le d \le 0.40 \\ 10, & 0.40 \le d \le 0.48 \\ 20, & 0.48 \le d \le 0.57 \\ 25, & 0.93 \le d \le 1.05 \\ 10, & 1.05 \le d \le 1.16 \\ 6, & 1.16 \le d \le 1.24 \end{cases} \tag{8}$$

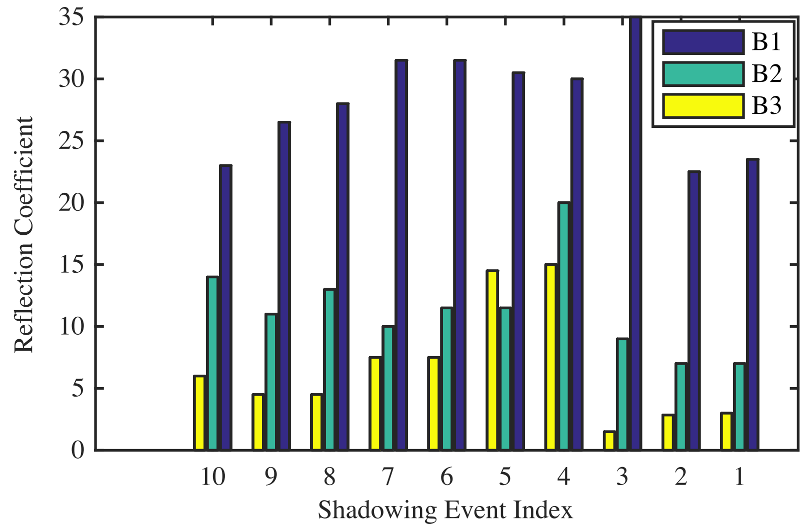

Figure 17 - Reflection Coefficient Values for the Right Unshadow Region

2.4.3 Shadow Region Analysis – DKED Evaluation and Doppler Shift Analysis

This section is devoted to characterizing the shadow region by first analyzing the Doppler shift due to the human body and then comparing the measured results with the DKED model. Doppler shift is defined as the rate of change of MPC path lengths. In order to assess the Doppler shift within the shadow region, Short-Term Fourier Transform of the shadowing event in time domain was obtained using 100 sector windows. This window was moved along by one sector in each iteration. The resulting responses for two of the 1399 sector windows are shown in Figure 18. These responses are shown in the Doppler domain and the peak values are extracted from each response corresponding to a sector window. This is done in order to understand the change in Doppler shift within the shadow region.

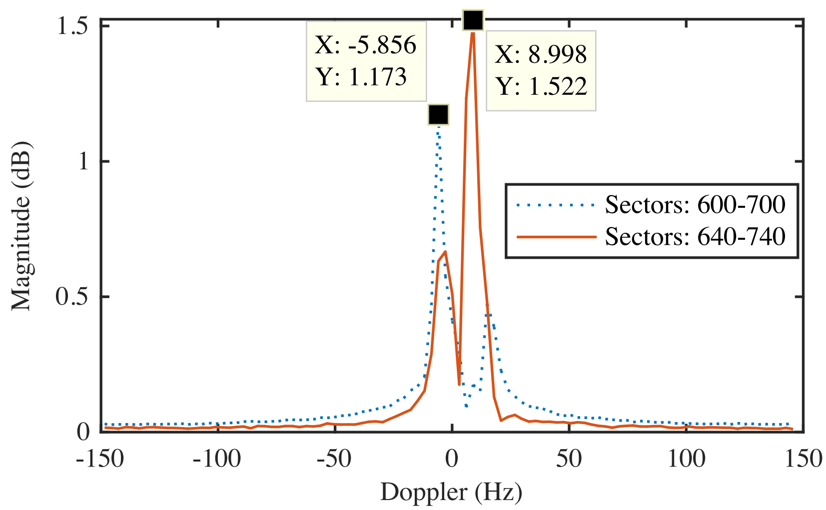

Figure 18 - Short term Fourier Transform of Shadowing Event - Doppler Frequency (Hz)

The peak from each response corresponding to the sector windows is shown in Figure 19. The change in Doppler due to front and back scatter from the human body is apparent in this figure. The human enters the shadow region at approximately sector 500, at which point the Doppler shift goes down. Once the human reaches the center of the shadow region where the LOS path is mostly blocked, the Doppler shift changes sign due to the switch from front to back scatter. After this point, the Doppler shift continues to go down as the human walks away from the LOS path. Although this figure shows 0 Doppler shift in the unshadow region, this is due to the fact that only the LOS path was observed in this figure. In reality, the Doppler shift in unshadow region would be much higher due to the rate of change of the reflected paths. In fact, reflection from the human body turns into diffraction when the Doppler shift is equal to 0.

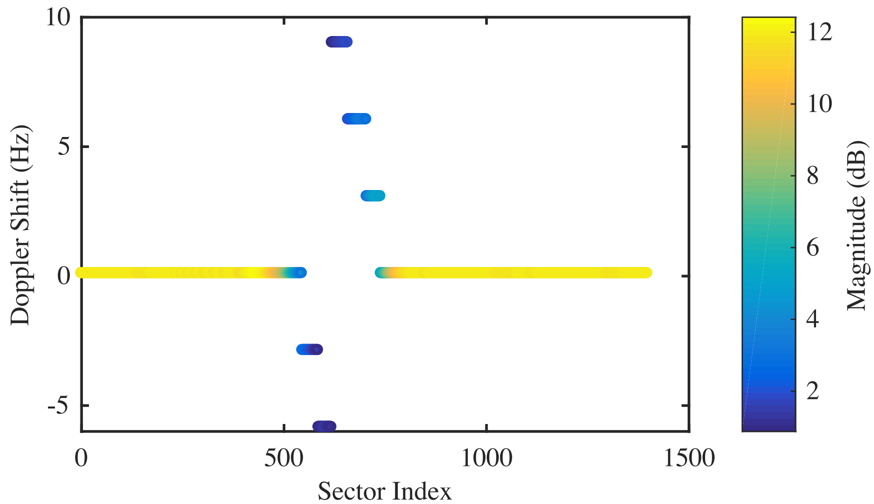

Figure 19 - Doppler Shift (Hz) vs Sectors

Double Knife-edge diffraction model was used to estimate the fading characteristics of the signal within the shadow region, as described in Section 2.2.3. DKED model comparison with the measurement results is shown in Figure 20 for six different shadowing events. Deep fades were observed in the DKED model which were overestimating the measured results. This may be due to destructive interference of the two diffracted rays from each side of the human body. A diffraction correction factor was used in order to correct this overestimation of energy within the shadow region.

This comparison was conducted on all 60 measured shadowing events. Due to the high-resolution measurements, all of the fading events were captured. The diffraction correction factor at different transmitter-receiver separation distances is given by,

$$\gamma = \begin{cases} 0.65, & d = 4m \\ 0.7, & d = 6m \\ 0.8, & d = 8m \end{cases} \tag{9}$$

It was realized that the diffraction correction factor (γ) was consistently the same for cases with different walking distance from the transmitter and for different human subjects and only changed with changes in transmitter-receiver separation distance (9).

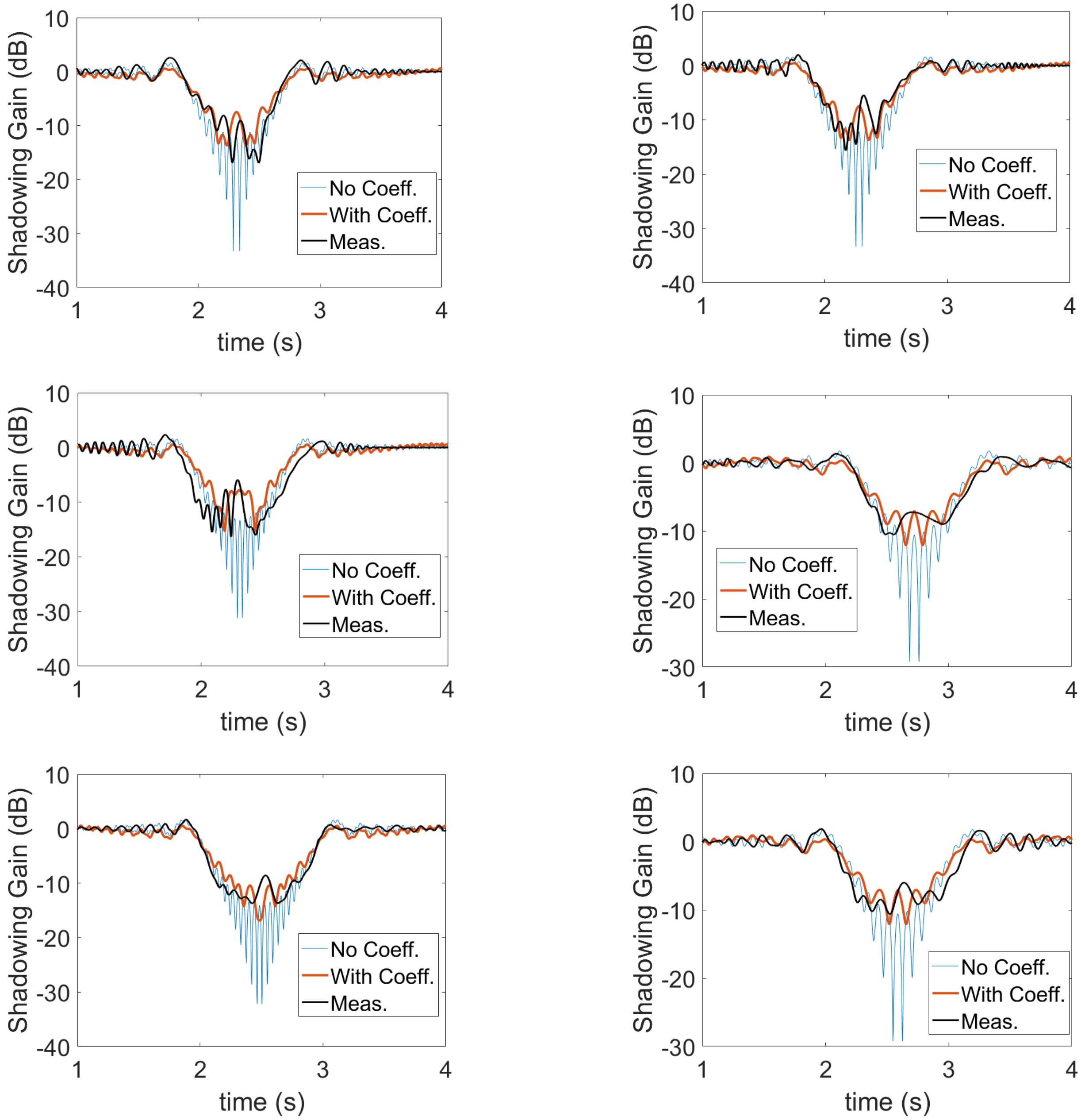

Figure 20 - Shadowing Events: Measurement vs DKED Model Comparison

2.5 Discussion

Previous efforts to develop both simulation and measurement-based models of the effect of human presence on mmWave propagation and radio access scenarios have yielded important and intermediate results but lack accuracy and/or generality. Their range of applicability is extremely limited. It is difficult to extrapolate channel response for a geometry of interest from a measured geometry unless the two are very similar. Here, we have proposed a physical-statistical model which combines both geometrical and measurement-based components which is both more accurate and more general than previous works.

Here, we model paths as the combination of direct path when present and the reflected and or diffracted that result from the interaction of the transmitting wave from the human body. The geometric component of our model accounts for the relative phase of each component and can be used to represent a large number of different configurations. The measurement-based component of our model captures the relative strength of each component with more reliability than purely simulation-based models. The overall model has two components: 1) the unshadow region of the blockage event is modeled using the two-ray model, and 2) the shadow region of the blockage event is modeled using the DKED model.

In order to come up with a statistically accurate model, up to sixty different shadowing events were captured. High resolution measurements allowed us to differentiate between reflected and diffracted paths during the shadowing event. Additional care was given during the measurements, by ensuring phase stability between samples; and constant walking speeds were ensured with the use of a metronome. As a measurement-verification step, the parameters of the pre-existing four state Markov model (fade depth, fade duration, and rise/decay rates) were analyzed for different shadowing events and were compared with previous studies. These parameters showed very good agreement with previous work conducted in similar environments. To further ensure that we are able to differentiate between the diffracted and reflected paths from the human body, we analyzed the Doppler shift within the shadow region. We were able to clearly show the resulting forward and back scatters from the human body in the Doppler spectrum.

The unshadow region of the overall blockage event was modeled using the two-ray model. The measurement-based component of this two-ray model, the reflection coefficient (Γ), was used to compute the strength of the reflected path within the unshadow region. It was realized that the reflection coefficient is distance dependent. The value of the reflection coefficient was observed to change every 0.1 m during the shadowing event. The resulting reflection coefficient values were consistent across multiple shadowing events with a very low standard deviation. The mean value for the reflection coefficient changed as follows across the 1.53 m long shadowing event: 5, 10, 20, 25, 10, and 6. The overall simulated response using the two-ray model matches very closely with the measurement results. This estimation of the reflection coefficient applies to several different blockage scenarios, including multiple human subjects, walking positions, and transmitter-receiver separation distances.

The Double Knife-Edge Diffraction (DKED) model was used to model the shadow region of the overall blockage event. The measurement-based component of the DKED model, the diffraction correction factor (γ), was used to compute the strength of the diffracted path within the shadow region. The derived value of the diffraction correction factor was observed to change as the transmitter-receiver separation distance changed. For 4 m, 6 m, and 8 m separation distances the value of the diffraction correction factor was 0.65, 0.7, and 0.8 respectively. For a given transmitter-receiver separation distance, the value of the diffraction correction factor was consistent for all scenarios which included, different human subjects and walking positions in between the transmitter and receiver. The overall simulated response using the DKED model matches very closely with the measurement results.

The final result is computationally efficient and can be used to accurately represent a large number of different blockage scenarios. It combines the best of simulation and measurement-based approaches, and will be a valuable tool for those engaged in the design and simulation of mmWave radio access networks which have the potential to be affected by human presence.

Although the model presented in this work accounts for wide range of geometries, more work can be done in the future to further improve the generality of the model. Future measurement campaigns for human presence may be conducted at multiple frequencies and account for different polarizations. Lastly, additional data with human subjects of different body types may be collected in the future for more comprehensive models.

Chapter 3: Statistical Modelling of Through-Wall Attenuation and Depolarization at 10 and 30 GHz

3.1 Introduction

As the emphasis of mmWave systems development transitions from point-to-point systems to Radio Access Networks (RANs) operating at street levels or indoor environments, the need to characterize through-wall attenuation due to both interior and exterior walls of buildings has achieved great significance. A complete statistical characterization of through-wall attenuation is highly desirable to support simulations of practical mm-wave wireless systems under realistic conditions, given the high penetration loss due to walls at mmWave frequencies.

In the past, a lot of work has been done on measuring electromagnetic properties of bulk materials, where the test is set-up in a lab as opposed to In-situ measurements. In [44], NIST provides a comprehensive report of such in-lab measurements, where the attenuation and dielectric properties of bulk materials (masonry, concrete, lumber, glass, drywall, etc.) has been provided. Although lab-based studies of bulk materials are useful, one must ultimately measure complex wall structures in realistic environments.

A lot of previous work has been done on measuring through-wall attenuation at microwave frequencies. Stone et al. conducted through-wall measurements in a lab environment at microwave bands and report attenuation and dielectric constants for building materials [44]. Kim et al. conducted 2.5 GHz ISM band measurements and report on the transmission and reflection characteristics of interior gypsum walls and concrete walls [41]. Landron et al. conducted microwave reflection coefficient measurements at 1.9 and 4 GHz at a variety of smooth and rough building materials, such as limestone, brick, and glass walls [42]. Similar measurements conducted at microwave frequency bands have been reported in [43]. Durgin et al. conducted penetration loss measurements at 5.85 GHz for indoor and exterior household walls [37].

In comparison to the through-wall measurements conducted at microwave bands, very little work has been done at mmWave bands. Anderson et al. conducted indoor propagation measurements at 2.5 GHz and 60 GHz [31]. This study provides measured attenuation data for common building materials, such as drywall, glass, whiteboard, etc. Similar measurements have also been performed in [34-36]. A more comprehensive study was conducted by Alejos et al. which investigates propagation mechanisms at 40 GHz [32]. This work analyzes different propagation mechanisms, such transmission, polarization, specular reflection, and wedge diffraction by means of various measurement campaigns. Zhao et al. measured reflection and penetration losses in and around buildings at 28 GHz [33]. Similar measurements were also performed in [39]. This work presents transmission and reflection measurements for exterior and interior building walls.

In the majority of the work cited above, both at micro- and mm-Wave bands, the focus has been on obtaining transmission and reflection coefficients by comparing measurement results with models such as Classic Fresnel theory, Internal Successive Reflection, or the Multilayer model. Since the goal of these studies was to estimate dielectric parameters of building materials, very little emphasis was placed on variations in through-wall attenuation that may be observed along a given wall and walls of different types. Such a statistical analysis would require large amounts of through-wall measurements, which would be a concern for measurements conducted at microwave bands employing large directional antennas.

In 2014, Ferreira et al. [30] conducted a literature survey of all the previous work done on electromagnetic characterization of building materials. The authors report on the shortcomings of the previous work done in this field. It was found that in most of the previous work, only a limited number of samples along a given wall were measured. Frequency dependence of dielectric parameters was not accurately estimated as the measurements were conducted only at a handful of frequencies that are close to each other. The authors also mention that very little detail regarding the building materials was provided in most studies. Overall, the authors conclude by suggesting that a more comprehensive study is required on this topic.

Knowledge of the dielectric properties of a superficial wall material is generally insufficient to predict relevant propagation behaviour as walls in general are multi-layered and quite complex. Overall, very little insight exists concerning the range of behavior or distribution either point-to-point on a given wall or between walls of broadly similar type. Intuition suggests that propagation characteristics will vary between general wall types, different walls of the same general type, and different locations on a given wall. These differences would be greatest for exterior walls, moderate for interior load bearing walls, and least for interior partition walls.

The objective of this work is to reveal the statistical distribution of through-wall attenuation, either point-to-point on a given wall or between walls of broadly similar type, the extent to which the distributions for different wall types overlap or are separable or distinguishable. To this end, we conducted through-wall attenuation and depolarization measurements at 10 and 30 GHz at tens of exterior, interior load bearing and interior partition walls around the University of British Columbia campus. Measurements were conducted at 22 different walls in 6 separate buildings. To accomplish this, we devised and assembled an automated test fixture that address most of the issues that make such a campaign challenging or time-consuming. Our results demonstrate that through-wall attenuation does fall into separable classes and are amenable to statistical characterization.

The remainder of this chapter is organized as follows: Section 3.2 describes the underlying concepts; Section 3.3 describes the measurement procedure and equipment; Section 3.4 provides the overall results; and Section 3.5 presents the final conclusions.

3.2 Concepts

The underlying concept of through-wall attenuation is straightforward. This sort of an analysis requires measurements to be conducted in free space environment first with transmit and receive antennas aligned with each other and then the measurements are repeated with the same setup but with a building material in between the transmitter and receiver. Free space measurements are conducted in a reflection free environment, in the sense that all of the surrounding scatterers are quite far from the measurement setup and have an excess delay which is much larger than the delay for specular reflections in an indoor propagation scenario. The free space path loss is given by,

$$PL_{FS} = \left(\frac{4\pi d}{\lambda}\right)^2 \tag{10}$$

where d is the antenna separation distance and lambda is the wavelength. The through-wall attenuation is calculated by simple dividing the received power, obtained when the wall is in the middle, with the free space received power. This is referred to as the 'free space' method for calibration and has been used quite extensively in previous studies.

However, previous work of this nature has received quite a lot of criticism for conducting not so comprehensive measurements and also for overlooking potential sources of error. In order to assess the statistical variability of through-wall attenuation on a given wall it is critical to measure at numerous locations on a given wall and repeat this on many walls of similar construction. Majority of the previous studies have reported anecdotal measurements where they have measured very few samples on a given wall. We have addressed this concern by conducting measurements at 40 different locations on a given wall, as shown in Figure 21.

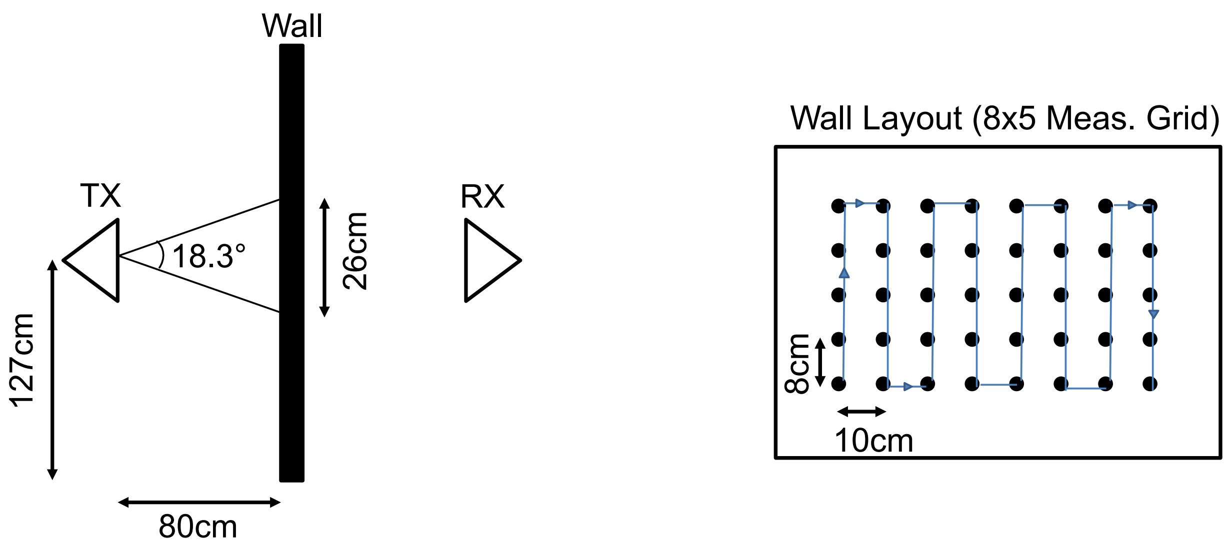

Figure 21 – Through Wall Measurement Grid and Setup

Another source of error that is generally overlooked is ensuring that the antenna to wall distance is in the far field such that d >> λ in (10). In our measurements, we not only made sure that the setup meets the far-field requirement but also ensured that the measurement grid is set up in such a way such that the first Fresnel ellipsoid is contained within the measurement grid at all points (Figure 21). This was done to ensure that any reflection or diffraction from other scatterers in the environment is minimized.

Several previous studies have done such measurements by changing the antenna positions manually along the wall. This can lead to significant positioning uncertainty and generate misleading results. Such measurements are best done using an automated test fixture like ours. This ensures that the transmit and receive antennas are completely aligned at all measured locations along the wall. With an automated test fixture, the alignment process takes place only once and that is at the start of the measurements. Once the antennas are aligned they remain aligned throughout the measurement process as the antennas move along the grid pattern shown in Figure 21. Several checks were made in order to ensure that the antennas are aligned at the beginning of the measurements. These antenna alignment checks were made using tape measures, laser pointer, and bubble levels.

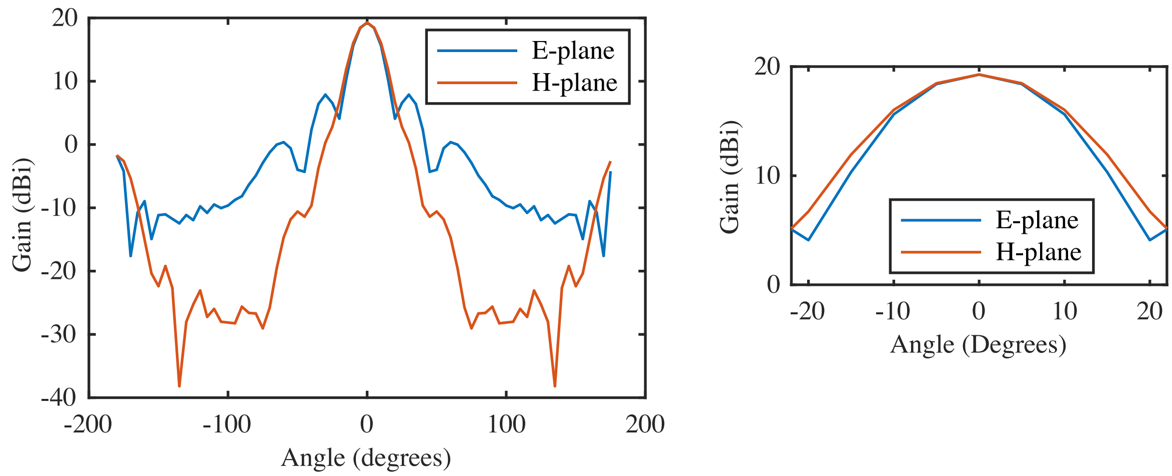

Figure 22 - Antenna Pattern: Overall (Left); Zoomed In (Right)

However, it is possible for antenna orientations to slightly change during the measurements due to vibrations from the moving bi-sliders. We have ensured that these subtle changes in antenna orientation won't have a big impact on the through-wall calculations by analyzing the antenna patterns. As shown in Figure 22, misalignment of antennas by as much as 10° would only cause a 2-dB mismatch. The antenna pattern clearly shows that the antennas on the transmit and receive sides would have to be misaligned by more than 10° in order to get any significant errors in the measured received power.

Such measurements can produce misleading results if proper care is not given during the measurement process. At each stage of the measurement campaign we have not only identified potential sources of error but also found ways to mitigate them. Since the measurements were conducted by following the same grid pattern consistently, it was very easy for us to spot any outliers such as metal clad door knobs on wood doors, glass panes on metal clad doors, etc.

Lastly, the overall channel sounder was configured to do measurements in the most accurate and efficient manner (refer to Section 3.3). The channel sounder was automated to simultaneously collect measurements at 10 and 30 GHz for all four polarization combinations (V-V, V-H, H-V, H-H). The entire measurement sequence was completely automated to avoid any human errors.

3.3 Methodology

Insertion loss of different building materials was measured at a variety of buildings on the campus of the University of British Columbia. Common building materials measured in this study include, glass (clear, frosted, and with mesh), wood, brick, concrete, drywall, and metal clad. A total of 22 different walls were measured in 6 different buildings across the UBC campus (Figure 23). A statistically accurate model requires that measurements are conducted in a bevy of different types of buildings with different building materials.

For each building material, approximately 4 or 5 walls of different levels of thickness were measured, as summarized in Table 2. On a given wall, 40 different points were measured such that the overall model is statistically accurate.

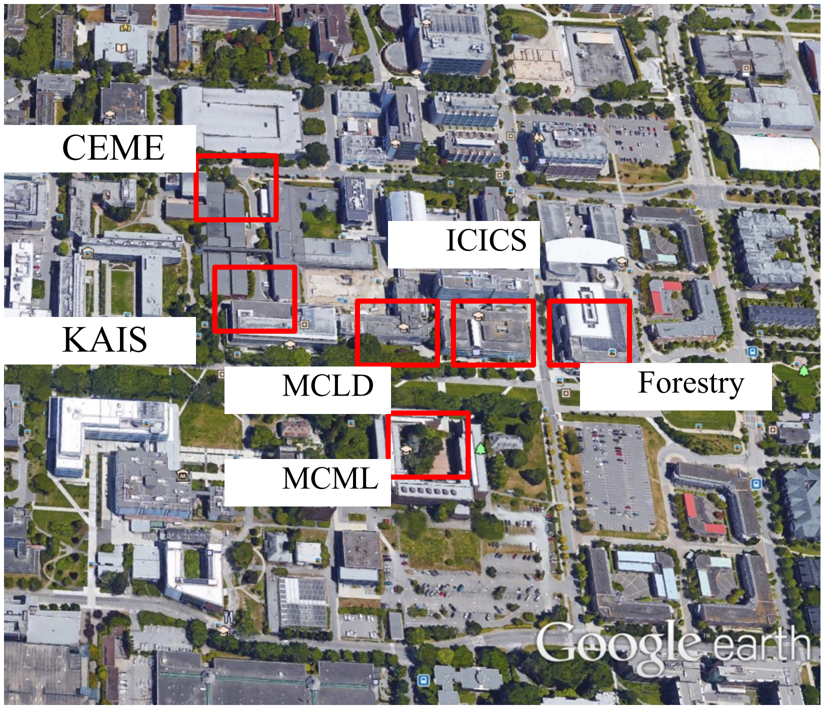

Figure 23 - Measurement Locations on UBC Campus

Table 2 - Summary of Building Materials and their Thickness

Materials	Thickness (cm)	Number of walls
Wood	4.5 - 5	4
Drywall	12.6 - 20	5
Concrete/Brick	30 - 65	4
Glass	2.5 - 6	4
Metal Clad	4.25 - 6	5

3.3.1 Channel Sounder Specifications

A VNA-based channel sounder was utilized for the measurement campaign. Configurations of the two different RF front ends used for the 30 GHz and 10 GHz measurements can be seen in Figure 24. The channel sounder has a temporal resolution of 1ns with a maximum dynamic range of approximately 40 dB for 10 GHz and 30 dB for 30 GHz case. The frequency sweep of the VNA was set to 9.5-10.5 GHz for X band. The power is transferred to transmit side using a set of Miteq RF to Fibre Transceiver units (100 MHz to 11 GHz frequency span). The fibre cables used for this setup were 10 m in length and had high phase stability.

The channel sounder was automated to simultaneously collect measurements at 10 and 30 GHz for all four polarization combinations (V-V, V-H, H-V, H-H), as shown in Figure 24. For Ka band measurements, a set of up convertor and down convertor is used to increase the IF frequency (750 – 1750 MHz) to millimetre wave range (29.3-30.3 GHz) and then bring it back to the IF range using an LO of 28.55 GHz. The power from port one of the VNA is transferred to the block up convertor using the second set of Miteq RF to fibre transceiver unit (10 MHz to 6 GHz band width). To have synchronization between BUC and Receiver, the attenuated 10 MHz reference signal generated by VNA is injected to the fibre link (using bias T) and delivered to transmit side. After amplification, the 10 MHz signal is then re-injected to BUC along with 24 V DC power using bias T.

In Both X band and Ka band cases, 801 frequency points were utilized at each sweep and the IF bandwidth is set to 1 kHz. The transmitter and the receiver utilized pyramidal horn antennas which had a gain of 18 dBi for X band and 20 dBi for Ka band antenna and HPBW beam-widths of 20°. Both antennas at transmit and receive sides were vertically polarized and the heights were set to 1m (few exceptions). The maximum EIRP for both X and Ka band cases was set to 38dBm. Lowest detectable power was used in order to reduce the chance of getting MPCs from the surrounding environment. However, transmit power was increased for cases (masonry and concrete) where too much attenuation was experienced.

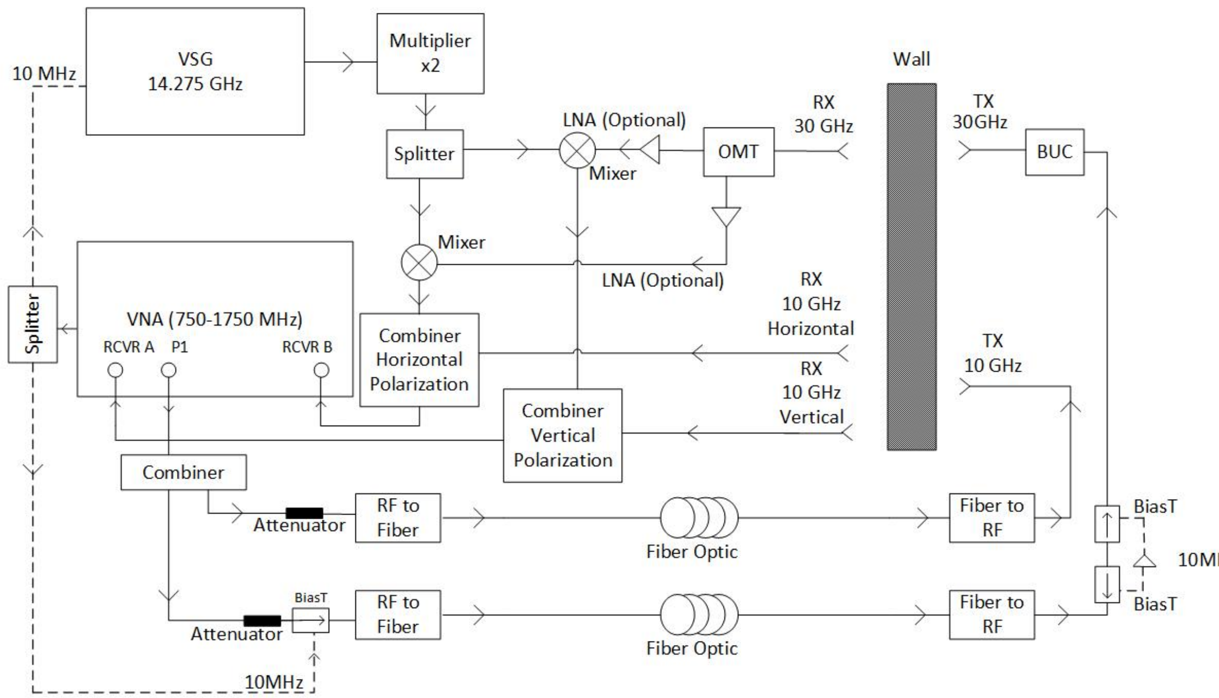

Figure 24 - Channel Sounder Configuration for Through Wall Measurements

3.3.2 Automated Test Fixture

The automated test fixtures used for these measurements are shown in Figure 26 (transmit side) and in Figure 25 (receiver side). In an attempt to create a very efficient measurement campaign, a lot of emphasis was placed on automating 10 and 30 GHz measurements. Horizontal and vertical bi-sliders were utilized in order to carry out the measurements in an 8x5 grid sequence as shown in Figure 21. Special antenna mounts were designed in order to attach both the 10 and 30 GHz antennas onto the vertical bi-slider. The mounts had a very robust design to be able to absorb any sort of vibrations during the measurement sequence.

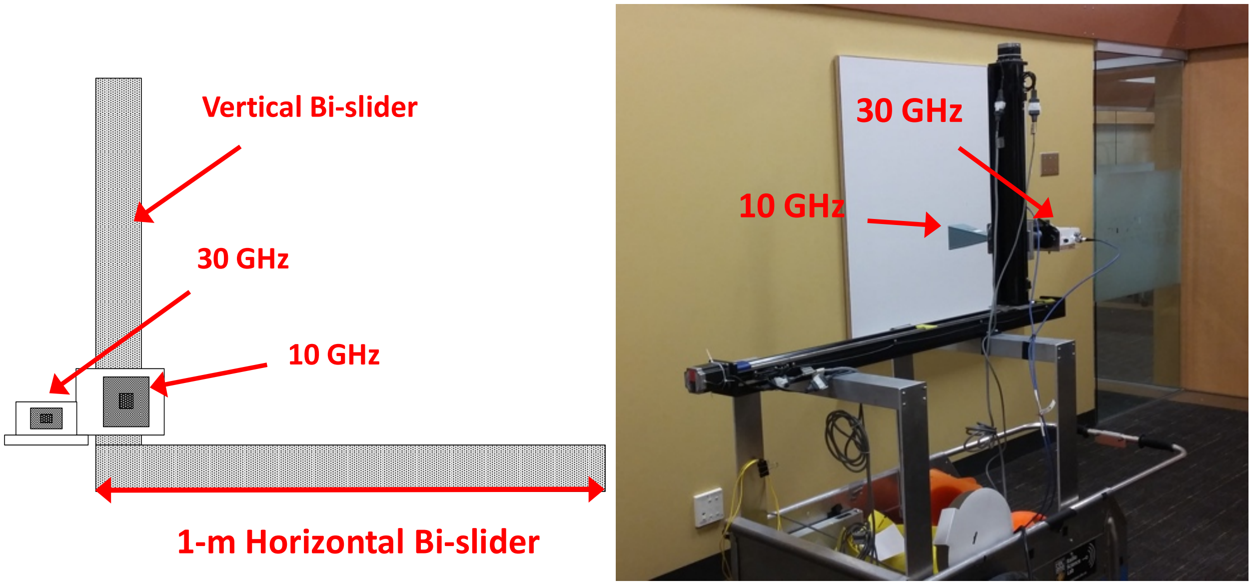

Figure 26 - Channel Sounder Transmitter Configuration

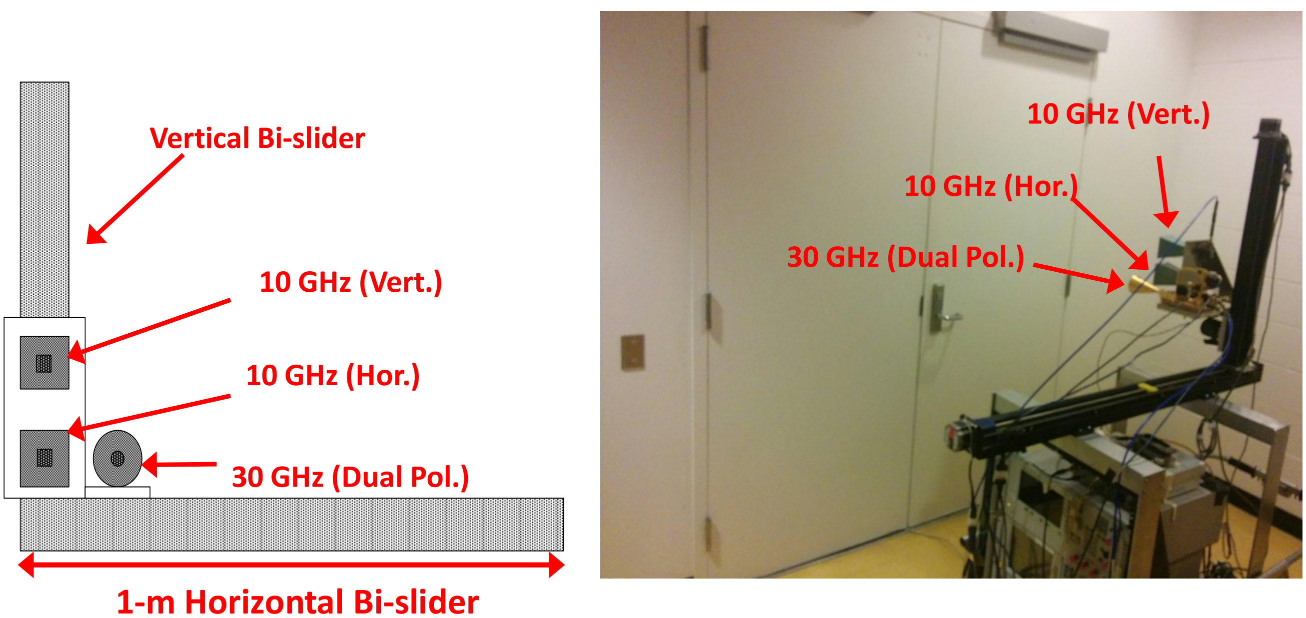

Figure 25 - Channel Sounder Receiver Configuration

3.3.3 System Calibration and Data Collection

Calibration of the system is done in order to remove the frequency depended distortions due to system and other in-chain apparatus. For the case of Wall Loss, the standard equalization process for calibration is not necessary. This is because wall loss is calculated using the 'free space' calibration method as described in (11),

$$\boldsymbol{S_{21}^{Wall}} = \frac{\dfrac{\boldsymbol{S_{21}^{Meas}} \times \boldsymbol{S_{21}^{Cable}} \times \boldsymbol{S_{21}^{Att}}}{\boldsymbol{S_{21}^{Cal}}}}{\dfrac{\boldsymbol{S_{21}^{FS}} \times \boldsymbol{S_{21}^{Cable}} \times \boldsymbol{S_{21}^{Att}}}{\boldsymbol{S_{21}^{Cal}}}} = \frac{\boldsymbol{S_{21}^{Meas}}}{\boldsymbol{S_{21}^{FS}}} \tag{11}$$

where S_{21}^{Wall} is the through-wall attenuation; S_{21}^{Meas} is the received power in wall measurements; and S_{21}^{FS} is the received power in free space measurements; and S_{21}^{Cable} and S_{21}^{Atten} are the frequency responses for cable and attenuators used during the calibration process. This process removes the free space loss and system effect from the measured data all together.

Measurement data was recorded using the linear measurement tracks (bi-sliders). The set of Velmex bi-sliders which were set in x-z formation were connected serially to a laptop. Each track is 50cm long and has a positioning accuracy of +/-5µm. 5 different locations were measured along each track with a 100mm separation between successive measurements. At each position along the wall, 10 different PDPs were recorded. A Matlab script was developed in order to control the bi-sliders, and process the measurement data.

Free space path loss data was also generated using the same setup as the wall loss measurements. Free space measurements were conducted in a reflection free environment (Building rooftops). In this scenario, all the surrounding objects were quite far from the setup and had an excess delay which is much larger than the indoor propagation scenario. The excess delay can be easily removed using time domain techniques. For the free space scenario, the bi-slider conducts measurements in the same 8x5 grid as the through-wall measurements.

Based on the recorded data, multipath reflections (MPCs) can be characterized in two main categories: reflections from other scatterers and reflections within the wall. Reflections from other scatterers have a much longer delay compared to the reflections within the wall. Time domain gating was attempted in order to eliminate the reflections with a longer delay. This technique suppresses all the signals that are not direct transmission through the wall. However, we did not see any big changes in the through-wall attenuation calculations as the power in those secondary paths was too low to have any impact.

Through-wall attenuation measurement data was recorded as an 8x5 matrix, corresponding to the grid shown in Figure 21. The 8x5 matrix represents the s-parameters extracted from the VNA corresponding to the received power. At each one of these measurement positions, 10 traces (801 frequency points) of S_{21} measurements are collected. The 10 traces are then linearly averaged, resulting in a single S_{21} frequency response. This process is then repeated for each position measured along the track. System calibration is then applied to the measurement response according to (11).

3.4 Results

Histograms corresponding to penetration losses measured at four different wood walls are shown in Figure 27. The observed distributions are mostly Gaussian, although a better fit can be achieved with greater number of measured data points along a given wall. Similar distributions were observed for all of the other materials as well.

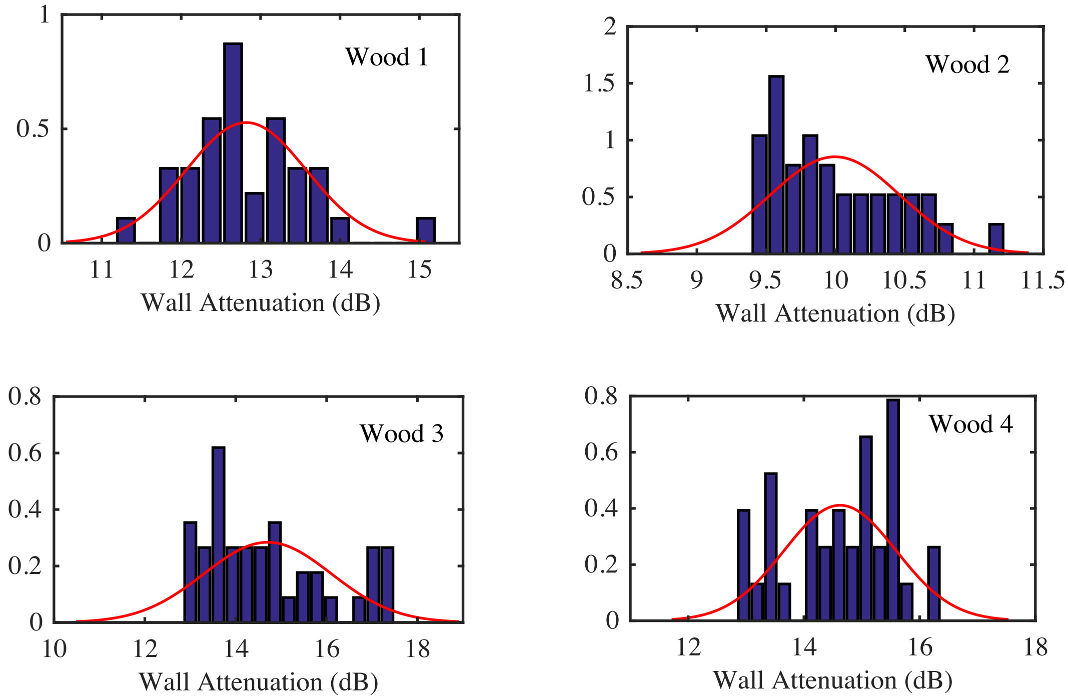

Figure 27 – Through Wall Attenuation for Wood Walls at 30 GHz

Figure 28 - Figure 32 demonstrate the variations in through-wall attenuation (dB) between general wall types, different walls of the same general type, and different locations on a given wall. Distributions corresponding to wall attenuation measured at each wall is shown and, in each case, multiple categories of attenuation can be observed. All of the distributions presented in this figure correspond to the 30 GHz V-V polarization measurements except for Masonry/Cement, for which 10 GHz data is shown. For the case of wood walls, ‘wood2’ shows very little variability in attenuation for points measured along the structure as it is one of those indoor wood doors that are mostly hollow. The rest of the wood doors show a little bit higher variation but very similar and overlapping attenuation values.

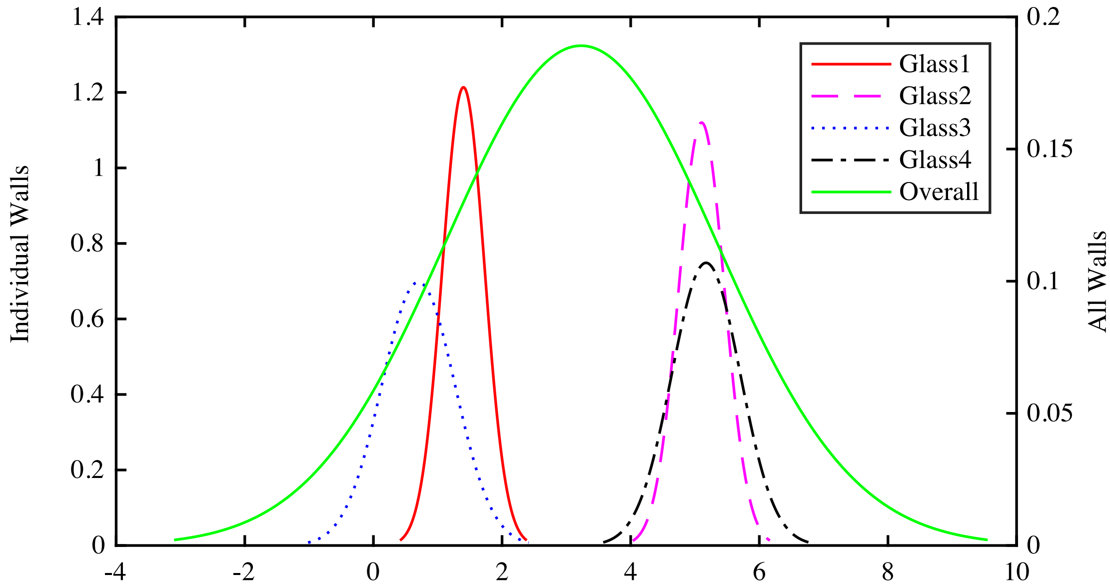

Figure 28 - Through Wall Attenuation (dB) Distributions for Glass Walls

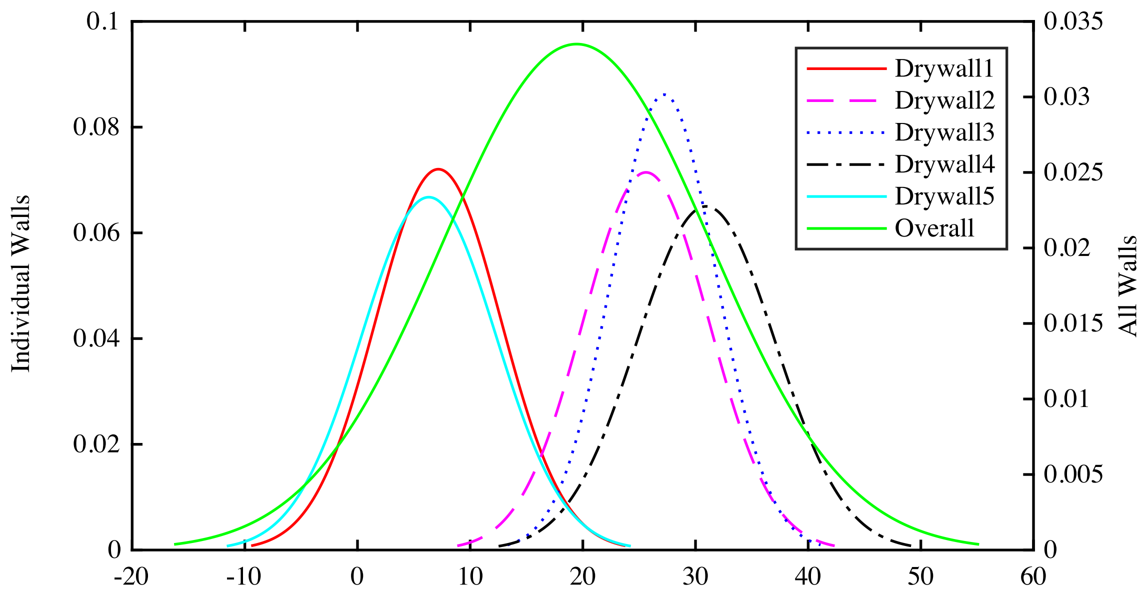

Figure 29 - Through Wall Attenuation (dB) Distributions for Drywalls

Standard deviation in metal clad doors was fairly low except for ‘metal3’, which was high due to the vertical glass panes in the middle of the door Figure 30. In the case of glass, several different kinds of glass partitions were measured, such as tinted glass, frosted glass, clear glass, and glass with metal mesh. The distributions suggest two different categories for glass, where frosted and mesh glass show slightly higher attenuation than clear and tinted glass (Figure 28). The level of coating on a tinted/frosted glass determines the amount of attenuation. In this case, tinted glass had very little coating on it which is why it shows similar level of attenuation as the clear glass.

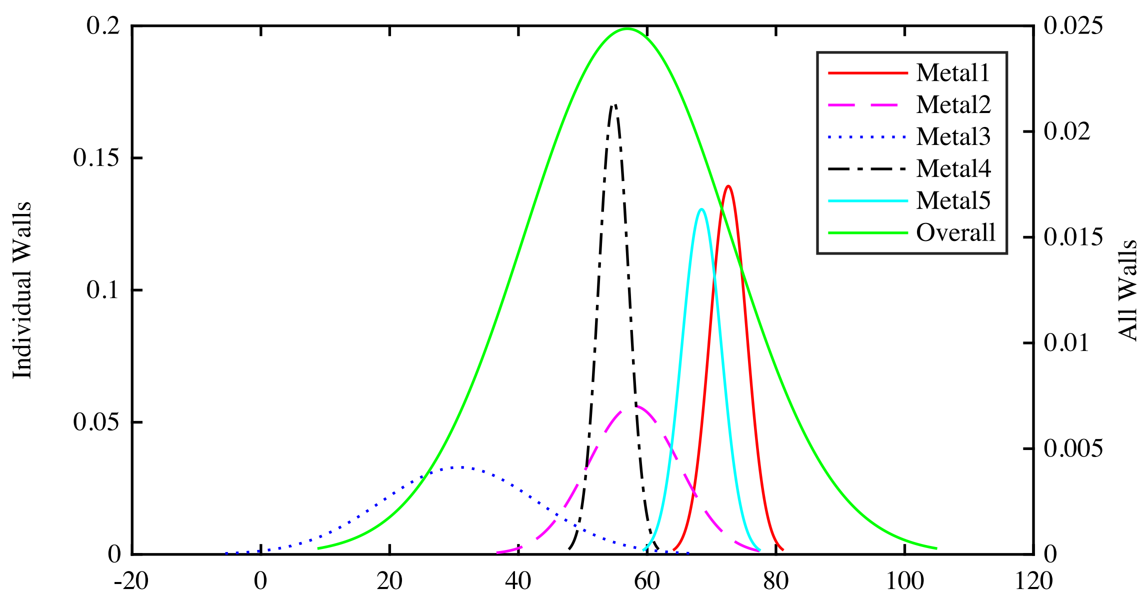

Figure 30 - Through Wall Attenuation (dB) Distributions for Metal

As shown in Figure 29, indoor walls or drywalls also display two different categories. Drywalls 1 and 5 are mostly hollow indoor walls, whereas drywalls 2, 3, and 4 are more complex load-bearing indoor walls that include, metal mesh, concrete pillars, etc. This explains why drywalls 1 and 5 show lower attenuation than drywalls 2, 3, and 4.

Figure 32 shows distributions obtained from Masonry/Cement walls at 10 GHz. Masonry/Cement walls in general show very similar mean and standard deviation values as most of these walls are not very complex and designed in a similar manner.

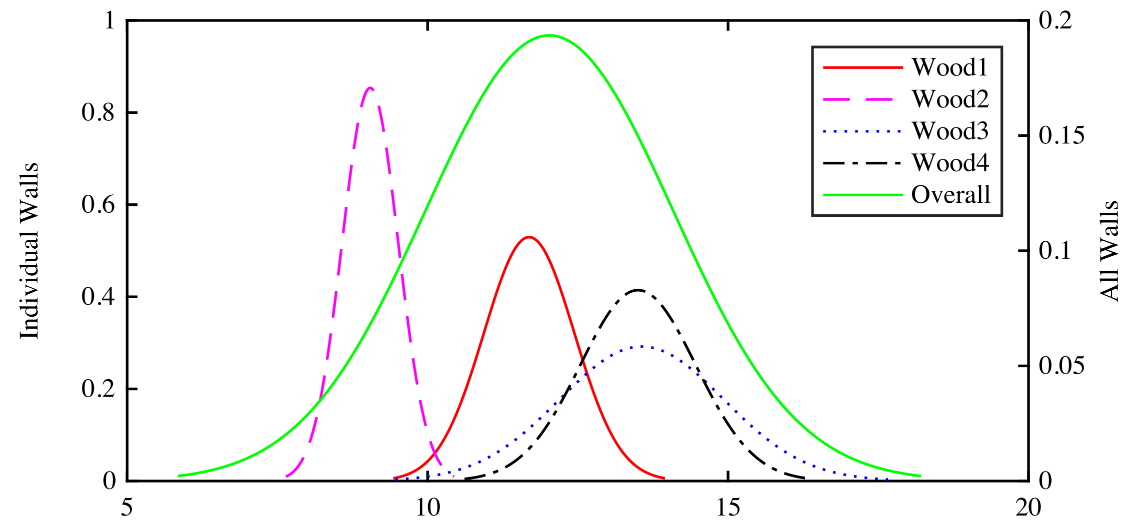

Figure 31 - Through Wall Attenuation (dB) Distributions for Wood

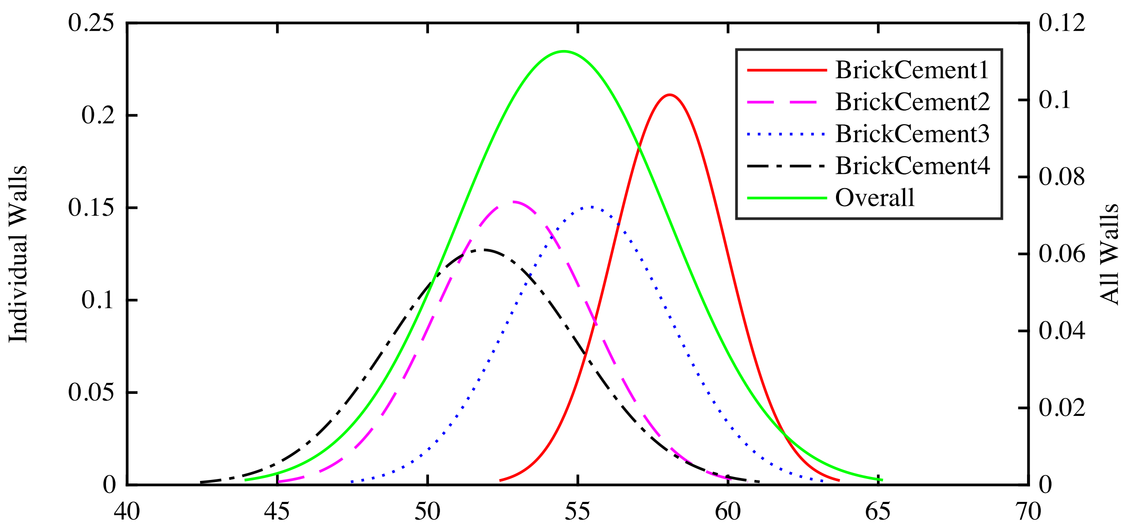

Figure 32 - Through Wall Attenuation (dB) Distributions for Brick/Cement

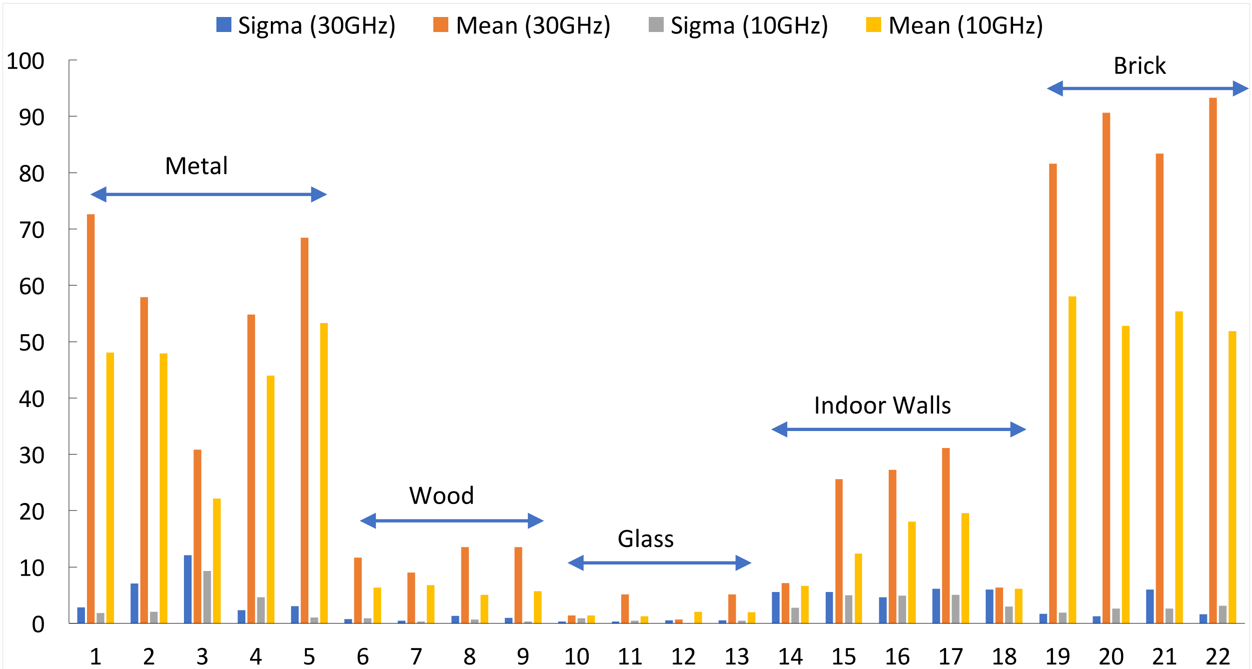

Figure 33 - Mean and Std of Wall Attenuation at 10 and 30 GHz (V-V polarization)

Figure 33 shows mean and standard deviation values derived from attenuation distributions at 10 and 30 GHz, just like the ones shown in Figure 28 - Figure 32. Five different categories of attenuation are clearly observed in this figure and are as expected. Brick walls show most attenuation followed by metal clad, indoor walls, wood and lastly glass, which shows the least amount of attenuation. Another observation that can be derived from Figure 33 is that penetration loss at 10 GHz is significantly smaller than penetration loss at 30 GHz in all materials. Standard deviation provides an estimate of point-to-point variability along a given wall. Large variability is observed in certain metal doors and indoor walls. For metal doors variability is observed due to gaps in the middle and edges of the doors where measured attenuation is less than the metal itself. In the case of 'metal 3' (refer to Appendix B), the metal door had small glass windows which resulted in lower attenuation as compared to other meter clad. In the case of indoor walls, variability was observed due to the complex interior structure of these walls, that include metal mesh, electrical wires, cinderblocks, etc.

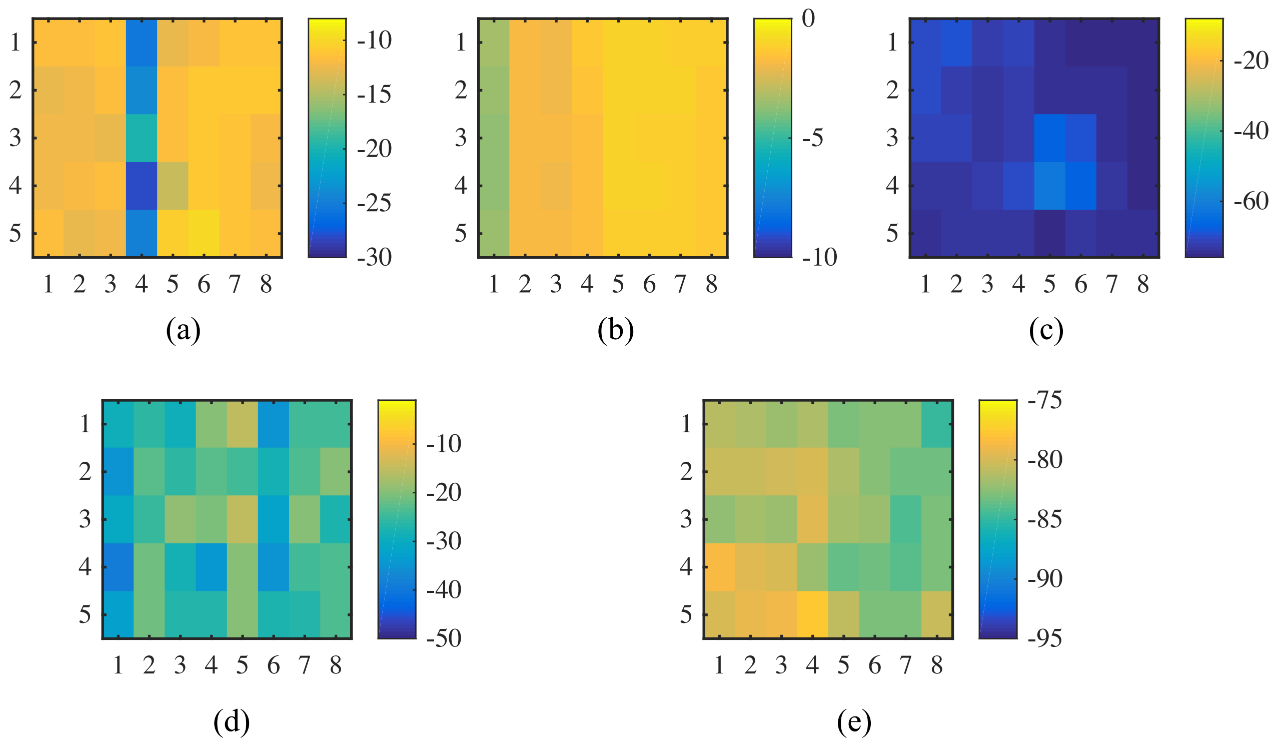

Figure 34 - Point-to-Point Variability across Wall: (a) Wood; (b) Glass; (c) Metal clad; (d) Drywall; (e) Brick/Cement

Point-to-point variability across a given wall are further analyzed using false color maps shown in Figure 34. Each figure shows 8x5 measurement grid and the color represent the measured attenuation (in dB) at that particular point along the wall. In the case of metal clad, a drop off in attenuation is observed near the center of the measurement grid. This is due to the gap right through the center of that particular metal door. For glass, there is a vertical column to the left with high attenuation and this is due to a wooden stud at the edge of the glass pane. In the case of wood, there is again a vertical column with high attenuation which was caused by a metal door opener. Very little variation was observed in brick and this finding is consistent with the in-situ work reported in [44]. Relatively high level of variability was observed for drywall. This is likely due to complex interior structures of the indoor walls containing metal mesh, electrical wires, cinderblocks, etc.

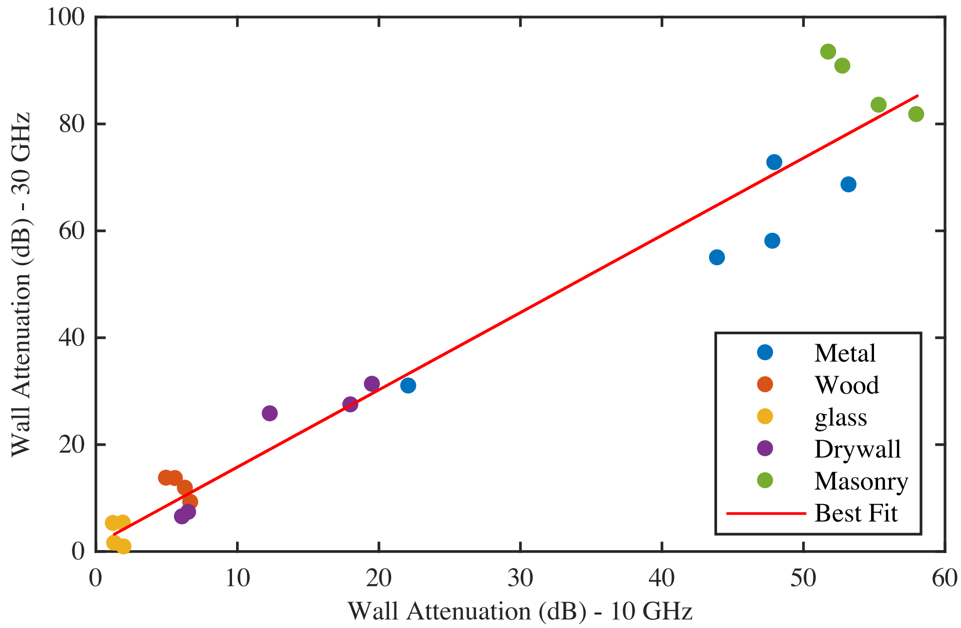

Figure 35 - Frequency Dependence of Wall Attenuation at 10 and 30 GHz

Figure 35 shows positive correlation between 10 and 30 GHz through-wall attenuation values (mean) in all building materials. The best fit line slope of 1.45 implies frequency dependence of the form of $f^{1.45}$ between 10 and 30 GHz through-wall attenuation (linear) values corresponding to metal, wood, glass, drywall, and masonry.

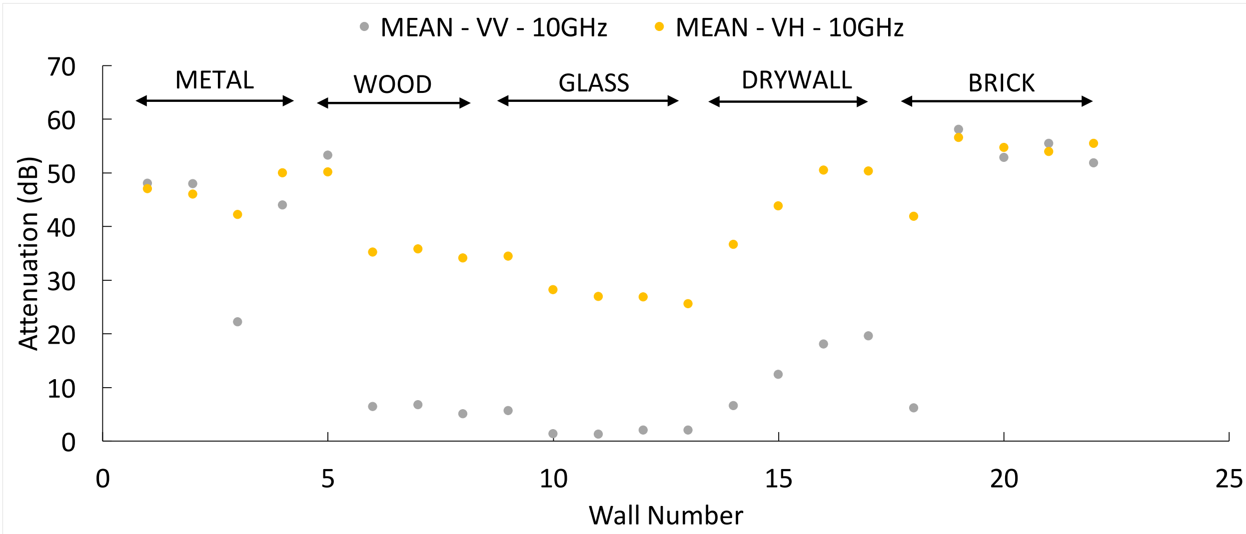

Figure 36 – Through Wall Attenuation Mean at Individual Walls: VV and VH Polarizations

Figure 36 compares the co-polar (VV) and cross-polar (VH) results for mean through-wall attenuation. V-V corresponds to the scenario where both transmit and receive antennas are oriented vertically; whereas V-H corresponds to vertical polarization at the transmit and horizontal polarization at the receiver. As expected, much higher attenuation is observed in cross polar scenarios as compared to the VV results due to the difference in antenna orientation at the transmit and receive. It is clear that cross-polar results scale (attenuation) comparably with their co-polar counter parts. Therefore, the five distinct categories observed in the co-polar results (Figure 33) carry over to the cross-polar results as well. The difference between the co-polar and cross-polar results, also known as the cross-polarization factor (XPD) is observed to be high in materials like wood, glass, and drywall.

3.5 Discussion

Through-wall attenuation is one of the key issues for indoor mmWave propagation. Given the high penetration loss at mmWave frequencies, designers urgently need a complete statistical characterization of through-wall attenuation. Knowledge of the statistical variation of through-wall attenuation is especially significant for realistic assessment of both the coverage of, and interference between, mmWave systems that operate in indoor and/or indoor-outdoor environments.

In this work, our objective was to reveal the distribution of through-wall attenuation, either point-to-point on a given wall or between walls of broadly similar type, the extent to which the distributions for different wall types overlap or are separable or distinguishable. We conducted through-wall attenuation and depolarization measurements at 10 and 30 GHz at tens of exterior, interior load bearing and interior partition walls around the University of British Columbia campus.

To accomplish this, we devised and assembled an automated test fixture that address most of the issues that make such a campaign challenging or time-consuming. Although measurements of this kind may seem to be error prone to a casual reader, it was realized that with the correct implementation of the measurement equipment such measurements can be conducted in a very efficient and accurate manner.

Our results demonstrate that through-wall attenuation does fall into separable classes and is amenable to statistical characterization. Mean values for through-wall attenuation observed at different walls are clearly divided into five quite separable categories based on building materials. The observed mean values for each building materials at 30 GHz are as expected with brick walls showing the most attenuation (84 dB) followed by metal clad (58 dB), indoor walls (20 dB), wood (12.5 dB) and lastly glass (3 dB), which shows the least amount of attenuation. High standard deviation is observed in certain metal clad and indoor walls. For metal doors variability is observed due to gaps in the middle and edges of the doors. In the case of indoor walls, variability was observed due to the complex interior structure of these walls that include metal mesh, electrical wires, cinderblocks, etc. Mean values for all walls of similar building material were mostly consistent once the outliers (as described previously) are accounted for. The through-wall attenuation distributions for each wall were mostly Gaussian.

We observed that through-wall attenuation at 10 GHz is significantly smaller than penetration loss at 30 GHz in all materials. A high positive correlation is observed between 10- and 30-GHz through-wall attenuation values in all building materials with a best fit line slope of 1.45. The best fit line slope of 1.45 implies frequency dependence of the form of $f^{1.45}$ between 10 and 30 GHz through-wall attenuation (linear) values. As expected, much higher attenuation is observed in cross polar scenarios as compared to the co-polar results due to the difference in antenna orientation at transmitter and receiver. The difference between the co-polar and cross-polar results (cross-polarization factor) is observed to be quite high (15 – 30 dB) in materials like wood, glass, and drywall.

This work will be of tremendous value to those who need to conduct system level studies or ray tracing based simulations of indoor and indoor-outdoor wireless communications systems. This work was done to show the feasibility of such measurements and also to demonstrate trends and patterns that haven't been previously analyzed. Future work can be expanded to include reflection and oblique incident measurements. Frequency dependence of dielectric parameters can be further analyzed by conducting similar measurements at 60 GHz. Future production measurement runs may take this work forward by conducting similar measurements presented here, at a much larger scale.

Chapter 4: Quality Assessment of Alternative Paths in Indoor and Outdoor Environments at 28 GHz

4.1 Introduction

At millimetre-wave frequencies, directional antennas are commonly used to ensure adequate received signal. The need for directional antennas introduces additional complexity but is necessary to close the link budget. Although mmWave links have been used for point-to-point transmission between hubs under free space conditions for many years, interest in using mmWave links in radio access networks (RAN) is much more recent. Such networks are characterized by multiple user equipment (UE) that establish communication either with one or more base stations (BTS) or with each other.

For radio access networks, directional antennas must be steerable. Mechanical steering is expensive since it is extremely cumbersome. Phased arrays, on the other hand, can exploit transmit and receive beam steering to add link gain. Steerable paths have been one out of the two principle schemes for mmWave access and form the basis for several previous standards including IEEE 802.15.3c [61], IEEE 802.11ad [62], and WirelessHD [63]. Over the past several decades a lot of work has been done on hardware and algorithms required for effective beam steering. [84] provides an overview of the technological advances in mmWave circuit components and antennas and the authors show the vast amount of work that has been done on 60 GHz chipsets. CMOS chips using steerable antenna arrays are now low cost and commercially viable.

Similarly, a considerable amount of work has been done on implementing algorithms for effective beam steering. To conduct accurate beam forming, DOD-DOA information is required which is generally obtained from beam training. The very first beam training schemes were demonstrated in IEEE 802.15.3c [61] and IEEE 802.11ad [62]. Similar beam training schemes have recently been reported in [47][81-90]. Most schemes reported in the literature are based on the two-stage beam training; where a very coarse beam is used to scan the channel for the strongest path and then in the second stage a much finer beam is used.

Beam training ensures that communication between the transmitter-receiver pair has been established. However, in dynamic channels it is necessary to be able to effectively track terminal rotation or translation [64-70]. [69] demonstrates beamforming protocol that doesn't require any complicated angular estimation. Similar work in [80] and [81] demonstrate the use sensors such as accelerometers and magnetometers for beam tracking. Kalman filters have been proven to provide accurate tracking in both slow and dynamic channels, as shown in [82] and [83].

Although a lot of emphasis has been placed on hardware and algorithms required for beam steering, very little effort has been allocated towards determining the quality of the secondary paths. In [65], MacCartney et al. conduct outdoor channel measurements at 16 different transmitter-receiver configurations in order to assess the NLOS paths. At each transmitter-receiver combination, complete azimuth sweeps are conducted, and a PDP is recorded at every 15° increment. Similar measurements are reported in [45] [46] [48] [49] [51]- [55] [57] and typical results are presented in the form of path loss – distance [50]; DOA polar plots; and RMS delay and angular distributions.

Majority of the previous work mentioned above, reports on the path loss and range of coverage at mmWave frequencies but few if any results capture the relative capability of direct and secondary paths. Previous standards, e.g., IEEE 802.15.3c [61], IEEE 802.11ad [62], and WirelessHD [63], have assumed that secondary paths exist but few previous works have considered their quality and capacity. This leads to a lack of understanding of the alternative paths and explains why previous standards haven't been widely adopted (ex. Wireless HD). Algorithms regarding beamforming may be able to track secondary paths but if information regarding the quality of these secondary path is not available, it puts a system-level designer in a very uncomfortable position. The work presented in this chapter tries to fill this void by assessing the relative quality and capacity of direct and secondary paths at millimetre-wave frequencies and, as a consequence, the performance that can be achieved when using beam forming in radio access environments.

This was achieved by conducting channel measurements in a large auditorium, a large classroom, and a street canyon, all with comparable dimensions. No objects or people were present to disrupt any of the direct or secondary paths. Double-directional channel sounding using mechanically steered directional antennas is a notoriously slow process. The channel sounder that was employed to conduct these measurements uses various means to speed up the measurement process compared to an exhaustive search for all paths. The final results show that the quality and capacity of secondary (reflected) paths at mmWave frequencies is dramatically lower than the direct (LoS) path with results obtained in outdoor microcell environments to be significantly worse than in indoor environments of comparable size. Our results further suggest that the utility of switching to a secondary (reflected) path when the direct (LOS) beam is blocked is somewhat limited in outdoor, indoor and hallway environments.

The remainder of this chapter is organized as follows: Section 4.2 describes the underlying concepts; Section 4.3 describes the measurements procedure and equipment; Section 4.4 presents the results; and Section 4.5 presents the final conclusions.

4.2 Concept

Double-directional channel sounding using mechanically steered directional antennas is a notoriously slow process. Previous studies that have conducted similar measurements have done so in the form of exhaustive scans. The time-consuming nature of such measurements may be the reason why previous standards have chosen to not account for the quality of secondary paths.

In order to address this, a more efficient measurement process was developed in this study that is capable of conducting such measurements in only fraction of time it takes to do an exhaustive scan. In the case of an exhaustive scan, a complete 360 azimuth scan needs to be conducted at both the transmitter and the receiver. Channel responses are collected after every few degrees during the scan. The measurement scan proposed in this work cuts down on the measurement time by conducting continuous scans in the zero-span mode of the VNA (refer to Section 4.3.3 for more details). This is much quicker than having to stop every few degrees to collect the channel response, as in the case with an exhaustive search.

In order to conduct these efficient measurements, a suitable test fixture was developed that automated the entire measurement process. The channel sounder configuration further improved the efficiency of the overall measurements. The channel sounder was configured such that the responses for both the vertical and horizontal polarizations can be captured at the same time.

Measurement sites were selected such that measurements are conducted in comparable environments. The sites were grouped into three categories: Indoor, Outdoor, and Hallway. In each category, the sites were selected with similar dimensions. The transmit and receive antennas were also positioned strategically in the sense that it was ensured that majority of antenna pointing angles and a variety of transmitter-receiver positions were being utilized. A lot of care also went into making sure that the transmit and receive antennas were perfectly aligned and this was done with the use of laser pointers, bubble levels, etc.

4.3 Methodology

4.3.1 Environment

The measurements were conducted in large indoor, outdoor and hallway environments. A total of 55 transmitter-receiver configurations were measured, which included 21 indoor, 23 outdoor, and 11 hallway configurations. Figure 37 shows some sample locations for each of the three environments. All measurements were conducted on the UBC campus. Outdoor locations included 3-4 story buildings along with some foliage. Indoor locations included large conference rooms, atrium and hallways. The transmitter-receiver coordinates were chosen such that the antenna separation distances corresponding to all locations are Gaussian distributed. Figure 38 shows the transmitter-receiver coordinates for all indoor locations. The orange circles represent the transmitter positions whereas the blue circles show the receiver positions (Figure 38).

(a) (b) (c)

Figure 37 - Measurement Environment: (a) Indoor, (b) Hallway, and (c) Outdoor

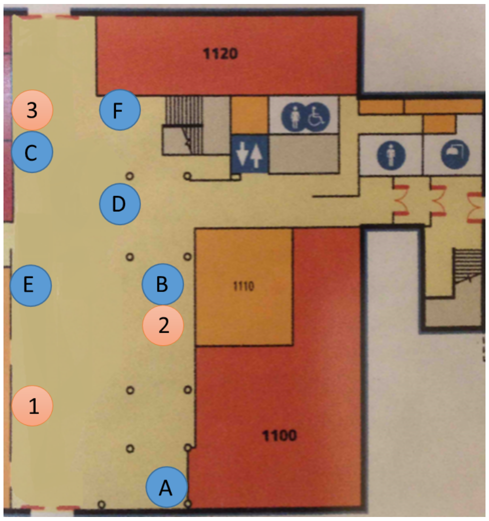

(a)

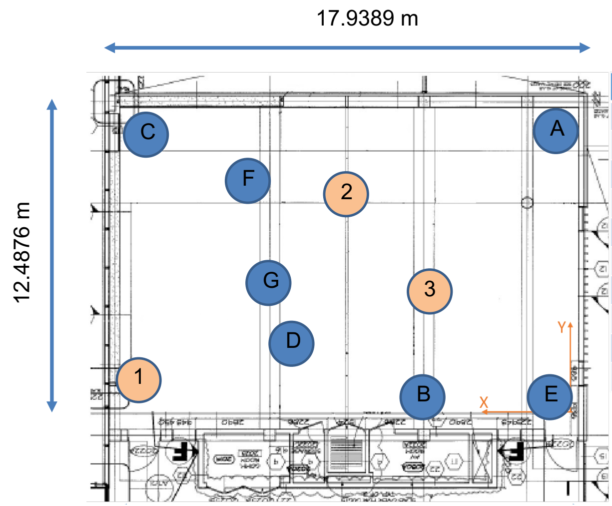

(b)

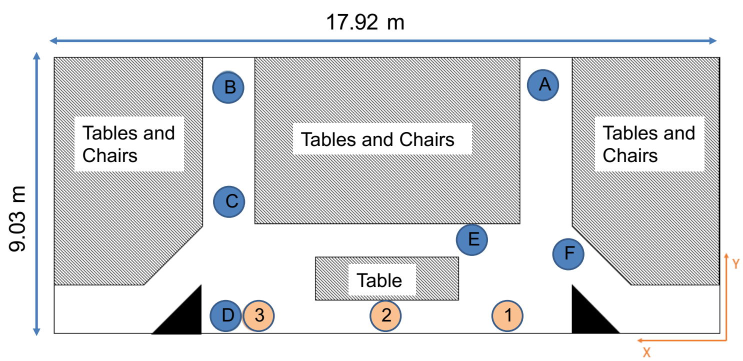

(c)

Figure 38 - TX-RX Configurations for Indoor Locations: (a) Atrium, (b) Conference Room, (c) Classroom

4.3.2 Channel Sounder Configuration

A VNA-based channel sounder was utilized for the measurement campaign. The 28 GHz channel sounder has an operating bandwidth of 1 GHz and provides 1 ns delay resolution. The maximum measurable path loss is 165 dB and the dynamic range is 45 dB. The instrument is VNA-based with a nominal channel sweep time of 500 ms. In zero-span mode, the sampling time is 1 ms. The transmitting antenna is an 18 dBi horn with 20º beamwidth in both planes. The receiving antenna is a dual-polarized 23 dBi horn with 13º beamwidth in both planes. Both antennas are mounted on identical azimuth-elevation positioners. The scan FOV is 360º in azimuth and +30º to -45º in elevation. The system can resolve both AoD and AoA.

The channel sounder configuration is shown in Figure 39. The power is transferred to transmit side using a set of Miteq RF to Fibre Transceiver units (100 MHz to 11 GHz band width). The length of the fibre cable (10 m or 100 m) was chosen based on the measurement setup. For Ka band measurements, a set of up convertor and down convertor is used to increase the IF frequency (750 – 1750 MHz) to millimetre wave range (29.3-30.3 GHz) and then bring it back to the IF range using an LO of 28.55 GHz. The power from port one of the VNA is transferred to the block up convertor using the second set of Miteq RF to fibre transceiver unit (10 MHz to 6 GHz band width). To have synchronization between BUC and Receiver, the attenuated 10 MHz reference signal generated by VNA is injected to the fibre link (using bias tee) and delivered to transmit side. After amplification, the 10 MHz signal is then re-injected to BUC along with 24 VDC power using bias tee.

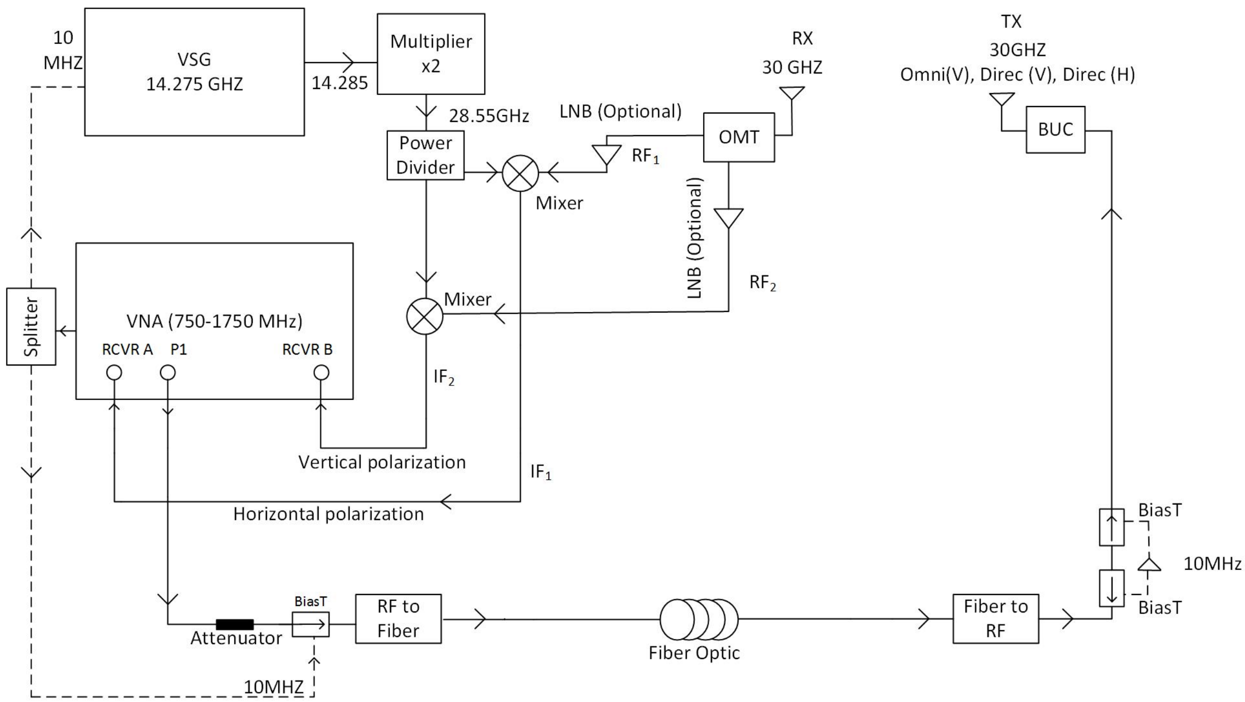

Figure 39 - Channel Sounder Configuration for Beam Quality Measurements

4.3.3 Measurement Procedure

In order to identify and characterize the best five paths for a given transmitter-receiver configuration, the measurements are carried out in three separate stages. The first two stages utilize the zero-span mode in the VNA in order to identify the Direction of departure (DOD) and Direction of arrival (DOA) for each of the best four paths. In the zero-span mode the local oscillator remains fixed at a given frequency and the analyzer turns into a fixed-tuned receiver. In this mode the signal's power variations are shown as a function of time. In stage 3, a full frequency response is collected for each of the DOD/DOA pair (obtained from stages 1 and 2) in order to characterize each beam.

The goal of stage 1 measurements is to identify all possible paths in the channel and their corresponding DOAs. This is done by using an omni-directional antenna at the transmit side and a directional antenna at the receiver. A full 360° azimuth scan is then conducted with the directional antenna at the receiver. The resulting waveform is shown in Figure 40. The measurements are recorded using the zero span mode in the VNA. Each of the measured scans had a resolution of 14150 points which is equivalent to 0.0248°. The zero span measurement scans were conducted at five different frequencies: 0.75, 1, 1.25, 1.5, and 1.75 GHz. A linear average of responses resulting from each of the five scans is then computed.

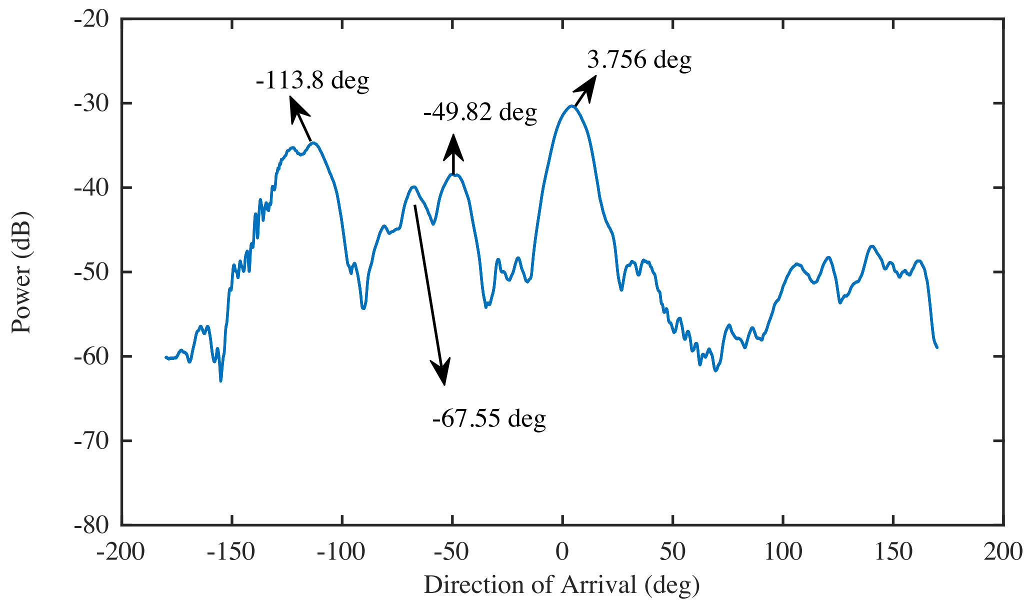

Figure 40 - Stage 1 Zero Span Measurements, Identify DOA's for Best Four Paths

Stage 2 measurements are then conducted in order to identify the DOD's corresponding to the best four paths. Directional antennas are now used both at the transmit and receive side. Antenna at the receiver is then pointed at the DOA angle obtained from stage 1 and full 360 azimuth scans are conducted at the transmitter. The scans are again conducted using the zero span mode with 0.0248 angular resolution (Figure 42). Similar to stage 1, zero-span scans are conducted at the 5 different carrier frequencies mentioned earlier and a linear average of all five responses is then computed. At the end of this stage, the DOD/DOA pairs corresponding to the best four paths have been computed.

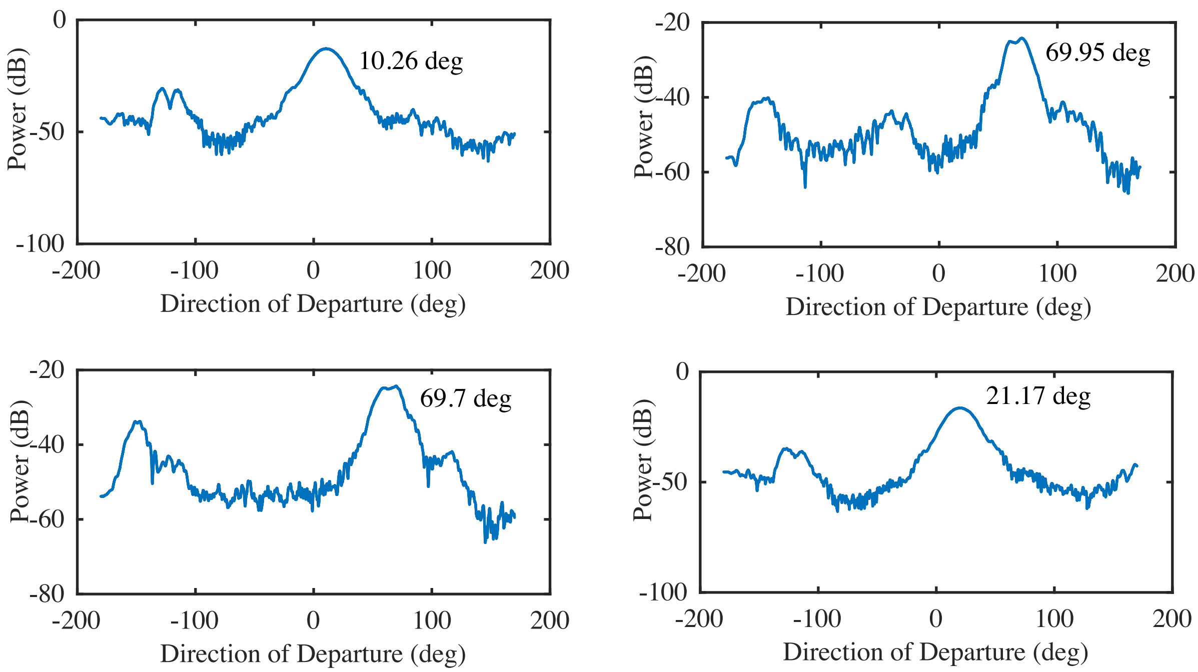

Figure 41 - Stage 2 Zero Span Measurements, Identify DOD's for Best Four Paths

Stage 3 of the measurements is where the complete frequency responses are collected for the best four paths. This is done by pointing the transmitter and the receiver in the directions obtained from stages 1 1and 2 (DOD/DOA pair). The channel sounder is configured to receive vertical and horizontal polarizations simultaneously. However, at the transmit end, measurements are first conducted with vertical polarization and then repeated with horizontal polarization. In the end co – and – cross polar frequency responses (VV, VH, HV, and HH) for the best four paths are obtained. Measured responses for the V-V configuration are shown in Figure 42.

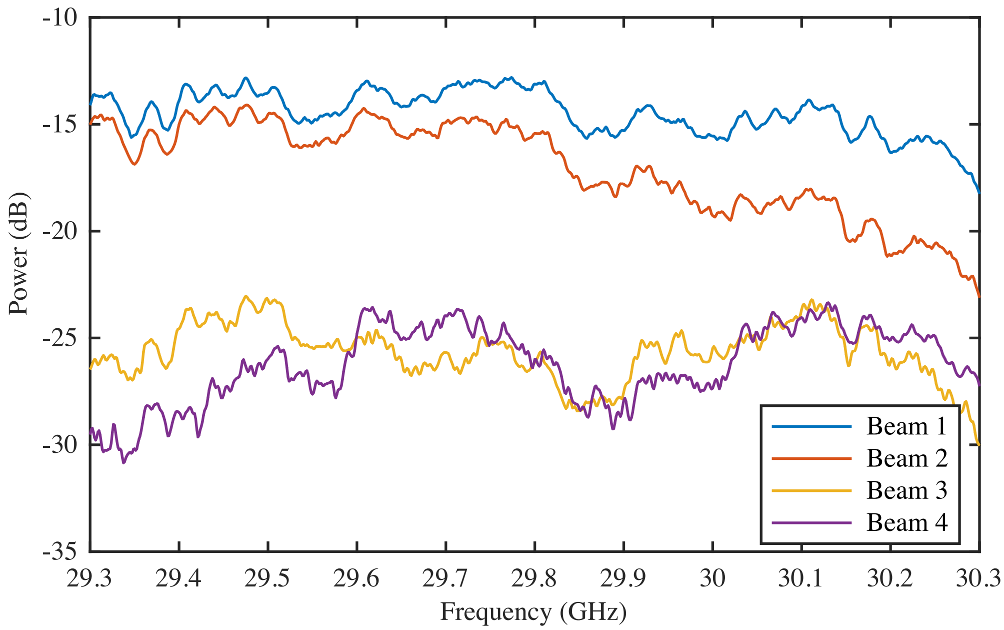

Figure 42 - Stage 3 Frequency Responses for Best Four Paths

4.3.4 Back-to-back Calibration

Back-to-back (B2B) calibration is necessary in order to correct for any system errors and accurately characterize channel parameters. It is crucial to have prior knowledge of the non-idealities in the measurement system and then apply proper corrections in the measured channel response to account for the system errors. In a VNA- based channel sounder non-idealities can arise from spurs or other distortions. The system response can be obtained by performing back-to-back calibration. This is done by first removing the transmit and receiving antennas and then connecting the front-ends using a phase stable coax cable and two 30-dB attenuators. The attenuators were used to ensure that there is no damage to the RF components. This setup can be seen in Figure 43. The frequency response of this B2B setup is recorded.

Figure 43 - Back-to-back Calibration Measurement Setup

The overall system response can be obtained as follows,

$$H_{system}(f) = \frac{H_{B2B}(f) * G_{TX} * G_{RX}}{H_{Caable}(f) * H_{attenuator1}(f) * H_{attenuator2}\ (f)} \tag{12}$$

where back-to-back, TX, RX, cable, and attenuator transfer functions are used. The measured channel response is then divided by the overall system response in order to correct for any system artifacts or non-idealities. The measured system response also provides a good measure of the linearity and the dynamic range of the channel sounder.

4.3.5 Measurement Verification

In order to verify the accuracy of the channel sounder measurements, we utilized a map-based multipath verification approach. This method assumes an open LOS channel such that there exists a LOS path and some specular reflections. Therefore, the verification measurements were conducted on a rooftop with very few scatterers. The geometric representation of the measurement setup is provided in Figure 44.

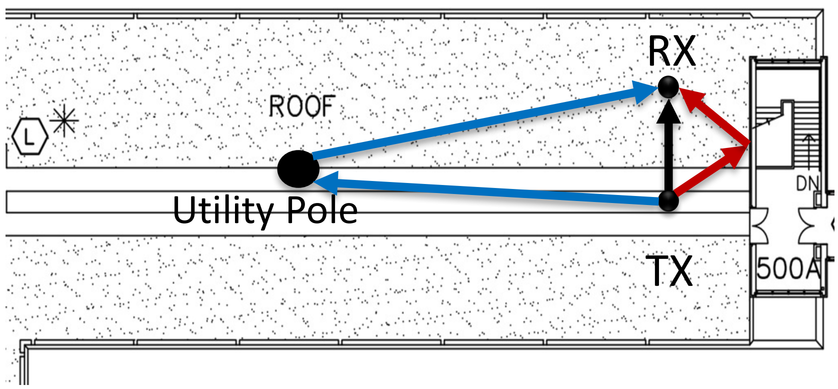

Figure 44 - Map-based Multipath Verification

The delays corresponding to each of the paths shown in Figure 44 are then extracted from the measured PDP (Figure 45). The path lengths for each measured MPC is calculated based on the expression given below,

$$Path\ length = Delay * c \tag{13}$$

where c is the speed of light. The geometric or map-based path lengths were recorded using a laser at the measurement site. A comparison of experimental and theoretical path lengths is shown in Table 3 and they match quite well.

Table 3 - Comparison of Map Based and Measured Path Lengths

MPC	DOD	DOA	Path Length (m) – Map based	Path Length (m) - Measured
→	0°	0°	5.95	6
→	60°	-60°	11.90	12
→	-90°	80°	39.5	38.7

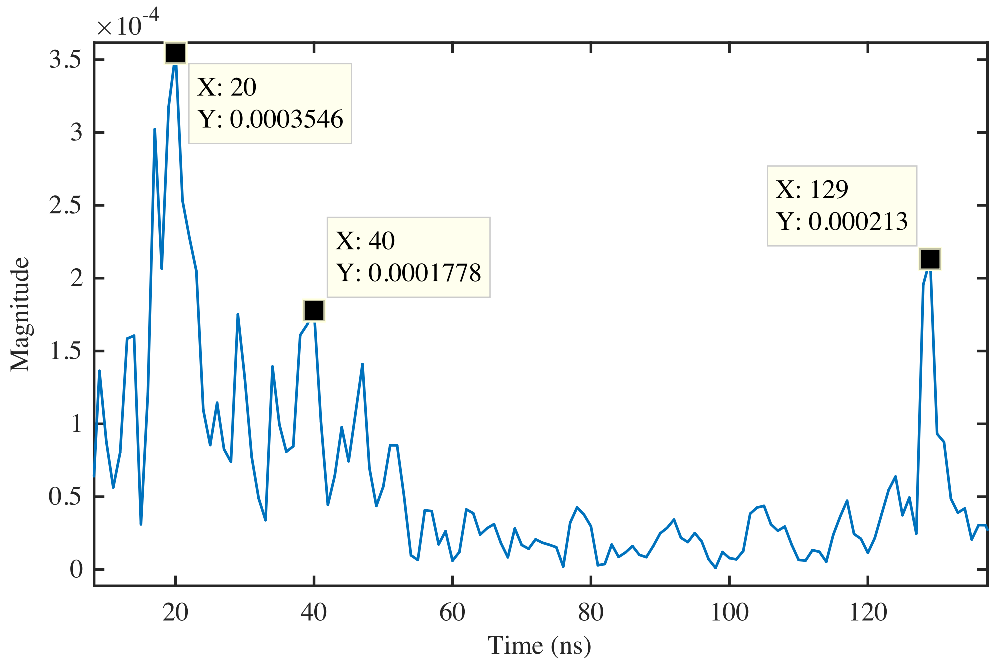

Figure 45 - Measured PDP Response for Rooftop Map based Verification

An exhaustive search for the direct and secondary beam was also conducted for comparison with the more efficient measurement scheme shown in this work. The antennas were mechanically steered, and a response was recorded at every 5° interval. As shown in the colormap below, maximum power is recorded when the transmit and receive antennas are aligned (Figure 46).

Several other blobs of 'yellow' can be seen in the colormap and these are the secondary paths arising from the specular reflections.

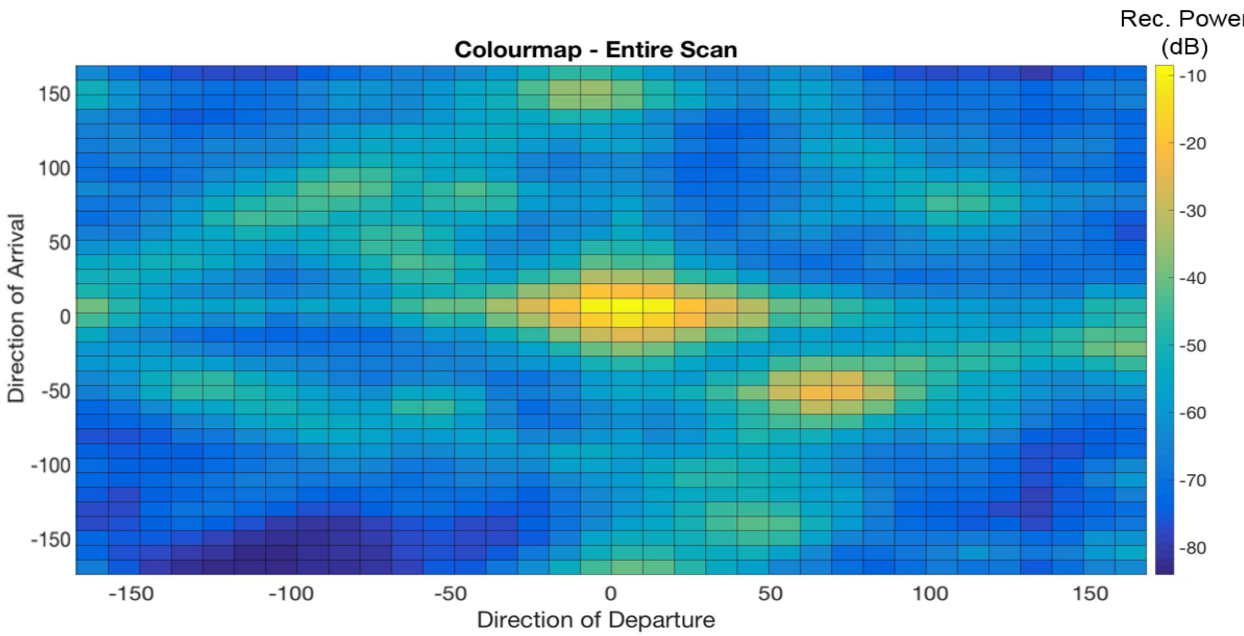

Figure 46 - Exhaustive Scan Conducted on the Rooftop

4.4 Results

The full 801-point frequency responses corresponding to each beam (shown in Section 4.3.3) are used in this section to compute path loss, K-factor, and capacity. Parameters for a measurement-based model are presented in this section which can be used by ray-tracing based simulation tools in order to get a better understanding of the channel.

4.4.1 Path Loss Analysis

Path loss values between the transmitter-receiver links were computed by dividing the measured frequency response by the back-to-back calibration frequency response (refer to Section 4.3.4). For each beam, five different frequency responses of the channel were captured. Finally, path loss values were computed by taking the linear average of all 5 frequency responses followed by an average of all 801-points in the frequency response.

Path loss comparison between the direct and secondary paths in indoor and outdoor environments is shown in Figure 47 and Figure 48, where path loss (in dB) is plotted again distance on a log scale. As expected, the path loss exponent increases from beam 1 to beam 4. Beam 1 is also compared with the path loss given by the Friis formula and it matches quite well in both environments. There is, however, a 0.1 offset in measured to expected path loss exponent values, which may be due to combining of secondary MPCs corresponding to beam 1.

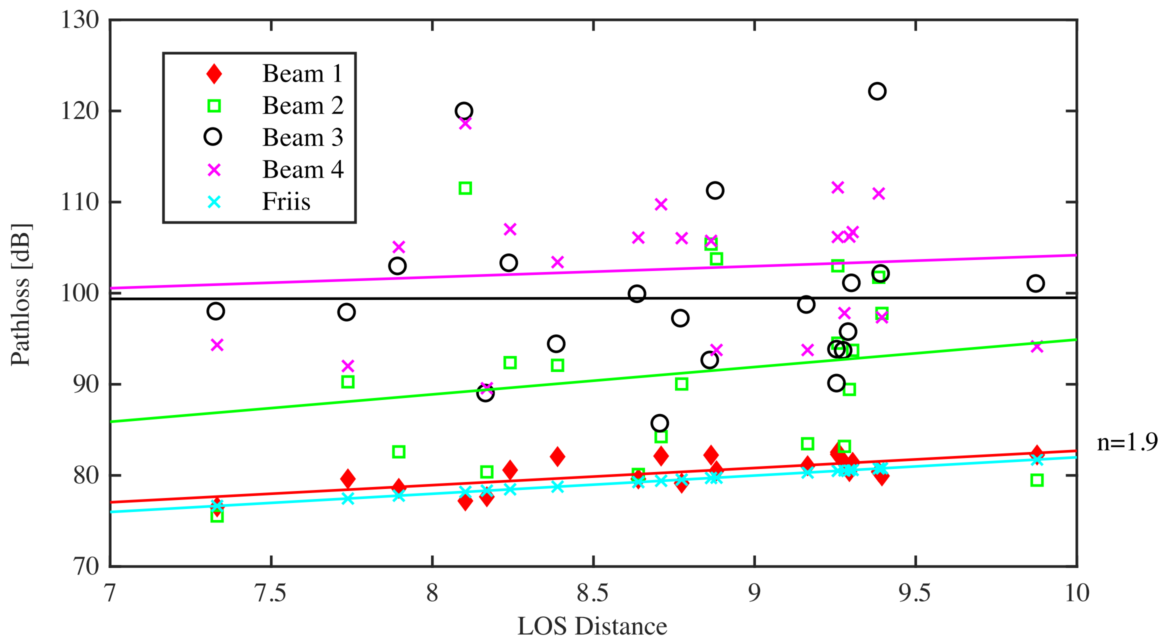

Figure 47 - Path Loss vs Distance for Best Four Paths: Indoor

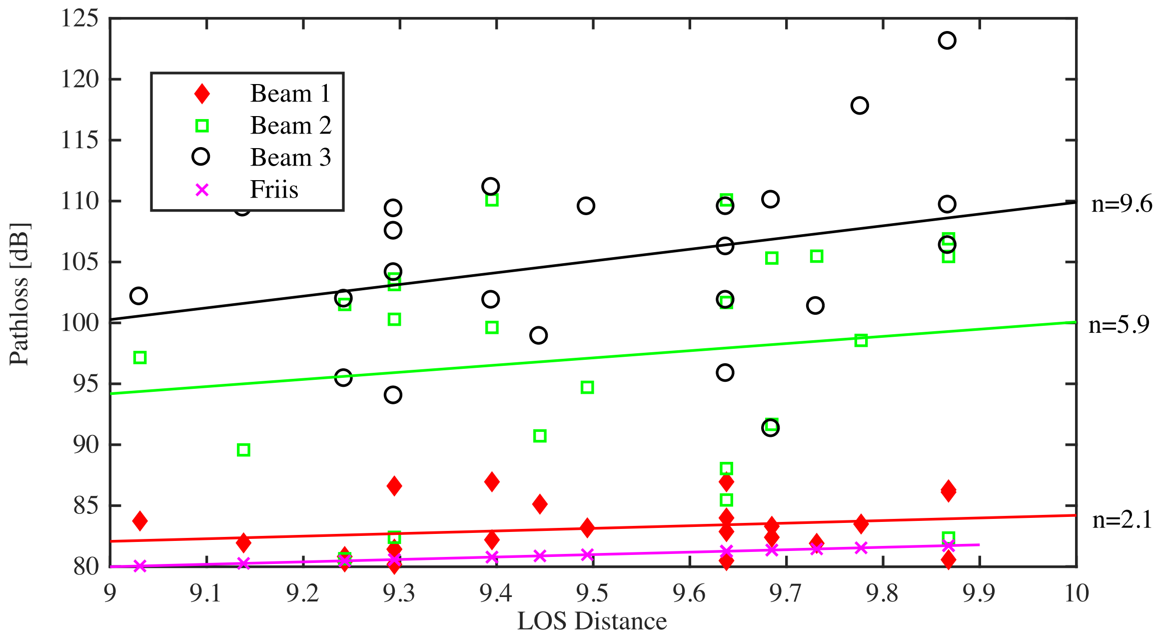

Figure 48 - Path Loss vs Distance for Best Three Paths: Outdoor

The histograms shown in Figure 49 are derived by normalizing the path loss values for the secondary paths with respect to the direct beam. The results show that path loss values increase significantly for secondary paths as compared to the direct beam. A Log-Normal distribution is observed for all paths in both environments.

Coherent beam combining is analyzed for the best four paths measured in each channel. In order to coherently combine paths, the square root of the absolute (i.e. linear) received power levels in Watts were computed, and the voltages obtained at the strongest few 3D (three dimensional) angular segments were summed, thus the total coherent voltage was found at each receiver location, and then this value was squared to obtain received power in units of Watts, which was then converted into dBm. Figure 50 shows the cdf plots for beam combining in indoor (top) and outdoor (bottom) environments. Improvement in path loss is shown in comparison to the strongest beam. The results demonstrate that beam combining provides more improvement in path loss in indoor environments as compared to outdoor. However, our results show relatively smaller improvement in path loss than those presented in [59].

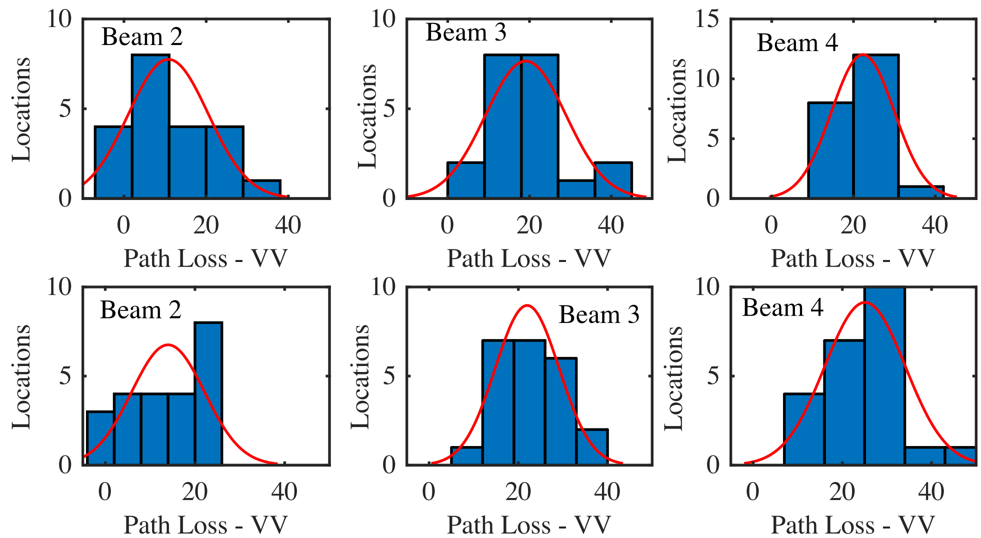

Figure 49 - Path Loss VV (Normalized to Beam 1): Indoor (Top Row); Outdoor (Bottom Row)

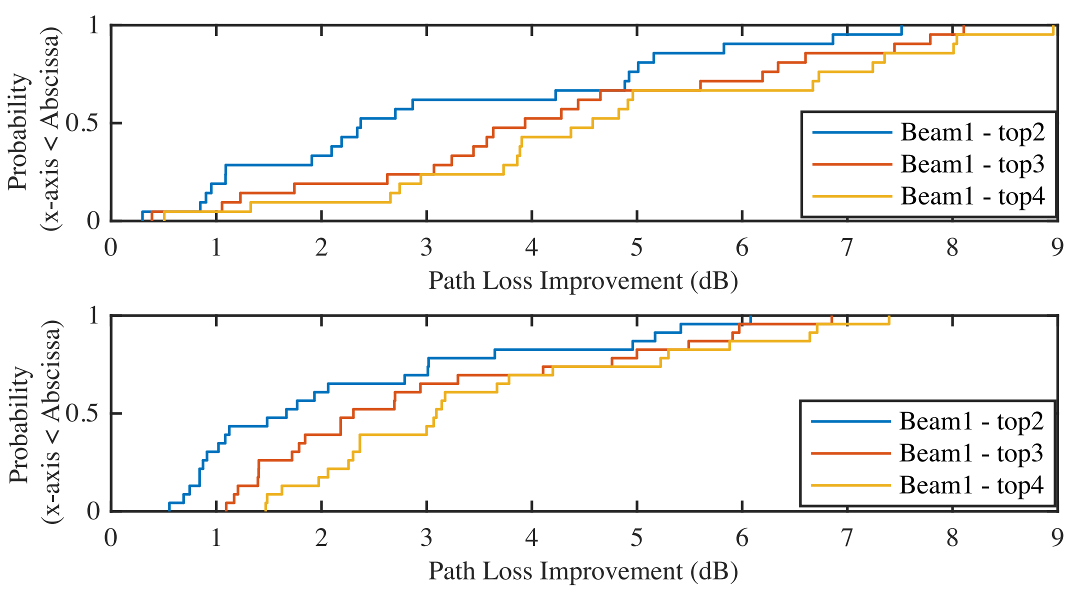

Figure 50 - Coherent Beam Combining (Path Loss Improvement): Indoor (Top); Outdoor (Bottom)

4.4.2 K-factor Analysis

Another performance metric used to assess the quality of the measured paths is K-factor. The complex path gain at any frequency consists of a fixed component plus a zero-mean fluctuating component. If the fluctuation is complex Gaussian, the time-varying envelope of the composite gain will have a Ricean distribution. The defining parameter of this distribution is the K-factor, which is the power ratio of the fixed and fluctuating components. The simple and rapid method for computing K-factor is described in [58] wherein K-factor is an exact function of moments estimated from the time series data. The complex path gain of a narrowband channel can be described using the following equation,

$$g(t) = V + v(t) \tag{14}$$

where V is a complex constant and v(t) is a complex, zero-mean random time variation caused by vehicular motion, or moving scatterers (e.g., foliage, people, etc.).

Measured power versus time data is used to compute the first two moments of the power gain, G which is given by $|g(t)|^2$. Equations (15) and (16) below describe the first and second moments of the response given in (14). The left hand sides of both equations below,

$$G_a = |V|^2 + \sigma^2 \tag{15}$$

$$G_v = [\sigma^4 + 2|V|^2\sigma^2]^{\frac{1}{2}} \tag{16}$$

are estimated from the measured data. The values for $|V|^2$ and σ^2 can then be computed and substituted into (17) below in order to compute K-factor,

$$K = |V|^2/\sigma^2 \tag{17}$$

K-factor box plots for the top four paths in indoor and outdoor environments are shown in Figure 51. An exponential decrease in K-factor is observed from path 1 to beam 4 in both environments (Figure 51). These results clearly show that the frequency flatness of the measured response deteriorates significantly for secondary paths as compared to the direct beam.

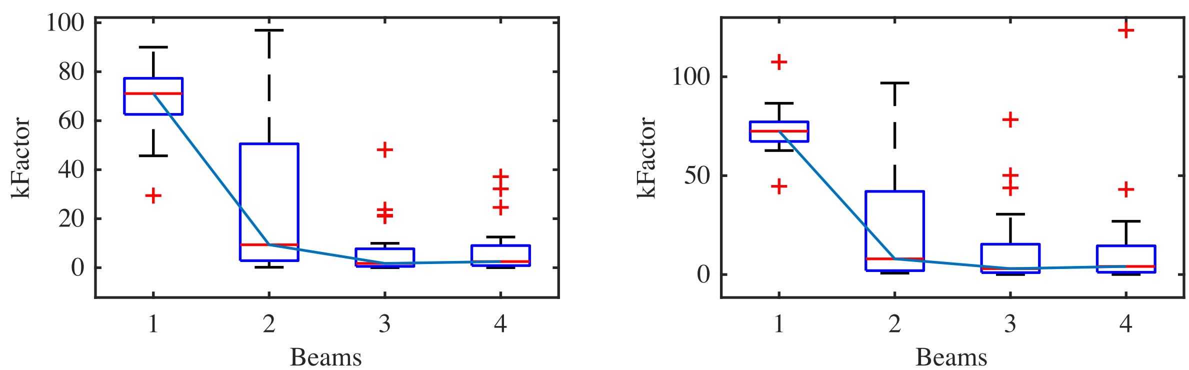

Figure 51 - K-factor Box Plots: Indoor (Left); Outdoor (Right)

Path loss and K-factor correlation figures corresponding to outdoor and indoor environments are shown below (Figure 52 - Figure 53). In general, an inverse relationship between K-factor and path loss was observed for secondary paths. Beams with relatively low path loss resulted in a very flat frequency response and hence the high K-factor values were observed for these particular paths. Correlation figures below show that there is very little variation in path loss and K-factor for the direct paths. This is consistent with the distance distribution corresponding to all transmitter-receiver configurations.

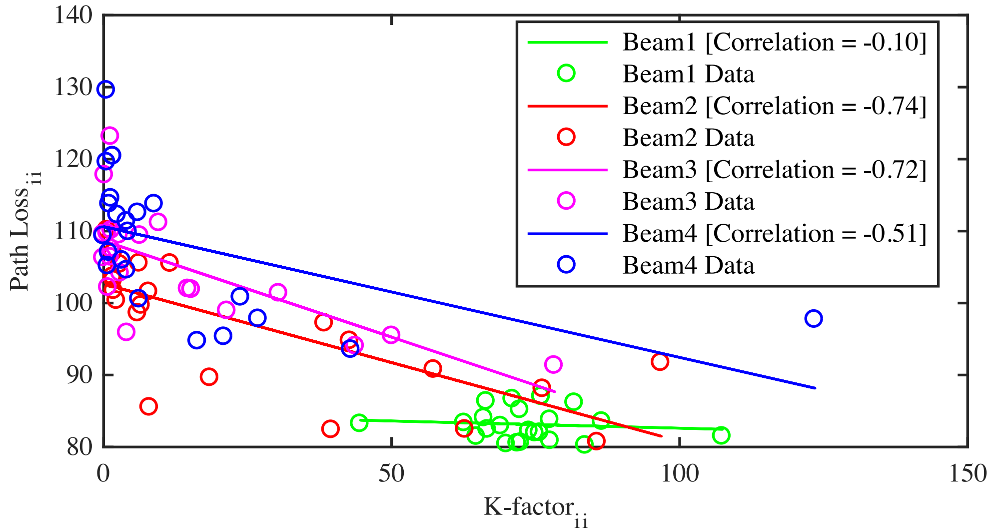

Figure 52 - Correlation Between Path Loss and K-factor for Best Four Paths: Outdoor

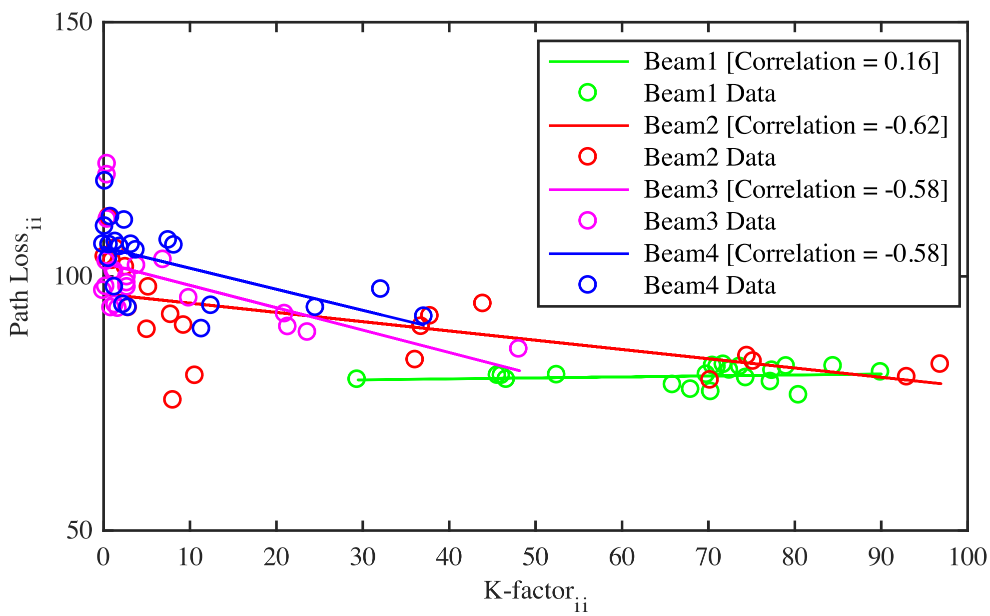

Figure 53 - Correlation Between Path Loss and K-factor for Best Four Paths: Indoor

Figure 54 shows K-factor histograms corresponding to secondary paths in outdoor and indoor environments. All histograms were normalized with respect to path 1 in order to make results more meaningful. An exponential decrease in K-factor is observed for all normalized paths.

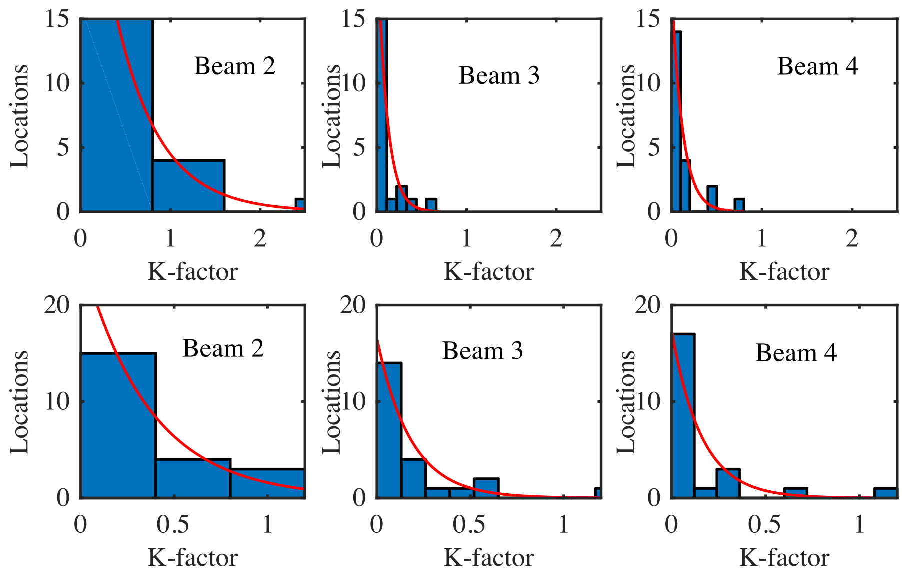

Figure 54 - K-factor (Normalized to Path 1): Indoor (Top); Outdoor (Bottom)

4.4.3 MIMO Capacity Analysis

In order to qualitatively assess the performance of direct and secondary paths, MIMO capacity was used as a performance metric. The assumption for flat fading holds for MIMO in the sense that the bandwidth of transmission needs to be within the coherence bandwidth of the channel and the frequency response is considered a single-valued complex scalar [85]. The 2x2 MIMO presented in this work can be represented by the following transmission matrix,

$$H = \begin{bmatrix} h_{11} & h_{12} \\ h_{21} & h_{22} \end{bmatrix} \tag{18}$$

where h_{ij} represents the channel coefficient between receiver and transmitter. The MIMO capacity in bits/s/Hz can then be provided using the following formula,

$$C = \log_2 \det\left(I_m + \frac{\rho}{n} * H * H^H\right) \quad \frac{\frac{\text{bits}}{\text{s}}}{\text{Hz}} \tag{19}$$

where $\{.\}^H$ stands for the transpose of the complex conjugate (Hermitian transpose) and I_m is the 2x2 unity matrix.

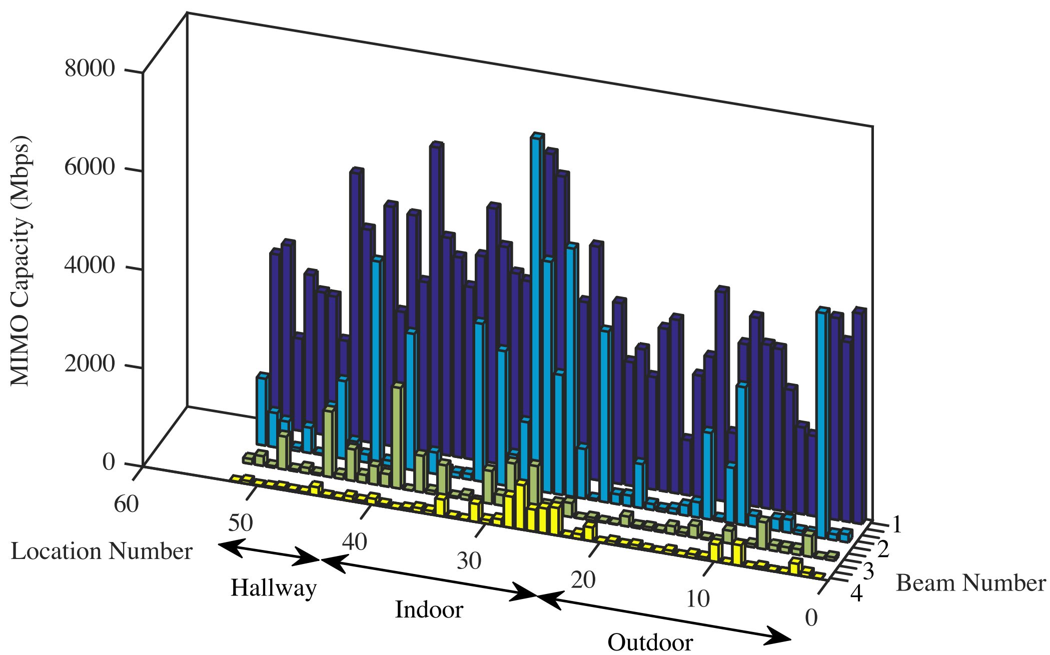

Figure 55 - MIMO Capacity, Best Four Beams (Indoor, Outdoor, and Hallway)

MIMO capacity corresponding to the top four paths in all three environments is shown in Figure 55. The secondary paths are relatively stronger in indoor and hallway environments as opposed to outdoor. This is because outdoor measurement scenarios comprised of 3-4 story high buildings with reflective exterior surfaces (ex. glass) in most cases. Secondary paths in such situations would have a much higher path loss as opposed to indoor environments (ex. conference rooms) with much smaller volume and minimal reflective surfaces.

Figure 56 shows MIMO capacity for paths 2, 3, and 4 normalized with respect to path 1. Beam 1, which is the LOS path is completely deterministic. Figure 12 shows the relationships between the direct and secondary paths. The exponential distribution observed in MIMO Capacity is due to the exponentially distributed path lengths of the secondary paths.

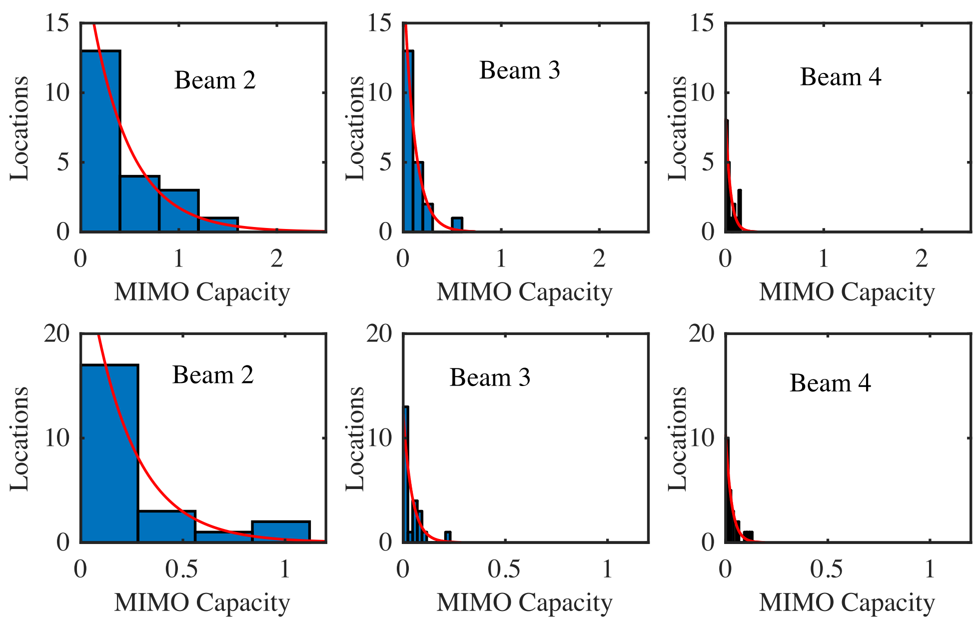

Figure 56 - MIMO Capacity (Normalized to Beam 1): Indoor (Top Row); Outdoor (Bottom Row)

As opposed to the MIMO capacity (shown above) which considers the responses from all four polarization combinations, the SISO capacity only considers the V-V polarization combination. In Figure 57, the capacity computed just for the V-V channel is shown for each of the secondary paths. In order to make these results more meaningful, the capacity values for the secondary paths are normalized with respect to path 1. Just like the MIMO case, exponential distributions are observed for all cases.

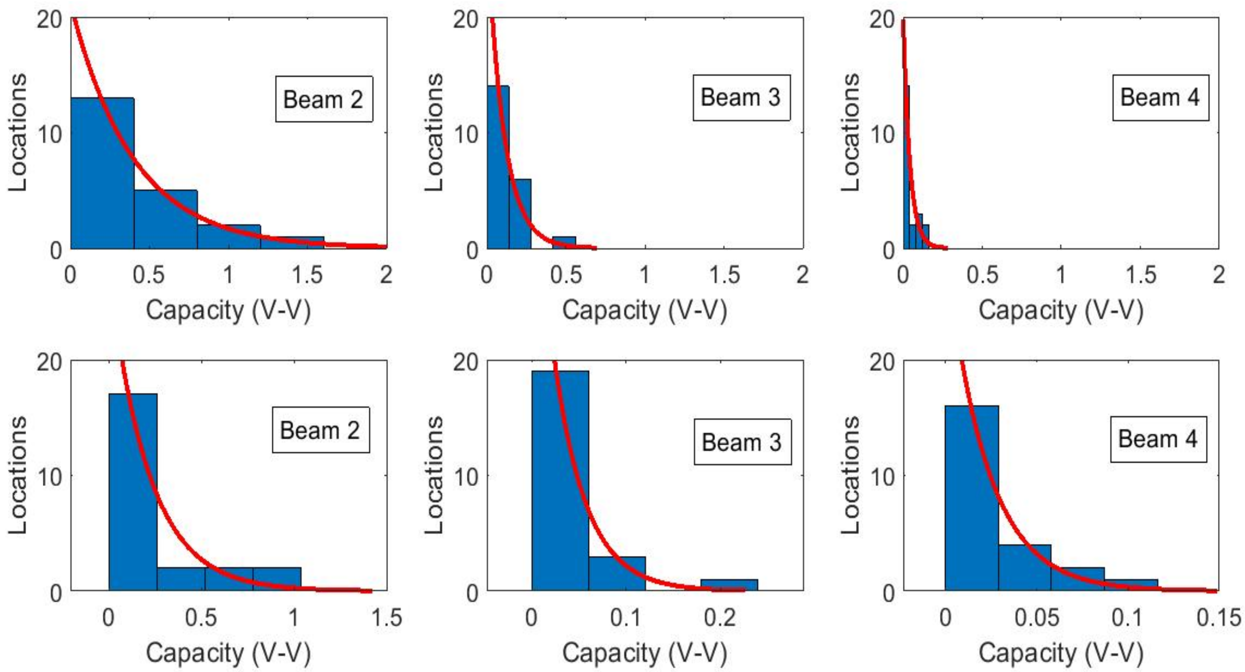

Figure 57 - Capacity V-V (Normalized to Beam 1): Indoor (Top Row); Outdoor (Bottom Row)

4.4.4 Simulation Model Parameters

First order statistics (mean or decay rate) for K-factor, path loss, and MIMO capacity are provided in Table 4. These parameters are derived from distributions shown in Figure 49, Figure 54, and Figure 56. All of the parameters presented in Table 4 for secondary beams have been normalized with respect to the direct (LoS) beam in order to make the results more meaningful. In the case of indoor MIMO capacity, the second-best beam is only 40.3% of the LoS beam; beam 3 is only 11.1% of the LoS beam; and beam 4 is only 4.89% of the LoS beam (Table 4). Similarly, K-factor also deteriorates significantly from beam 1 to beam 4 (Table 4). The rate parameter (λ) for MIMO capacity increases from beam 2 to beam 4 due to the decrease in variability.

Table 4 - K-factor, Path Loss, and MIMO Capacity: Mean Values and Rate Parameter

Parameter	Parameter Definition	Indoor	Outdoor
K-factor (linear scale) [Exponential Distribution]	μ and λ are mean values and rate parameters of K-factor for beams 2, 3, and 4 which are normalized wrt. beam 1	$\mu_2 = 0.49$ $\lambda_2 = 2.02$	$\mu_2 = 0.36$ $\lambda_2 = 2.77$
		$\mu_3 = 0.11$ $\lambda_3 = 9.32$	$\mu_3 = 0.18$ $\lambda_3 = 5.52$
		$\mu_4 = 0.12$ $\lambda_4 = 8.20$	$\mu_4 = 0.16$ $\lambda_4 = 6.25$
Path Loss (dB) [Log-Normal Distribution]	μ and λ are mean values and rate parameters of Path Loss (VV) for beams 2, 3, and 4 which are normalized wrt. beam 1	$\mu_2 = 10.81$	$\mu_2 = 14.01$
		$\mu_3 = 19.08$	$\mu_3 = 21.98$
		$\mu_4 = 22.31$	$\mu_4 = 25.01$
Capacity MIMO (Mbps) [Exponential Distribution]	μ and λ are mean values and rate parameters of MIMO Capacity for beams 2, 3, and 4 which are normalized wrt. beam 1	$\mu_2 = 0.40$ $\lambda_2 = 2.48$	$\mu_2 = 0.22$ $\lambda_2 = 4.62$
		$\mu_3 = 0.11$ $\lambda_3 = 8.97$	$\mu_3 = 0.04$ $\lambda_3 = 23.30$
		$\mu_4 = 0.049$ $\lambda_4 = 20.46$	$\mu_4 = 0.03$ $\lambda_4 = 34.66$

Exponential distributions were observed for both MIMO capacity and K-factor in all environments. We realized that this is due to the exponentially distributed path lengths of the best four beams.

Since the distributions observed for K-factor and MIMO capacity are exponential, a correlation or simulation model for this case is very complicated because the random variables involved are non-Gaussian. A copula model has been used in the past to model correlated random variables that aren't Gaussian. This approach is extremely complex but can be used in future to model K-factor and MIMO capacity.

Table 5 compares the normalized secondary beams in indoor and outdoor scenarios. It can be concluded that outdoor MIMO capacity is approximately twice as worst compared to the indoor capacity. Although both indoor and outdoor measurement scenarios were of comparable size, this drop off in outdoor capacity may be due to the rough exterior surfaces of buildings and foliage. Approximately 3 dB increase in path loss was observed in outdoor scenarios as compared to indoor.

Table 5 - Tertiary Analysis (Comparing Indoor and Outdoor)

	Beam 2 (Normalized wrt. Beam 1)	**Beam 3** (Normalized wrt. Beam 1)	**Beam 4** (Normalized wrt. Beam 1)
Path Loss (dB) (Outdoor - Indoor)	3.19	2.89	2.70
Capacity MIMO (Indoor/Outdoor)	1.86	2.60	1.69

Lastly, the performance metrics for secondary beams are compared in Table 6. Clear deterioration of all performance metrics from beam 2 to beam 4 can be observed in Table 6. Provided that path 1 is completely deterministic, statistics given in Table 4 - Table 6 can be used to provide further insight into the performance of secondary paths in indoor and outdoor environments.

Table 6 - Tertiary Analysis (Comparing the Secondary Beams)

	Beam3 wrt. Beam2	**Beam4 wrt. Beam2**	**Beam4 wrt. Beam3**
K-factor (Indoor)	49.4%	10.7%	12.2%
K-factor (Outdoor)	36.1%	18.1%	16.0%
Path Loss (VV) (Indoor)	8.27 dB	11.50 dB	3.23 dB
Path Loss (VV) (Outdoor)	7.97 dB	11.00 dB	3.03 dB
Capacity MIMO (Indoor)	27.7%	12.1%	43.8%
Capacity MIMO (Outdoor)	19.8%	13.3%	67.2%

4.5 Discussion

Path loss and distortion at millimetre-wave frequencies have been studied previously in a variety of indoor and outdoor environments but, surprisingly, the relative capacity of direct and secondary paths hasn't been previously captured. There is a pressing need to understand the quality of such paths in order to accurately predict the performance of systems. Double-directional channel sounding using mechanically steered directional antennas is a notoriously slow process. To address this problem, we assembled a suitable test fixture and conducted channel measurements in comparable indoor and outdoor environments. The channel sounder utilized for this work uses various means to speed up the measurement process compared to an exhaustive search for all paths. It still takes almost an hour to assess the performance of alternative paths between two points with the three-dimensional (D2I) case taking 50% longer than the two-dimensional (D2D) case.

We have presented our observations of the path loss, Ricean K-factor, and SISO/MIMO channel capacity associated with the top four strongest paths as distributions/box plots. In the case of path loss and channel capacity, we normalized the values of the secondary paths with respect to the value observed for the direct path in order to make comparisons between links more meaningful.

Our results show that the relative path loss on the n strongest secondary paths follow a Log-normal distribution while the Ricean-K-factor and SISO/MIMO channel capacity follow exponential distributions. They clearly show that the quality and capacity of secondary (reflected) paths at mmWave frequencies is dramatically lower than the direct (LoS) path with results obtained in outdoor microcell environments to be significantly worse than in indoor environments of comparable size. They further suggest that the utility of switching to a secondary (reflected) path when the direct (LoS) path is blocked is somewhat limited in outdoor, indoor and hallway environments.

The second strongest beams in indoor environments are found to be on average 40.3% of the LoS beam; beam 3 are only 11.1% of the LoS beam; and beam 4 are only 4.89% of the LoS beam. Outdoor MIMO capacity is found to be approximately twice as worst as compared to the indoor capacity. This is likely due to rough exterior surfaces of outdoor buildings as compared to the much smoother surface of interior walls. Path loss observed in outdoor scenarios is 3 dB higher than in indoor environments. Exponential distributions were observed for both MIMO capacity and K-factor in all environments. Since the distributions observed for K-factor and MIMO capacity are exponential, a correlation or simulation model for this case is very complicated because the random variables involved are non-Gaussian. However, accurate estimation of the Channel Capacity provided in this work can be directly used by existing simulation tools as it captures all of the relevant channel parameters.

The work presented here establishes the feasibility of such measurements and demonstrates an efficient methodology to conduct them. To assess the quality of direct and secondary paths, we didn't just analyze path loss and K-factor but also provided an estimate of capacity for each beam. In the near future, a statistical site-general model can be developed based on the results shown here; where the LoS path is completely deterministic, and the secondary paths can be estimated based on the derived parameters in this work. Although this work shows that the quality of secondary paths is dramatically lower than the direct path, we believe that clever algorithms (beam training/beam tracking) may be implemented in the future to mitigate these impairments.

Chapter 5: Conclusions and Future Work

5.1 Conclusions

Millimetre-wave signals are highly susceptible to blockage by humans and building structures. Developers require accurate models of these phenomena in order to support design and simulation of alternative strategies to mitigate such blockage. Here, we have sought : 1) to develop a physical-statistical model of the effect of human presence/blockage at 60 GHz; 2) to statistically characterize the manner in which through-wall attenuation varies between wall types, different walls of the same type, and different locations on a given wall together with an indication of how these results scale between 10 and 30 GHz; and 3) to provide an accurate assessment of the relative quality and capacity of direct and secondary paths at 30 GHz in both indoor and outdoor environments.

Simple but accurate models of the effect of human presence on path propagation are vital to the simulation of mmWave access networks. Our physical-statistical model for human presence combines both geometrical and measurement-based elements and is both more accurate and more general than previous works. The presented model covers a wide range of geometries and can be used to accurately represent a large number of blockage scenarios. The geometric component of our model accounts for the relative phase of each component while the measurement-based component of our model captures the relative strength of each component. The overall model has two components: 1) the unshadow region of the blockage event is modeled using the two-ray model, and 2) the shadow region of the blockage event is modeled using the DKED model. High resolution measurements were conducted to differentiate between diffracted and reflected paths during the shadowing event.

The simulated results from our human-presence model match very closely with the measured blockage events. The reflection coefficient (Γ) is used to compute the strength of the reflected path within the unshadow region. It was realized that the reflection coefficient is distance dependent. The value of the reflection coefficient is observed to change every 0.1 m during the shadowing event. The resulting reflection coefficient values are consistent across multiple shadowing events with a very low standard deviation. The mean value for the reflection coefficient changed as follows across the 1.53 m long shadowing event: 5, 10, 20, 25, 10, and 6. The diffraction coefficient (γ) is used to compute the strength of the diffracted path within the shadow region. The derived value of the diffraction correction factor is observed to change as the transmitter-receiver separation distance changed. For 4 m, 6 m, and 8 m separation distances the value of the diffraction correction factor was 0.65, 0.7, and 0.8 respectively. For a given transmitter-receiver separation distance, the value of the diffraction correction factor is consistent for all blockage scenarios. Overall, the result is computationally efficient and will be a valuable tool for those engaged in the design and simulation of mmWave radio access networks which have the potential to be affected by human presence.

In this work, we were also able to reveal: 1) the distribution of through-wall attenuation, either point-to-point on a given wall or between walls of broadly similar type and 2) the extent to which the distributions for different wall types overlap or are separable or distinguishable. To accomplish this, we devised and assembled an automated test fixture that address most of the issues that make such a campaign challenging or time-consuming.

Our results demonstrate that through-wall attenuation does fall into separable classes and is amenable to statistical characterization. Mean values for through-wall attenuation observed at different walls are clearly divided into five quite separable categories based on building materials.

The observed mean values for each building materials at 30 GHz are as expected with brick walls showing the most attenuation (84 dB) followed by metal clad (58 dB), indoor walls (20 dB), wood (12.5 dB) and lastly glass (3 dB), which shows the least amount of attenuation. High standard deviation was observed in certain metal clad and indoor walls. Mean values for all building material were mostly consistent once the outliers (as previously discussed) are accounted for. The through-wall attenuation distributions for each wall were mostly Gaussian. We observed that through-wall attenuation at 10 GHz is significantly smaller than attenuation at 30 GHz in all materials. A high positive correlation is observed between 10- and 30-GHz through-wall attenuation values in all building materials with a best fit line slope of 1.45. The best fit line slope of 1.45 implies frequency dependence of the form of $f^{1.45}$ between 10 and 30 GHz through-wall attenuation (linear) values. As expected, much higher attenuation is observed in cross-polar scenarios as compared to the co-polar results. The difference between the co-polar and cross-polar results (cross-polarization factor) is observed to be quite high (15 – 30 dB) in materials like wood, glass, and drywall. This work will be of tremendous value to those who need to conduct system level studies or ray-tracing-based simulations of indoor and indoor-outdoor wireless communications systems.

When the direct path is blocked or not available, communication will be conducted by secondary paths that arise from reflection or scattering in the environment. There is a pressing need to understand the quality of such paths in order to accurately predict system level performance. However, double-directional channel sounding using mechanically steered directional antennas is a notoriously slow process. To address this problem, we assembled a suitable test fixture for channel sounding that uses various means to speed up the measurement process compared to an exhaustive search for all paths.

Our results show that the relative path loss on the four strongest secondary paths follow a log-normal distribution while the Ricean-K-factor and SISO/MIMO channel capacity follow exponential distributions. They clearly show that the quality and capacity of secondary (reflected) paths at mmWave frequencies is dramatically lower than the direct (LoS) path with results obtained in outdoor microcell environments observed to be significantly worse than in indoor environments of comparable size. They further suggest that the utility of switching to a secondary (reflected) path when the direct (LoS) path is blocked is somewhat limited in both indoor and outdoor environments. The second strongest beams in indoor environments are found to be on average 40.3% of the LoS beam; beam 3 are only 11.1% of the LoS beam; and beam 4 are only 4.89% of the LoS beam. Outdoor MIMO capacity is found to be approximately twice as worst as compared to the indoor capacity. Approximately 3dB increase in path loss was observed in outdoor scenarios as compared to indoor. The accurate estimation of the Channel Capacity provided in this work can be directly used by existing simulation tools as it captures all of the channel parameters.

5.2 Limitations and Future Work

The work presented here shows the feasibility of such models and measurements; and demonstrates trends and patterns that haven't been previously analyzed. However, more comprehensive measurement datasets may be required before these models can be adopted by standards development organizations such as 3GPP.

In the case of human presence, future measurement campaigns could be conducted at multiple frequencies and account for different polarizations. Lastly, additional data with human subjects of different body types may be collected in the future in order to obtain more comprehensive models.

In the case of through-wall attenuation, future work could include reflection and/or oblique incidence measurements. Frequency dependence of dielectric parameters can be further analyzed by conducting similar measurements at 60 GHz as it will allow us to more accurately discern the trend in frequency dependence.

In the case of secondary-path quality, our results for MIMO channel capacity can be directly used by existing simulation tools as it captures all of the relevant channel parameters. Future work could include similar measurements in other environment to confirm the observed trends.

References

[1] FCC, "Spectrum frontiers R&O and FNPRM: FCC16-89," 2016, [Online], Available: https://apps.fcc.gov/edocspublic/attachmatch/FCC-16-89A1 Rcd.pdf.

[2] IEEE Future Directions 5G Initiative, "IEEE future networks," *IEE Future Networks*, [Online]: https://5g.ieee.org/ (accessed Oct. 30, 2017).

[3] ITU-R. "Study Group 3 (SG3)." ITU.int. https://www.itu.int/en/ITU-R/study-groups/rsg3/Pages/default.aspx.

[4] M. Peter et al., "Deliverable D2.1: Measurement campaigns and initial channel models for preferred suitable frequency ranges," *mmMAGIC*, Apr. 2016. [Online]. Available: https://bscw.5g-mmmagic.eu/pub/bscw.cgi/d94832/mmMAGIC_D2-1.pdf.

[5] 3GPP, "Technical specification group radio access network; channel model for frequency spectrum above 6 GHz (Release 14)," 3GPP, Tech. Rep. TR 38.900 V14.2.0, Dec. 2016. [Online]. Available: http://www.3gpp.org/DynaReport/38900.htm

[6] B. Walke and R. Briechle, "A local cellular radio network for digital voice and data transmission at 60 GHz," in *Proc. ICMC*, Nov. 1985, pp. 215–225.

[7] J. G. Andrews, T. Bai, M. N. Kulkarni, A. Alkhateeb, A. K. Gupta, and R. W. Heath, "Modeling and analyzing millimeter wave cellular systems," *IEEE Trans. Commun.*, vol. 65, no. 1, pp. 403-430, Jan. 2017.

[8] C. Park and T. S. Rappaport, "Short-range wireless communications for next-generation networks: UWB, 60 GHz millimeter-wave WPAN, and ZigBee," *IEEE Wireless Commun.*, vol. 14, no. 4, pp. 70–78, Aug. 2007.

[9] *Local and metropolitan area networks – specific requirements – part 15.3: amendment 2: millimeter-wave-based alternative physical layer extension,* IEEE Standard 802.15.3c-2009, pp.1 —200, Oct. 2009.

[10] "SiBEAM." http://www.sibeam.com (accessed 15 Sept. 2017).

[11] W. Qi, J. Huang, J. Sun, Y. Tan, C. X. Wang, and X. Ge, "Measurements and modeling of human blockage effects for multiple millimeter wave bands," in *Proc. IWCMC'17*, pp. 1604–1609.

[12] J. Kunisch and J. Pamp, "Ultra-wideband double vertical knife-edge model for obstruction of a ray by a person," in *Proc. ICUWB*, volume 2, 2008, pp. 17–20.

[13] M. Jacob, S. Priebe, A. Maltsev, A. Lomayev, V. Erceg, and T. Kürner, "A ray tracing based stochastic human blockage model for the IEEE 802.11ad 60 GHz channel model," in *Proc. EUCAP'11*, pp. 3084–3088.

[14] X. Chen, L. Tien, P. Tang, and J. Zhang, “Modelling of human body shadowing based on 28 GHz indoor measurement results,” in *Proc. VTC-Fall’16*, pp. 1-5.

[15] N. Tran, T. Imai, and Y. Okumura, “Study on characteristics of human body shadowing in high frequency bands: Radio wave propagation technology for future radio access and mobile optical networks” in *Proc. VTC-Fall’14,* pp. 1-5.

[16] M. Ghaddar, L. Talbi, and T. A. Denidni, “Human body modelling for prediction of effect of people on indoor propagation channel,” *Electr. Lett.*, vol. 40, no. 25, pp. 1592–1594, Dec. 2004.

[17] M. Jacob et al., “Fundamental analyses of 60 GHz human blockage,” in *Proc. EuCAP’13*, pp. 117–121.

[18] M. Ghaddar, L. Talbi, T. A. Denidni, and A. Sebak, “A conducting cylinder for modeling human body presence in indoor propagation channel,” *IEEE Trans. Antennas Propag.*, vol.55, no. 11, pp. 3099– 3103, Nov 2007.

[19] M. Peter, M. Wisotzki, M. Raceala-Motoc, W. Keusgen, and R. Felbecker, “Analyzing human body shadowing at 60 GHz: Systematic wideband MIMO measurements and modeling approaches,” in *Proc. EUCAP’12*, pp. 468–472.

[20] C. Gustafson and F. Tufvesson, “Characterization of 60 GHz shadowing by human bodies and simple phantoms,” in *Proc. EUCAP’12*, pp. 473–477.

[21] G. R. MacCartney, T.S. Rappaport, and S. Rangan, “Rapid fading due to human blockage in pedestrian crowds at 5G millimeter-wave frequencies,” in *Proc. GLOBECOM*, 2017, pp. 1-7.

[22] G. R. MacCartney, S. Deng, S. Sun, and T. S. Rappaport, "Millimeter-wave human blockage at 73 GHz with a simple double knife-edge diffraction model and extension for directional antennas," in *Proc. VTC-Fall’16*, pp. 1-6.

[23] M. Jacob, C. Mbianke, and T. Kürner, “A dynamic 60 GHz radio channel model for system level simulations with MAC protocols for IEEE 802.11ad,” in *Proc. ISCE*, 2010, pp. 1-5.

[24] M. Peter et al., “Analyzing human body shadowing at 60 GHz: Systematic wideband MIMO measurements and modeling approaches,” in *Proc. EuCAP’12*, pp. 468-472.

[25] X. Zhao et al., “Attenuation by human bodies at 26- and 39.5-GHz millimeter wavebands,” *IEEE Antennas Wireless Propag. Lett.*, vol. 16, pp. 1229-1232, 2017.

[26] Q. Wang, X. Zhao, S. Li, M. Wang, S. Sun, and W. Hong, “Attenuation by a human body and trees as well as material penetration loss in 26 and 39 GHz millimeter wave bands,” *Int. J. Antennas Propag.*, vol. 2017, pp. 1-8, 2017.

[27] M. Jacob, S. Priebe, A. Maltsev, A. Lomayev, V. Erceg, and T. Kürner, “A ray tracing based stochastic human blockage model for the IEEE 802.11ad 60 GHz channel model,” in *Proc. EuCAP’11*, pp. 3084 - 3088.

[28] L. Raschkowski et al., “Deliverable D1.4: METIS channel models”, METIS, Tech. Rep. ICT-317669-METIS/D1.4, Feb. 2015.

[29] R. Sun et al., “Design and calibration of a double-directional 60 GHz channel sounder for multipath component tracking,” in *Proc. EuCAP’17*, pp. 3336-3340.

[30] D. Ferreira, I. Cuiñas, R. F. S. Caldeirinha, and T. R. Fernandes, "A review on the electromagnetic characterisation of building materials at micro- and millimetre wave frequencies," in *Proc. EuCAP’14*, pp. 145-149.

[31] C. R. Anderson and T. S. Rappaport, "In-building wideband partition loss measurements at 2.5 and 60 GHz," *IEEE Trans. Wireless Commun.*, vol. 3, no. 3, pp. 922-928, May 2004.

[32] A. V. Alejos, M. G. Sanchez, and I. Cuinas, “Measurement and analysis of propagation mechanisms at 40 GHz: viability of site shielding forced by obstacles,” *IEEE Trans. Veh. Technol*, vol. 57, pp. 3369-3380, Nov. 2008.

[33] H. Zhao et al., "28 GHz millimeter wave cellular communication measurements for reflection and penetration loss in and around buildings in New York city," in *Proc. ICC*, 2013, pp. 5163-5167.

[34] G. Vannucci and R. S. Roman, "Measurement results on indoor radio frequency re-use at 900 MHz and 18-GHz," in *Proc. PIMRC*, 1992, pp. 308-314.

[35] S. Nie, G. R. MacCartney, S. Sun and T. S. Rappaport, "72 GHz millimeter wave indoor measurements for wireless and backhaul communications," in *Proc. PIMRC,* 2013, pp. 2429-2433.

[36] A. Muqaibel, A. Safaai-Jazi, A. Bayram, A. M. Attiya, and S. M. Riad, "Ultrawideband through-the-wall propagation," *IEE Proc. Microw. Antennas Propag.*, vol. 152, no. 6, pp. 581-588, 9 Dec. 2005.

[37] G. Durgin, T. S. Rappaport, and H. Xu, "5.85-GHz radio path loss and penetration loss measurements in and around homes and trees," *IEEE Commun. Lett.*, vol. 2, no. 3, pp. 70-72, March 1998.

[38] T. S. Rappaport et al., "Millimeter wave mobile communications for 5g cellular: It will work," *IEEE Access*, vol. 1, pp. 335-349, May 2013.

[39] K. Sato et al., “Measurements of reflection and transmission characteristics of interior structures of office buildings in the 60-GHz band,” *IEEE Trans. Antennas Propag.*, vol. 45, no. 12, pp. 1783–1792, Dec. 1997.

[40] I. Cuiñas and M.G. Sánchez, “Permittivity and conductivity measurements of building materials at 5.8 GHz and 41.5 GHz” *Wireless Pers. Commun.*, vol. 20, no. 1, pp. 93-100, Jan. 2002.

[41] S. Kim, B. Bougerolles, and H. L. Bertoni, "Transmission and reflection properties of interior walls," in *Proc. ICUPC*, 1994, pp. 124-128.

[42] O. Landron, M.J. Feuerstein, T.S. Rappaport, “In situ microwave reflection coefficient measurements for smooth and rough exterior wall surfaces,” in *Proc. VTC’93,* 1993, pp. 77-80.

[43] L. Raschkowski et al., “Deliverable D1.4: METIS channel models”, METIS, Tech. Rep. ICT-317669-METIS/D1.4, Feb. 2015.

[44] William C. Stone, "Electromagnetic signal attenuation in construction materials," NIST, Gaithersburg, MD, USA, Tech. Rep. NISTIR-6055, October 1997.

[45] A.I. Sulyman, A. Alwarafy, G.R. MacCartney, T.S. Rappaport, and A. Alsanie, “Directional radio propagation path loss models for millimeter-wave wireless networks in the 28-, 60-, and 73- GHz bands,” *IEEE Trans. Wireless Commun.*, vol. 15, no. 10, pp. 6939-6947, Oct. 2016.

[46] T. Rappaport, Y. Qiao, J. Tamir, J. Murdock, and E. Ben-Dor, “Cellular broadband millimeter wave propagation and angle of arrival for adaptive beam steering systems,” in *Proc. RWS*, Santa Clara, CA, Jan. 2012, pp. 151-154.

[47] T. S. Rappaport, F. Gutierrez, E. Ben-Dor, J. N. Murdock, Y. Qiao, and J. I. Tamir, “Broadband millimeter-wave propagation measurements and models using adaptive-beam antennas for outdoor urban cellular communications,” *IEEE Trans. Antennas Propag.*, vol. 61, no. 4, pp. 1850–1859, Apr. 2013.

[48] S. Sun and T. S. Rappaport, “Wideband mmWave channels: Implications for design and implementation of adaptive beam antennas,” in *Proc. IMS 2014*, pp. 1–4. 2014.

[49] T. S. Rappaport, E. Ben-Dor, J. N. Murdock, and Y. Qiao, “38 GHz and 60 GHz angle-dependent propagation for cellular and peer-to-peer wireless communications,” in *Proc. IEEE ICC*, Jun. 2012, pp. 4568–4573.

[50] G. R. MacCartney, Jr., M. K. Samimi, and T. S. Rappaport, “Omnidirectional path loss models in New York City at 28 GHz and 73 GHz,” in *Proc. PIMRC*, Sep. 2014, pp. 227–231.

[51] E. Ben-Dor, T.S. Rappaport, Y. Qiao, and S. Lauffenburger, “Millimeter-wave 60 GHz outdoor and vehicle AoA propagation measurements using a broadband channel sounder,” in *Proc. GLOBECOM*, Dec. 2011, pp. 1-6.

[52] G. R. MacCartney, Jr., and T. S. Rappaport, “73 GHz millimeter wave propagation measurements for outdoor urban mobile and backhaul communications in New York City,” in *Proc. ICC*, Jun. 2014, pp. 4862–4867.

[53] Y. Azar et. al., “28 GHz propagation measurements for outdoor cellular communications using steerable beam antennas in New York City,” in *Proc. ICC*, 2013, pp. 5143-5147.

[54] M. Samimi et al., "28 GHz angle of arrival and angle of departure analysis for outdoor cellular communications using steerable beam antennas in New York City," in *Proc. VTC Spring-2013,* 2013, pp. 1-6.

[55] M. K. Samimi and T. S. Rappaport, "Ultra-wideband statistical channel model for non line of sight millimeter-wave urban channels," in *Proc. GLOBECOM*, Dec. 2014, pp. 3483–3489.

[56] S. Sun, G. R. MacCartney, Jr., M. K. Samimi, S. Nie, and T. S. Rappaport, ''Millimeter wave multi-beam antenna combining for 5G cellular link improvement in New York City,'' in *Proc. ICC*, Jun. 2014, pp. 5468–5473.

[57] S. Nie, G. R. MacCartney, S. Sun, and T. S. Rappaport, "28 GHz and 73 GHz signal outage study for millimeter wave cellular and backhaul communications," in *Proc. ICC*, Jun. 2014, pp. 4856–4861.

[58] L. J. Greenstein, D. G. Michelson, and V. Erceg, "Moment-method estimation of the Ricean K-factor," *IEEE Commun. Lett.*, vol. 3, no. 6, pp. 175–176, June 1999.

[59] S. Sun and T. S. Rappaport, ''Multi-beam antenna combining for 28 GHz cellular link improvement in urban environments,'' in *Proc. GLOBECOM*, Dec. 2013, pp. 3754-3759.

[60] G. R. MacCartney, Jr., H. Yan, S. Sun, and T. S. Rappaport, "A flexible wideband millimeter-wave channel sounder with local area and NLOS to LOS transition measurements," in *Proc. ICC*, May 2017, pp. 1-7.

[61] *Approved IEEE Draft Revision for IEEE Standard for Information Technology-Telecommunications and Information Exchange Between Systems-Local and Metropolitan Area Networks-Specific Requirements—Part 15.4B: Wireless Medium Access Control (MAC) and Physical Layer (PHY) Specifications for Low Rate Wireless Personal Area Networks (WPANs)*, IEEE Standard P802.15.4/D6, 2009. [Online]. Available: http://www.ieee802.org/15/pub/TG3c.html

[62] *IEEE Standard for Information Technology—Telecommunications and Information Exchange Between Systems—Local and Metropolitan Area Networks—Specific Requirements—Part 11: Wireless LAN Medium Access Control (MAC) and Physical Layer (PHY) Specifications Amendment 3: Enhancements for Very High Throughput in the 60 GHz Band*, IEEE Standard 802.11ad-2012, Dec. 2012. [Online]. Available: http://standards.ieee.org/findstds/standard/802.11ad-2012.html

[63] "Wireless HD Consortium Home Page." http://www.wirelesshd.org (accessed Jul. 11, 2018).

[64] Z. Yang, P. H. Pathak, Y. Zeng, and P. Mohapatra, "Sensor-assisted codebook-based beamforming for mobility management in 60 GHz WLANs," in *Proc. MASS*, 2015, pp. 333 – 341.

[65] D.S. Shim, C.K. Yang, J. H. Kim, J. P. Han, and Y. S. Cho, "Application of motion sensors for beam-tracking of mobile stations in mmWave communication systems," *Sensors*, vol. 14, no. 10, pp. 19622-19638, Oct. 2014.

[66] C. Zhang, D. Guo, and P. Fan, "Tracking angles of departure and arrival in a mobile millimeter wave channel," in *Proc. ICC*, May 2016, pp. 1– 6.

[67] V. Va, H. Vikalo, and R. W. Heath, "Beam tracking for mobile millimeter wave communication systems," in *Proc. GlobalSIP*, 2016, pp. 743–747.

[68] N. Czink, C. Mecklenbrauker, and G. Del Galdo, "A novel automatic cluster tracking algorithm," in *Proc. PIMRC*, Sep. 2006, pp. 1– 5.

[69] J. Wang, Z Lan et. al, "Beam codebook-based beamforming protocol for multi-Gbps millimeter-wave WPAN systems," *IEEE J. Sel. Areas Commun.*, vol. 27, no. 8, pp. 1390 – 1399, Oct. 2009.

[70] M. Jasim and N. Ghani, "Fast beam discovery for mmWave cellular networks," in *Proc. WAMICON*, 2017, pp. 1–6.

[71] A. Alkhateeb, Y. H. Nam, M. S. Rahman, J. Zhang, and R.W. Heath, "Initial beam association in millimeter wave cellular systems: Analysis and design insights," *IEEE Trans. Wireless Commun.*, vol. 16, no. 5, pp. 2807–2821, May 2017.

[72] J. Kim and S.-N. Hong, "Dynamic two-stage beam training for energy efficient millimeter wave 5G cellular systems," *Telecommun. Syst.*, vol. 59, no. 1, pp. 111–122, 2014.

[73] M. E. Eltayeb, A. Alkhateeb, R. W. Heath, and T. Y. Al-Naffouri, "Opportunistic beam training with hybrid analog/digital codebooks for mmWave systems," in *Proc. GlobalSIP*, Dec. 2015, pp. 315-319.

[74] A. Alkhateeb, O. El Ayach, G. Leus, and R. W. Heath, "Hybrid precoding for millimeter wave cellular systems with partial channel knowledge," in *Proc. ITA*, Feb. 2013, pp. 1-5.

[75] M. Giordani, M. Mezzavilla, C. N. Barati, S. Rangan, and M. Zorzi, "Comparative analysis of initial access techniques in 5G mmWave cellular networks," in *Proc. CISS*, 2016, pp. 268–273.

[76] M. Giordani, M. Mezzavilla, and M. Zorzi, "Initial access in 5G mmWave cellular networks," *IEEE Commun. Mag.*, vol. 54, no. 11, pp. 40 – 47, Nov. 2016.

[77] C. N. Barati et al., "Initial access in millimeter wave cellular systems," *IEEE Trans. Wireless Commun.*, vol. 15, no. 12, pp. 7926 – 7940, Dec. 2016.

[78] A. Capone, I. Filippini, and V. Sciancalepore, "Context information for fast cell discovery in mm-Wave 5G networks," in *Proc. Eur. Wireless Conf.*, May 2015, pp. 1 – 6.

[79] W. B. Abbas and M. Zorzi, "Context information based initial cell search for millimeter wave 5G cellular networks," in *Proc. EuCNC*, 2016, pp. 1 – 7.

[80] Z. Yang, P. H. Pathak, Y. Zeng, and P. Mohapatra, “Sensor-assisted codebook-based beamforming for mobility management in 60 GHz WLANs,” in *Proc. MASS*, 2015, pp. 333 – 341.

[81] D.S. Shim, C.K. Yang, J. H. Kim, J. P. Han, and Y. S. Cho, “Application of motion sensors for beam-tracking of mobile stations in mmWave communication systems,” *Sensors*, vol. 14, no. 10, pp. 19622-19638, Oct. 2014.

[82] C. Zhang, D. Guo, and P. Fan, “Tracking angles of departure and arrival in a mobile millimeter wave channel,” in *Proc. ICC*, May 2016, pp. 1– 6.

[83] V. Va, H. Vikalo, and R. W. Heath, “Beam tracking for mobile millimeter wave communication systems,” in *Proc. GlobalSIP*, 2016, pp. 743 – 747.

[84] T. S. Rappaport, J. N. Murdock, and F. Gutierrez, "State of the art in 60-GHz integrated circuits and systems for wireless communications," *Proc. IEEE*, vol. 99, no. 8, pp. 1390-1436, Aug. 2011.

[85] S. Salous, *Radio Propagation Measurement and Channel Modelling*. West Sussex, U.K.: Wiley, 2013.

Appendices

Appendix A: NIST 60 GHz Channel Sounder

A block diagram of the NIST 60 GHz channel sounder used to collect the channel measurement data used in the human presence studies is shown in Figure 58.

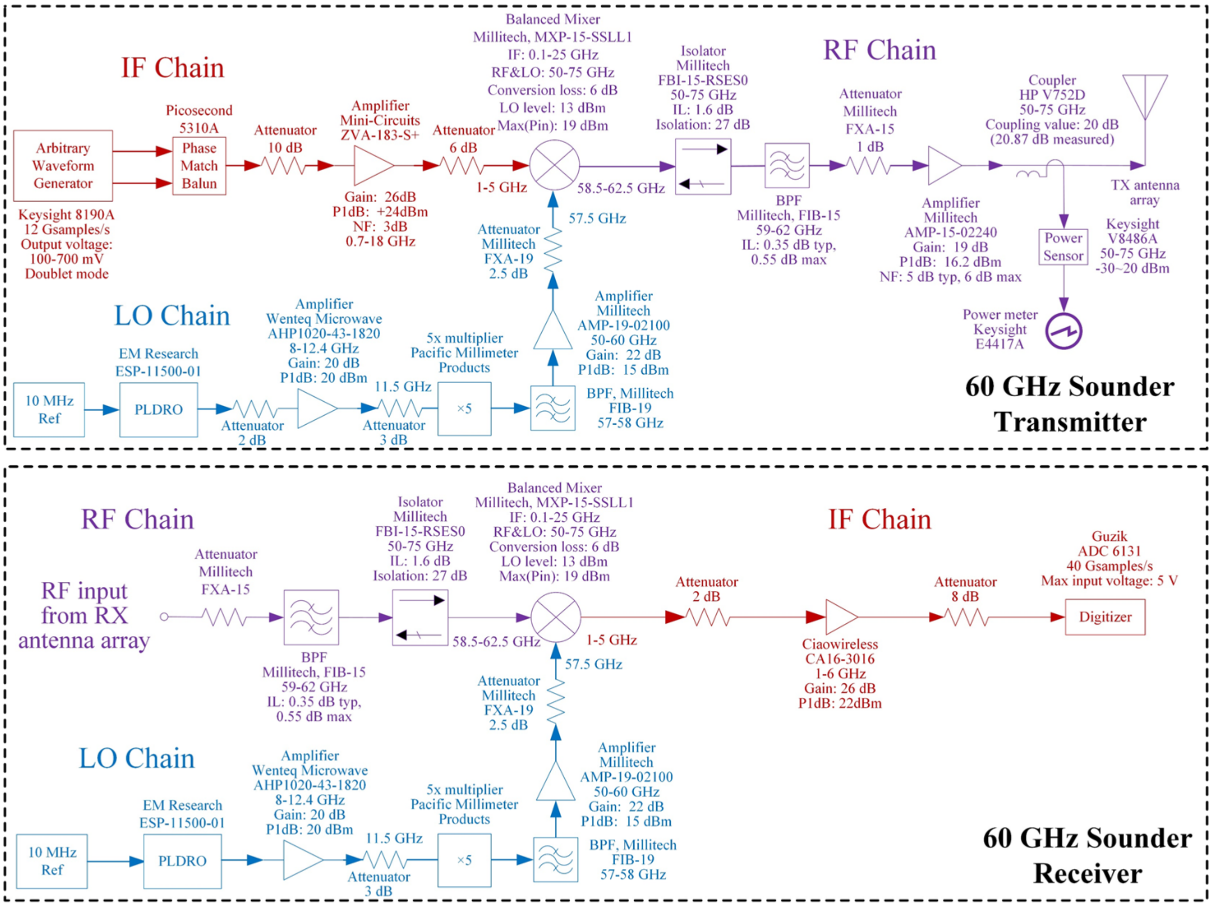

Figure 58 - Channel Sounder Configuration for Human Presence Measurements

Appendix B: Through Wall Attenuation Measurement Locations

B.1 Wood Measurement Locations

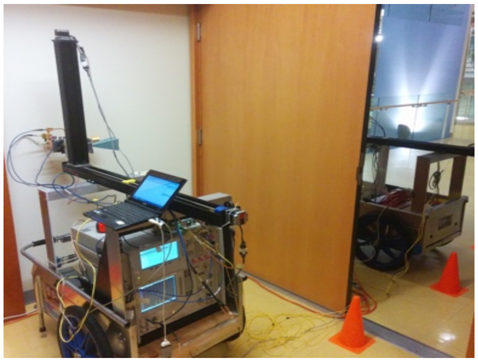

(a)

(b)

(c)

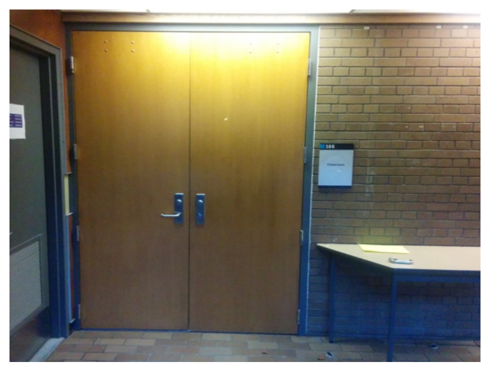

(d)

Figure 59 - Wood Measurement Locations: (a) Wood 1; (b) Wood 2; (c) Wood 3; (d) Wood 4

B.2 Metal Clad Measurement Locations

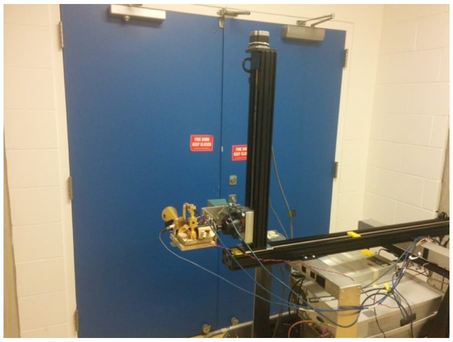

(a)

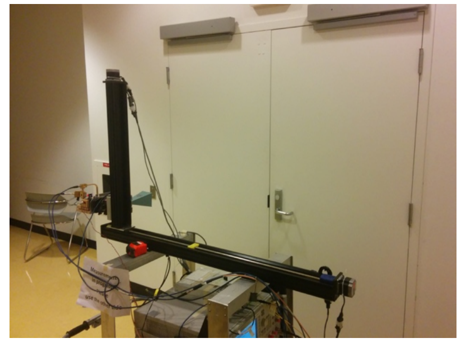

(b)

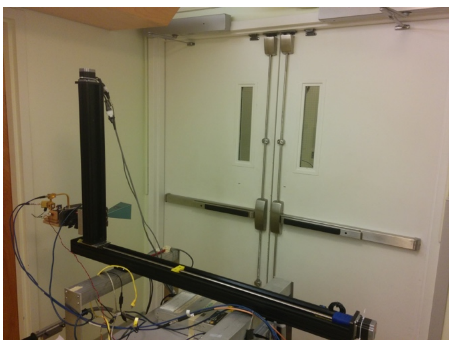

(c)

(d)

(e)

Figure 60 - Metal Measurement Locations: (a) Metal 1; (b) Metal 2; (c) Metal 3; (d) Metal 4; (e) Metal 5

B.3 Glass Measurement Locations

(a)

(b)

(c)

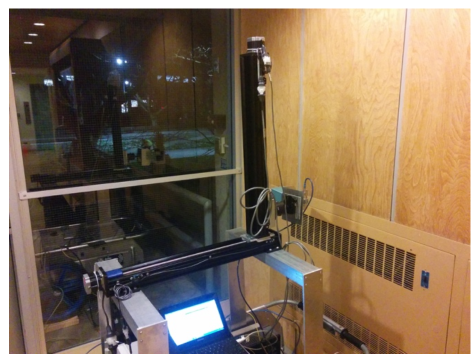

(d)

Figure 61 - Glass Measurement Locations: (a) Glass 1; (b) Glass 2; (c) Glass 3; (d) Glass 4

B.4 Drywall Measurement Locations

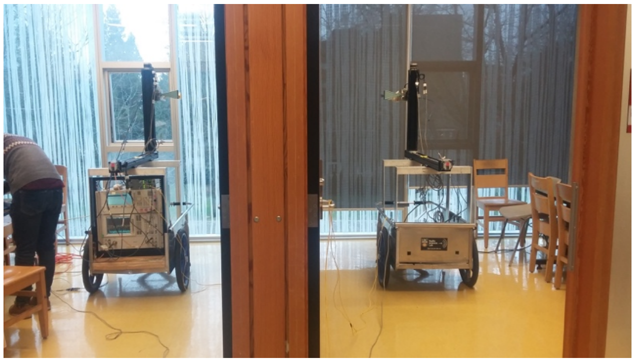

(a)

(b)

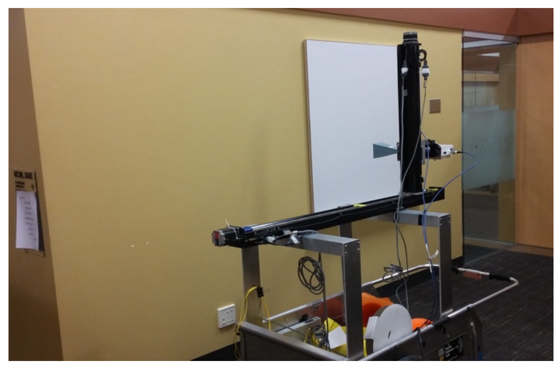

(c)

Figure 62 - Drywall Measurement Locations: (a) Drywall 1; (b) Drywalls 3 and 4; (c) Drywall 5

B.5 Masonry Measurement Locations

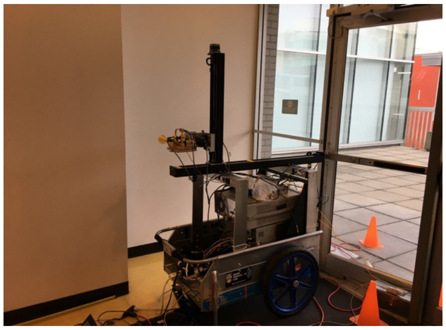

(a)

(b)

(c)

(d)

Figure 63 - Masonry Measurement Locations - (a) Masonry 1; (b) Masonry 2; (c) Masonry 3; (d) Masonry 4